

---

Modelling and Investigation of  
Airborne Electromagnetic Data, and  
Reprocessing of Vibroseis Data,  
from Nechako Basin, B.C.,  
Guided by Magnetotelluric Results

Final report prepared for Geoscience BC

by

Jessica Spratt, J. Kim Welford, Colin Farquharson and Jim Craven

Geoscience BC Report 2012-14

---

July 27th, 2012

## Summary

Magnetotelluric (MT) data collected in the Nechako Basin during 2007 have previously been inverted to produce 2D conductivity sections along seven profiles through the region. In the work reported here, these conductivity sections were used to assess the ability of z-axis tipper electromagnetic (ZTEM) data to determine and resolve the conductivity structure of the Nechako Basin, and to investigate the possibility of using the MT-derived conductivity sections to assist in processing the multichannel seismic reflection data collected across the basin in 2008. ZTEM is a natural-source, airborne electromagnetic (EM) technique. As such it has the potential to sense conductive features deeper in the subsurface than controlled-source airborne methods. Also, it can efficiently cover much larger areas than any ground-based EM method. Synthetic ZTEM data were generated from the conductivity sections produced by the inversion of the full 2007 MT data-set. The ZTEM data-sets were generated for different frequency ranges, different numbers of measurement frequencies, and for different densities of measurement locations. The results indicated that, although highly dependent on the actual conductivity structure in different parts of the basin, ZTEM data may be capable of identifying the conductive Eocene volcanoclastic rocks to shallow depths but may struggle to differentiate between the Eocene groups and the Cretaceous sedimentary rocks. Multichannel seismic reflection data were acquired along a number of profiles through the Nechako Basin in 2008. To date, processing of this data-set has proved challenging because of the complex structure of the region, with results not giving as much information about the subsurface as hoped. Here, an attempt was made to use the MT-derived 2D conductivity sections in the processing of the seismic data. In particular, conductivities were converted to seismic velocities using a selection of rock property-derived relationships, and these velocities then used to stack the data. In addition, reprocessing of the seismic data without the use of MT-derived information was performed for comparison with results from previous processing attempts. The reprocessing of the seismic data resulted in sections with moderately improved reflectivity, although no new structures were revealed that had not been discernible previously. The MT-derived velocity models provided surprisingly decent starting models for the velocity analysis required for stacking the seismic data, but nothing that could not be obtained by conventional velocity analysis of the seismic data alone. Finally, work was performed to integrate the interpretations derived from the MT data with those from other existing geophysical and geological data in order to improve our understanding of the structure and formation of the Nechako Basin. The results of this integration work appear in the special section "New insights in Cordilleran Intermontane geoscience: reducing exploration risk in the mountain pine beetle-affected area, British Columbia" of the Canadian Journal of Earth Sciences (v. 48, n. 6).

## Table of Contents

<b>Introduction</b>	<b>11</b>
<b>Modelling and Assessment of ZTEM Data</b>	<b>11</b>
<b>Background Information</b>	<b>11</b>
<b>Analysis of ZTEM data derived from measured MT responses</b>	<b>16</b>
<b>Conclusions from 2-D modelling</b>	<b>41</b>
<b>Integration of MT Derived Models in a Tectonic History of the Nechako Basin</b>	<b>42</b>
<b>Seismic Reprocessing</b>	<b>42</b>
<b>Goals</b>	<b>42</b>
<b>Regional Setting</b>	<b>43</b>
<b>Standard Reprocessing of Vibroseis Data</b>	<b>46</b>
<b>Overview</b>	<b>46</b>
<b>Data</b>	<b>46</b>
<b>Processing Summary</b>	<b>46</b>
<b>Description of Key Processors</b>	<b>47</b>
<i>Gain Recovery</i>	<i>47</i>

<i>Crooked Line 2D Geometry</i>	47
<i>Frequency Filtering</i>	53
<i>Surface Consistent Deconvolution</i>	53
<i>Near Surface Statics</i>	53
<i>Velocity Analysis and Normal Moveout (NMO)</i>	54
<i>Residual Statics</i>	55
<i>Stack</i>	56
<i>Migration</i>	56
<i>Coherency Filtering</i>	57
<b>Interpretation of the Reprocessed Sections</b>	<b>58</b>
<b>Assessing Contribution of MT Results to Reprocessing of Vibroseis Data</b>	<b>60</b>
<b>Physical Property Measurements and Well Logs</b>	<b>60</b>
<b>Resistivity to Velocity Conversion</b>	<b>62</b>
<b>Building the Optimal Velocity Model</b>	<b>67</b>
<b>Stack Comparison</b>	<b>68</b>
<b>Joint Interpretation</b>	<b>69</b>
<b>Key Findings from the Seismic Reprocessing</b>	<b>72</b>
<b>Future Work</b>	<b>73</b>

<b>References</b>	<b>74</b>
<b>Appendix: Fold-out sections</b>	<b>76</b>

## Table of Figures

<b>Figure 1:</b> Geological map of the southern Nechako basin showing the measured 2007 MT site and profile locations.	12
<b>Figure 2:</b> Two-dimensional conductivity models and interpretations for profiles A, B, C, and D.	13
<b>Figure 3:</b> Two-dimensional conductivity models and interpretations for profiles F, G, and H.	14
<b>Figure 4:</b> Plots of the tipper magnitude for two sites at the various frequency distributions included in inversions	17
<b>Figure 5:</b> Pseudo-sections of the tipper data as function of frequency for profile A.	19
<b>Figure 6:</b> Pseudo-sections of the tipper data as function of frequency for profile B.	20
<b>Figure 7:</b> Pseudo-sections of the tipper data as function of frequency for profile C.	21
<b>Figure 8:</b> Pseudo-sections of the tipper data as function of frequency for profile D.	22
<b>Figure 9:</b> Pseudo-sections of the tipper data as function of frequency for profile F.	23
<b>Figure 10:</b> Pseudo-sections of the tipper data as function of frequency for profile G.	24
<b>Figure 11:</b> Pseudo-sections of the tipper data as function of frequency for profile H.	25
<b>Figure 12:</b> Plots of induction vectors of the 2007 measured MT data at the northern part of the MT survey area (includes profiles A, B, C, and D) at various frequencies.	26
<b>Figure 13:</b> Plots of induction vectors of the 2007 measured MT data at the southern part of the MT survey area (includes profiles F, G, and H) at various frequencies.	27
<b>Figure 14:</b> Plots of induction vectors of the 2007 measured MT data at the northern part of the MT survey area (includes profiles A, B, C, and D) at the frequencies specific to ZTEM surveys.	28
<b>Figure 15:</b> Plots of induction vectors of the 2007 measured MT data at the southern part of the MT survey area (includes profiles F, G, and H) at the frequencies specific to ZTEM surveys.	29
<b>Figure 16:</b> Results of two-dimensional modelling of measured and synthetic MT data along profile A.	32
<b>Figure 17:</b> Results of two-dimensional modelling of measured and synthetic MT data along profile B.	34

## Table of Figures

<b>Figure 18:</b> Results of two-dimensional modelling of measured and synthetic MT data at a site spacing of 100 m along profile C.	<b>36</b>
<b>Figure 19:</b> Results of two-dimensional modelling of measured and synthetic MT data at a site spacing of 100 m along profile D.	<b>37</b>
<b>Figure 20:</b> Results of two-dimensional modelling of measured and synthetic MT data at a site spacing of 100 m along profile F.	<b>39</b>
<b>Figure 21:</b> Results of two-dimensional modelling of measured and synthetic MT data at a site spacing of 100 m along profile G.	<b>40</b>
<b>Figure 22:</b> Results of two-dimensional modelling of measured and synthetic MT data at a site spacing of 100 m along profile H.	<b>41</b>
<b>Figure 23:</b> Regional geological map of southern British Columbia	<b>44</b>
<b>Figure 24:</b> Detailed geological map of study area	<b>45</b>
<b>Figure 25:</b> Map of Line 2008-05 geometry	<b>49</b>
<b>Figure 26:</b> Map of Line 2008-10 geometry	<b>50</b>
<b>Figure 27:</b> Map of Line 2008-12 geometry	<b>51</b>
<b>Figure 28:</b> Map of Line 2008-13 geometry	<b>52</b>
<b>Figure 29:</b> Plot of dry P-wave velocity (km/s) versus resistivity (Ohm*m)	<b>61</b>
<b>Figure 30:</b> Resistivity model and empirically-derived velocity models for Line 2008-5	<b>63</b>
<b>Figure 31:</b> Resistivity model and empirically-derived velocity models for Line 2008-10	<b>64</b>
<b>Figure 32:</b> Histograms of the occurrence of resistivity values in the 2-D model along profile B.	<b>65</b>
<b>Figure 33:</b> Comparison of the results of 1-D models calculated from MT site locations and those generated from synthetic response curves derived from the resistivity borehole logs.	<b>66</b>
<b>Figure 34:</b> Comparison between the stacking velocities and the empirically-derived velocities.	<b>67</b>
<b>Figure 35:</b> Optimal velocity model for Line 2008-5 based on lithology-specific application of velocities empirically-derived from the resistivity model.	<b>68</b>
<b>Figure 36:</b> Optimal velocity model for Line 2008-10 based on lithology-specific application of velocities empirically-derived from the resistivity model.	<b>68</b>

## Table of Figures

<b>Figure 37:</b> <i>Depth-converted final stack for Line 2008-5 overlain on the MT-derived resistivity model.</i>	<b>69</b>
<b>Figure 38:</b> <i>Depth-converted final stack for Line 2008-10 overlain on the MT-derived resistivity model.</i>	<b>71</b>
<hr/>	
<b>Figure A-1:</b> <i>Comparison of final stacks from this study (A) and from original CGG Veritas processing (B) for Line 2008-5.</i>	<b>77</b>
<b>Figure A-2:</b> <i>Comparison of final stacks from this study (A) and from original CGG Veritas processing (B) for Line 2008-12.</i>	<b>77</b>
<b>Figure A-3:</b> <i>Comparison of final stacks from this study (A) and from original CGG Veritas processing (B) for Line 2008-10.</i>	<b>78</b>
<b>Figure A-4:</b> <i>Comparison of final stacks from this study (A) and from original CGG Veritas processing (B) for Line 2008-13.</i>	<b>79</b>
<b>Figure A-5:</b> <i>Comparison of interpreted final stacks from this study (A) and from original CGG Veritas processing (B) for Line 2008-5.</i>	<b>80</b>
<b>Figure A-6:</b> <i>Comparison of interpreted final stacks from this study (A) and from original CGG Veritas processing (B) for Line 2008-12.</i>	<b>80</b>
<b>Figure A-7:</b> <i>Comparison of interpreted final stacks from this study (A) and from original CGG Veritas processing (B) for Line 2008-10.</i>	<b>81</b>
<b>Figure A-8:</b> <i>Comparison of interpreted final stacks from this study (A) and from original CGG Veritas processing (B) for Line 2008-13.</i>	<b>82</b>
<b>Figure A-9:</b> <i>Post-stack migrated sections for Line 2008-5; (A) finite-difference, this study; (B) Kirchhoff, this study; (C) F-K phase-shift, CGG Veritas processing.</i>	<b>83</b>
<b>Figure A-10:</b> <i>Post-stack migrated sections for Line 2008-12; (A) finite-difference, this study; (B) Kirchhoff, this study; (C) F-K phase-shift, CGG Veritas processing.</i>	<b>83</b>
<b>Figure A-11:</b> <i>Post-stack migrated sections for Line 2008-10; (A) finite-difference, this study; (B) Kirchhoff, this study; (C) F-K phase-shift, CGG Veritas processing.</i>	<b>84</b>
<b>Figure A-12:</b> <i>Post-stack migrated sections for Line 2008-13; (A) finite-difference, this study; (B) Kirchhoff, this study; (C) F-K phase-shift, CGG Veritas processing.</i>	<b>85</b>
<b>Figure A-13:</b> <i>Migrated sections with interpretation for Line 2008-5.</i>	<b>86</b>
<b>Figure A-14:</b> <i>Migrated sections with interpretation for Line 2008-12.</i>	<b>86</b>
<b>Figure A-15:</b> <i>Migrated sections with interpretation for Line 2008-10.</i>	<b>87</b>
<b>Figure A-16:</b> <i>Migrated sections with interpretation for Line 2008-13.</i>	<b>88</b>

## Table of Figures

<b>Figure A-17:</b> <i>Coherency filtered complete stack (to 18 s TWT) for Line 2008-5.</i>	<b>89</b>
<b>Figure A-18:</b> <i>Coherency filtered complete stack (to 18 s TWT) for Line 2008-12.</i>	<b>89</b>
<b>Figure A-19:</b> <i>Coherency filtered complete stack (to 18 s TWT) for Line 2008-10.</i>	<b>90</b>
<b>Figure A-20:</b> <i>Coherency filtered complete stack (to 18 s TWT) for Line 2008-13.</i>	<b>91</b>
<b>Figure A-21:</b> <i>Comparison between brute stack obtained using MT-derived velocities (A) and final stack (B) for Line 2008-5</i>	<b>92</b>
<b>Figure A-22:</b> <i>Comparison between brute stack obtained using MT-derived velocities (A) and final stack (B) for Line 2008-10</i>	<b>93</b>

## Table of Tables

**Table 1:** *Geometry parameters*

**48**

## Introduction

This report describes, in detail, the final results from the project: “Modelling and Investigations of Airborne Electromagnetic Data, and Reprocessing of Vibroseis Data, From Nechako Basin, B.C., Guided by Magnetotelluric Results”. This work was proposed to aid in the objectives of Geoscience BC's project “Geoscience to Stimulate Exploration Activity in the Nechako Basin, British Columbia”. The services provided under this contract fall under three main categories: 1) modelling and assessment of ZTEM data, 2) MT guided reprocessing of vibroseis data, and 3) integration of MT-derived models in a tectonic history of the Nechako basin. The ZTEM data were analyzed by Ms. Jessica Spratt and the seismic reprocessing was undertaken by Dr. J. Kim Welford at Memorial University in St. John's, Newfoundland, on a part-time basis from April 2011 to February 2012.

## Modelling and Assessment of ZTEM Data

### Background Information

The Nechako Basin, located within the Intermontane belt of the Canadian Cordillera, is an Upper Cretaceous to Oligocene sedimentary basin that formed in response to terrane amalgamation along the western edge of ancestral North America. It extends up to 5 km in thickness and consists of three primary geological elements: Early Cretaceous sedimentary rocks of the Taylor Creek and Skeena groups, Eocene volcanoclastic rocks that include the Endako and Ootsa Lake groups, and Neogene Chilcotin Group basalts (Figure 1). The potential for hydrocarbon reservoirs has been noted within the Cretaceous sedimentary packages and several studies, including MT, have been carried out to determine the thickness, internal structure, and distribution of these units with the goal of resolving the structure of the Nechako basin and evaluating this potential.

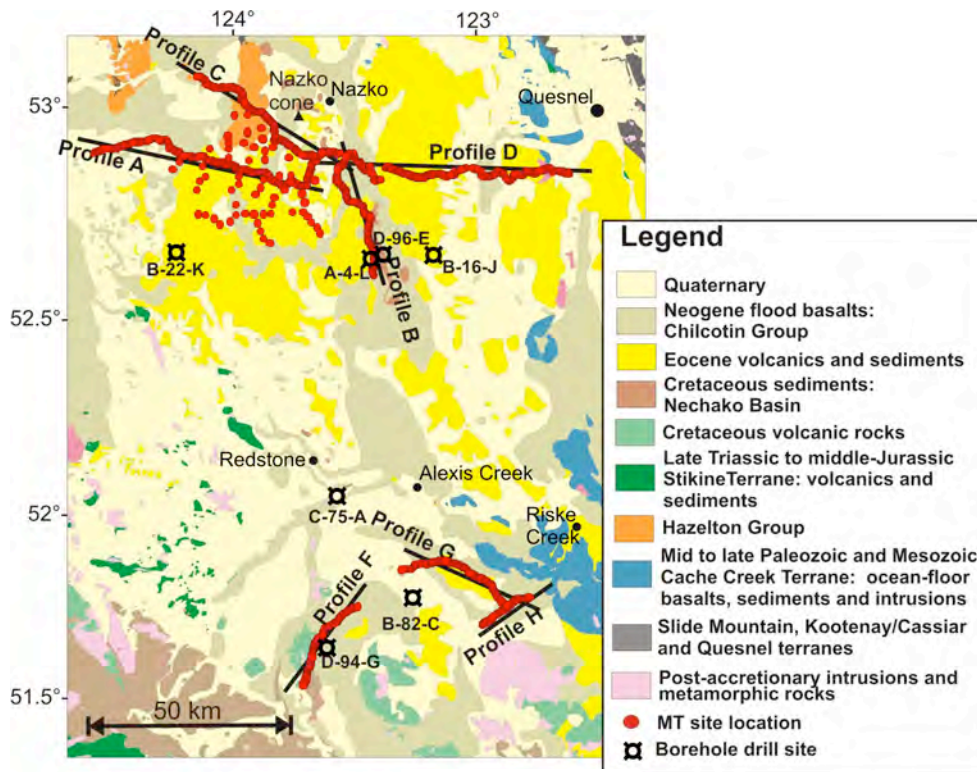


**Figure 1:** Geological map of the southern Nechako basin showing the measured 2007 MT site and profile locations.

Magnetotelluric (MT) data were collected within the Nechako Basin in 2007 and were successful in imaging the conductivity structure beneath two-dimensional (2-D) profiles (Figures 2 and 3). They demonstrated that the method is capable of differentiating the various rock types and identifying structural features in the subsurface (Spratt and Craven, 2011). It has been suggested that acquiring airborne z-axis tipper electromagnetic (ZTEM) data over the Nechako Basin could be useful for mapping the thickness of overlying volcanic layers and identifying areas of reservoir potential, particularly in the regions between the MT profiles where the conductivity structure is unknown. The ZTEM method measures airborne electromagnetic data that provide information on the 3-D conductivity structure to depths up to 2 km, deeper than other airborne methods, and is a cost-effective way to record high density transfer function data over a broad region. The data, however, are not sensitive to 1-D layers (Holtham and Oldenburg, 2010) and, depending on the conductivity of the subsurface, the

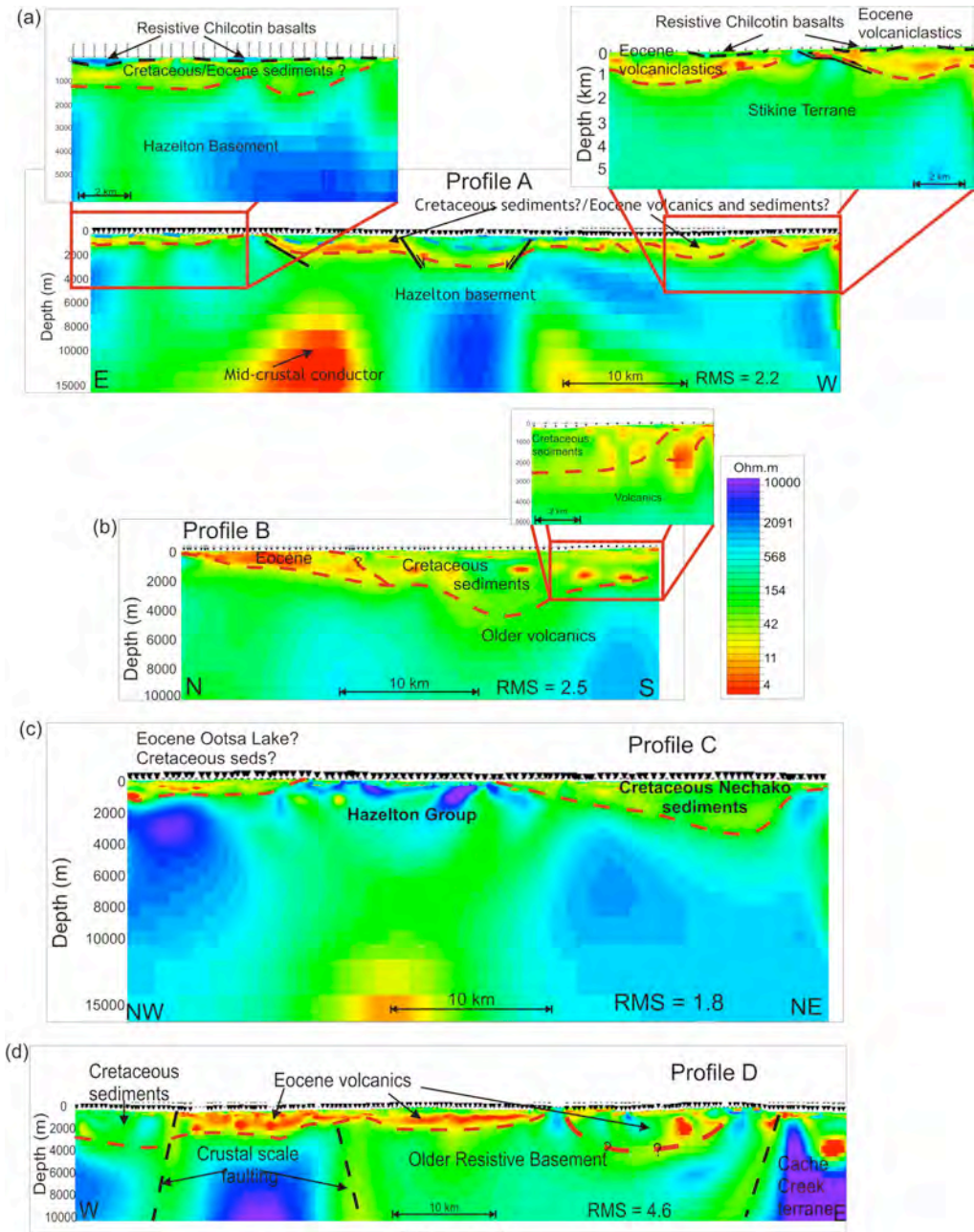


**Figure 2:** Two-dimensional conductivity models and interpretations for (a) profile A, (b) profile B, (c) profile C, and (d) profile D. The red dashed line illustrates the interpreted base of the Nechako basin and the black lines represent fault lines.

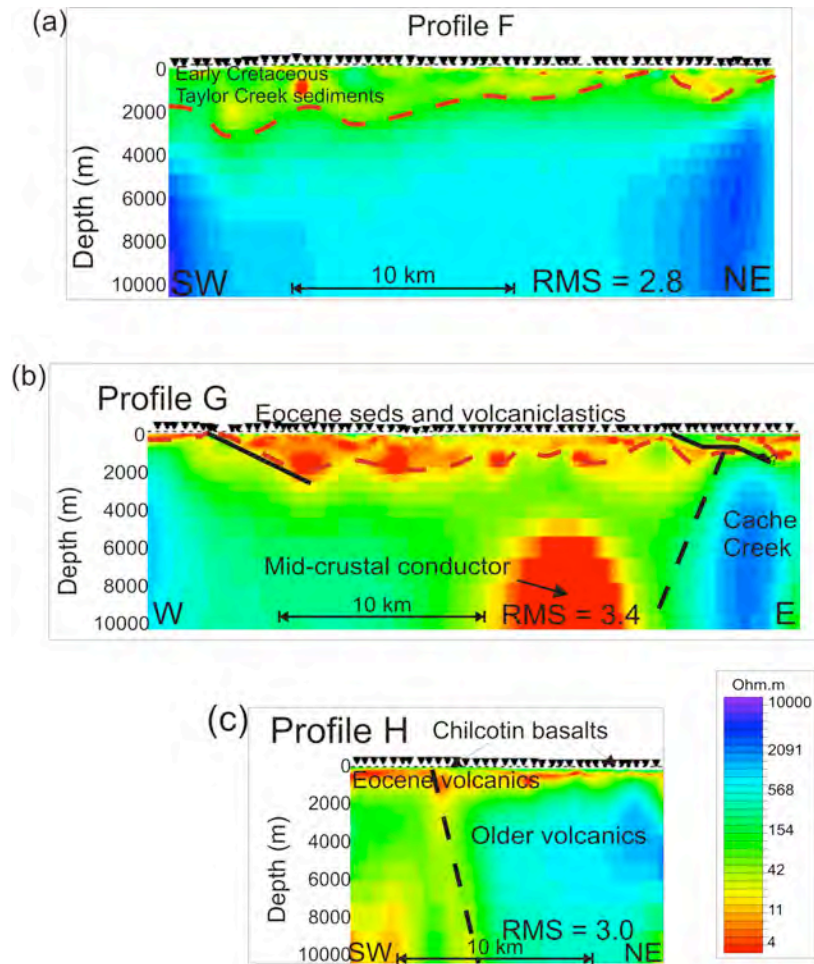


**Figure 3:** Two-dimensional conductivity models and interpretations for (a) profile F, (b) profile G, and (c) profile H. The red dashed line illustrates the interpreted base of the Nechako basin and the black lines represent fault lines.

frequencies measured may yield low resolution of the models and limited penetration depths. As MT data record the horizontal and vertical components of magnetic field on the ground, along with the electric fields, the transfer functions are available at each recorded site. Results from the 2007 MT survey have been analyzed to determine the benefits of a ZTEM survey over the Nechako basin.

In the fall of 2007, combined high-frequency audio-magnetotelluric (AMT) and broadband magnetotelluric (BBMT) data were collected at a total of 734 sites through the southern part of the Nechako Basin at a site spacing of 200 - 500 m (Spratt and

Craven, 2009; Figure 1). The data were processed by Geosystem Canada using robust remote-reference techniques that generally resulted in excellent data quality covering a range of nearly seven orders of magnitude from 10000 to 0.001 Hz (Spratt and Craven, 2009). For every three successive sites the vertical-field data were recorded in the BBMT range (200–0.0001 Hz) at the first site, the AMT range (10 000–1 Hz) at the second site, and no vertical-field data were recorded at the third site. In general, the data quality is excellent to frequencies up to 1 Hz. Each site was analyzed for distortion, dimensionality and directionality, and a 2-D model was generated along seven separate profiles (A,B,C,D, F,G, and H) by inverting data from the 3 main MT components: the transverse magnetic (TM) mode, transverse electric (TE) mode and the transfer functions (TF) data (Spratt and Craven, 2010, 2011). Details on the MT method, data analysis, and modelling techniques are described in Spratt and Craven, 2009.

The models of the measured 2007 MT data, in general, reveal three distinct horizontal units that characterize the conductivity structure of the Nechako Basin; these units are best resolved in the models along profiles A, B, C and F. A near-surface resistive layer (>500 Ohm•m) is interpreted as the Chilcotin basalts, which blanket portions of the region to depths of <50 m but can locally thicken up to 200 m in paleochannels. A low-resistivity unit underlies the near-surface resistor with a variable thickness between 0 and 4000 m. This unit appears to have two end members with varying resistivity signatures: the Cretaceous sedimentary units are characterized by moderate resistivities (10–100 Ohm•m) that are laterally highly variable, whereas lower, more uniform conductivity values (<4 Ohm•m) appear to be associated with the Eocene volcanoclastic groups. The base of the Nechako Basin is marked by an increase in resistivity (>200 Ohm•m) associated with the deeper underlying Cretaceous volcanic units or island-arc terranes. In addition to the layered resistivity structure, the data also image folding and faulting of the Nechako sediments, structural features that may provide an environment for trapping hydrocarbons.

## **Analysis of ZTEM data derived from measured MT responses**

Similar to the MT method, ZTEM uses natural fields as the source of transmitted energy to resolve a conductivity-depth profile of the Earth. The method involves interpretation of transfer functions that relate the local airborne vertical field to mutually perpendicular horizontal magnetic fields recorded at a reference station on the ground. Common line spacings used in airborne ZTEM surveys are 100–400 m (Geotech Limited 2009a, Sattell, 2010). Data are recorded at an output sampling rate of 2.5 samples/second and the recording equipment is typically flown at a speed of 80 km/h for a nominal sample spacing of 8 m along each line flown. In theory, current ZTEM instrumentation can measure data in the frequency range 22–2800 Hz; however, typical surveys process data at 30, 45, 90, 180, 360 and occasionally 720 Hz (e.g., Geotech Limited, 2009a; Geotech Limited, 2009b; Lo et al. 2009).

Synthetic transfer-function data have been computed from the 2-D conductivity models produced by the inversion of all components of the MT data using the WinGlink® MT interpretation software package. The data have been computed at a site spacing of 100 m along each of the MT profiles, a site spacing that reaches the limit of the modelling program. These synthetic data have been generated by creating additional sites along the profiles, importing the final 2-D models, running a forward inversion and then saving the calculated responses as station data. Note that no noise was added to the synthetic data, as it appears that the WinGlink program only adds random gaussian noise to the TE and TM modes. The different data sets used in the assessment of the transfer functions and in the subsequent 2-D modelling along each of the MT profiles include: (a) the 2007 Nechako Basin MT survey at all measured frequencies, (b) the 2007 Nechako Basin MT survey at the ZTEM frequency range, (c) synthetic ZTEM data (computed from the 2-D models that have been produced from the original data) at the frequency range of the collected MT data, (d) synthetic ZTEM data at the ZTEM frequency ranges, and (e) synthetic ZTEM data at the frequencies specific to typical ZTEM surveys. Figure 4 shows examples of different frequency ranges used in various 2-D model inversions for two sites: one located above conductive Eocene volcanoclastic

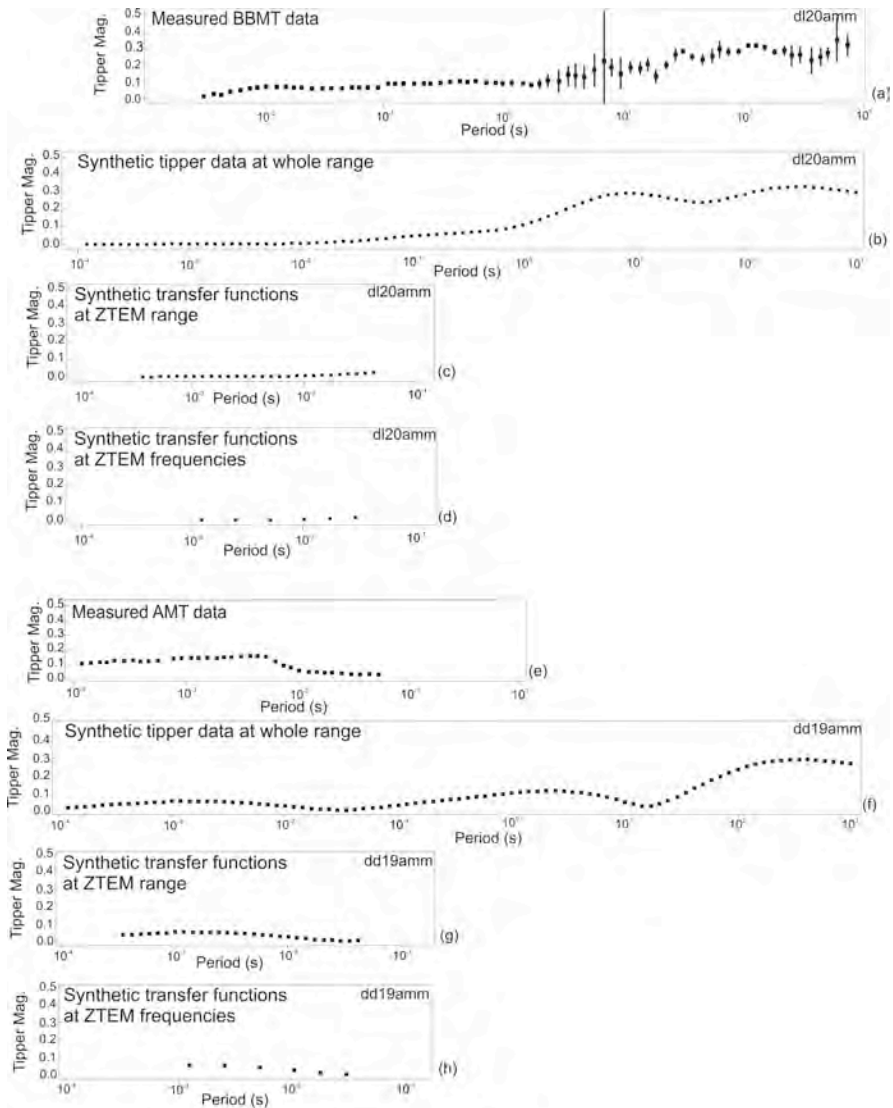


**Figure 4:** Plots of the tipper magnitude for two sites at the various frequency distributions included in inversions: (a) shows the measured data from BBMT site dd22amm, located above the conductive Eocene volcanoclastics, (b) shows the synthetic data derived from the 2-D MT model at site dd22amm, (c) shows the synthetic data at site dd22amm, over the ZTEM period range, and (d) shows the synthetic data at site dd22amm, at the periods typically analyzed using the ZTEM method. (e) shows the measured data from AMT site dd19aam, located above exposed Cretaceous sedimentary rocks, (f) shows the synthetic data derived from the 2-D MT model at site dd19aam, (g) shows the synthetic data at site dd19aam, over the ZTEM period range, and (h) shows the synthetic data at site dd19aam, at the periods typically analyzed using the ZTEM method.

rocks and the other located above exposed Cretaceous sedimentary units.

In order to assess the quality of the data, the magnetic transfer functions have been plotted as pseudo-sections of relative apparent resistivity using frequency as a proxy for depth, and induction vectors have been plotted at a variety of frequencies. Figures 5 to 11 show the plotted transfer function pseudo-sections along each of the MT profiles for the measured and synthetic data for the various data sets (frequency ranges) described above. Induction vectors are shown at a variety of frequencies selected from the entire range of measured data (1 frequency per decade) for the northern section of the data, including profiles A, B, C, and D (Figure 12) and for the southern section of the data, profiles F,G, and H (Figure 13). The induction vectors of the measured data at the specific ZTEM frequencies are shown in Figure 14 (northern sites) and Figure 15 (southern sites). The low tipper magnitude and high degree of scatter at the ZTEM frequencies is consistent with the decomposition analysis that showed nearly all of the sites to have a maximum phase difference between the TE and TM-modes to be less than 10 degrees at periods below 0.1 seconds, suggesting that the data are independent of the geoelectric strike angle and can be considered 1-dimensional (Spratt and Craven, 2009).

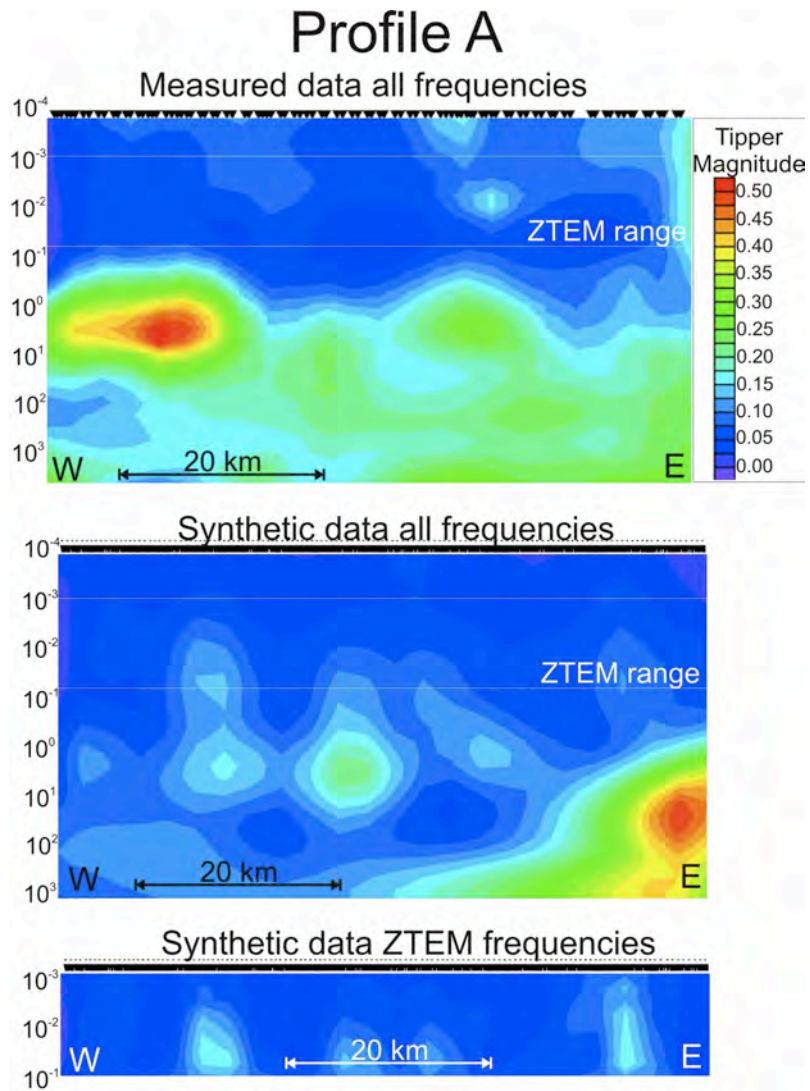


**Figure 5:** Pseudo-sections of the tipper data as function of frequency for profile A. (a) shows the 2007 MT measured data, the white box marks the ZTEM frequency range (b) shows the synthetic data derived from the 2-D models over the whole measurable frequency range, and (c) shows the synthetic data at the 6 specific ZTEM frequencies.

## Profile B

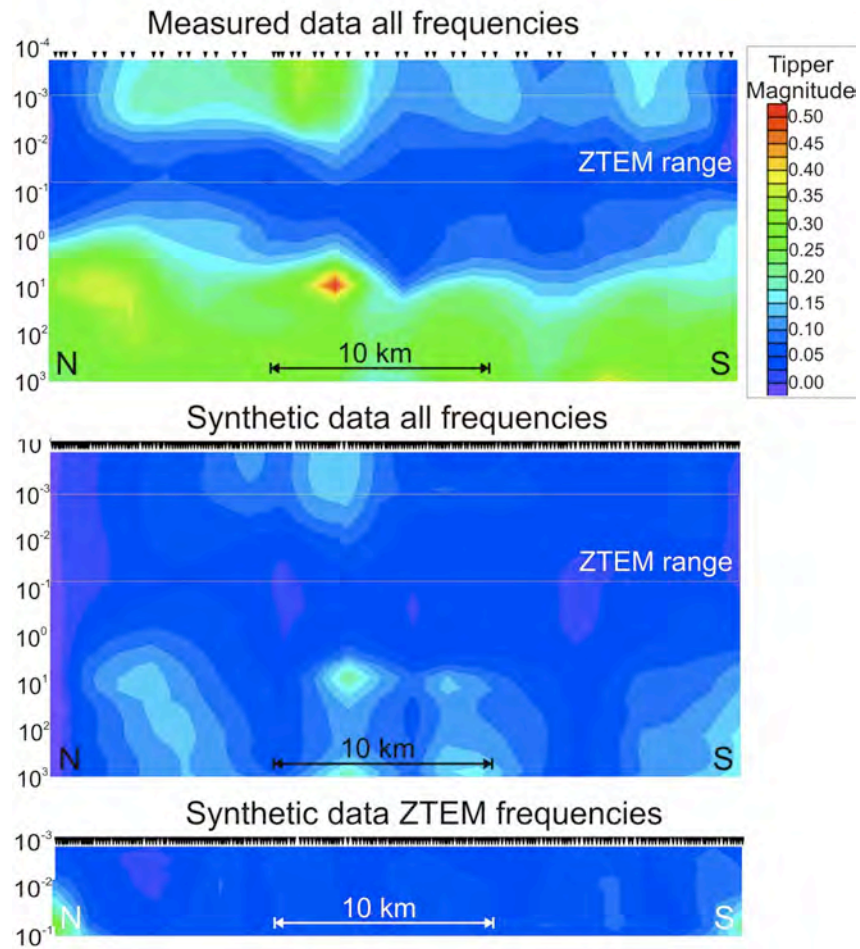


**Figure 6:** Pseudo-sections of the tipper data as function of frequency for profile B. (a) shows the 2007 MT measured data, the white box marks the ZTEM frequency range (b) shows the synthetic data derived from the 2-D models over the whole measurable frequency range, and (c) shows the synthetic data at the 6 specific ZTEM frequencies.

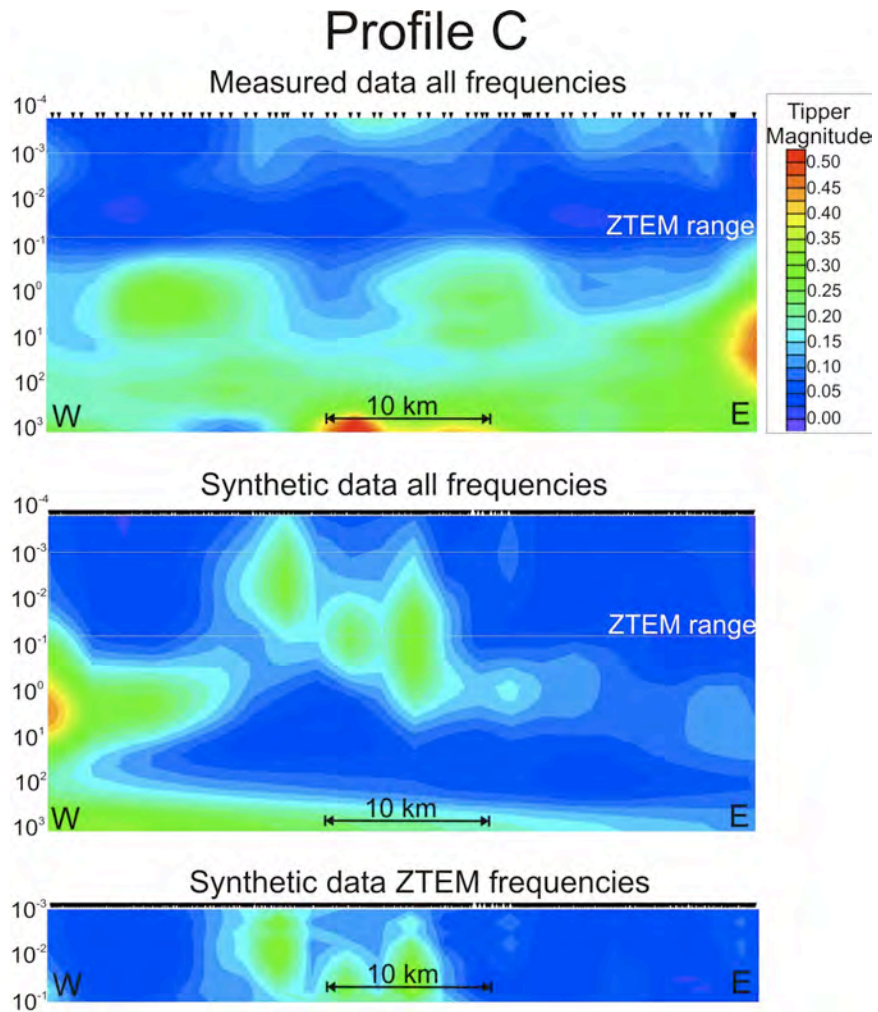


**Figure 7:** Pseudo-sections of the tipper data as function of frequency for profile C. (a) shows the 2007 MT measured data, the white box marks the ZTEM frequency range (b) shows the synthetic data derived from the 2-D models over the whole measurable frequency range, and (c) shows the synthetic data at the 6 specific ZTEM frequencies.

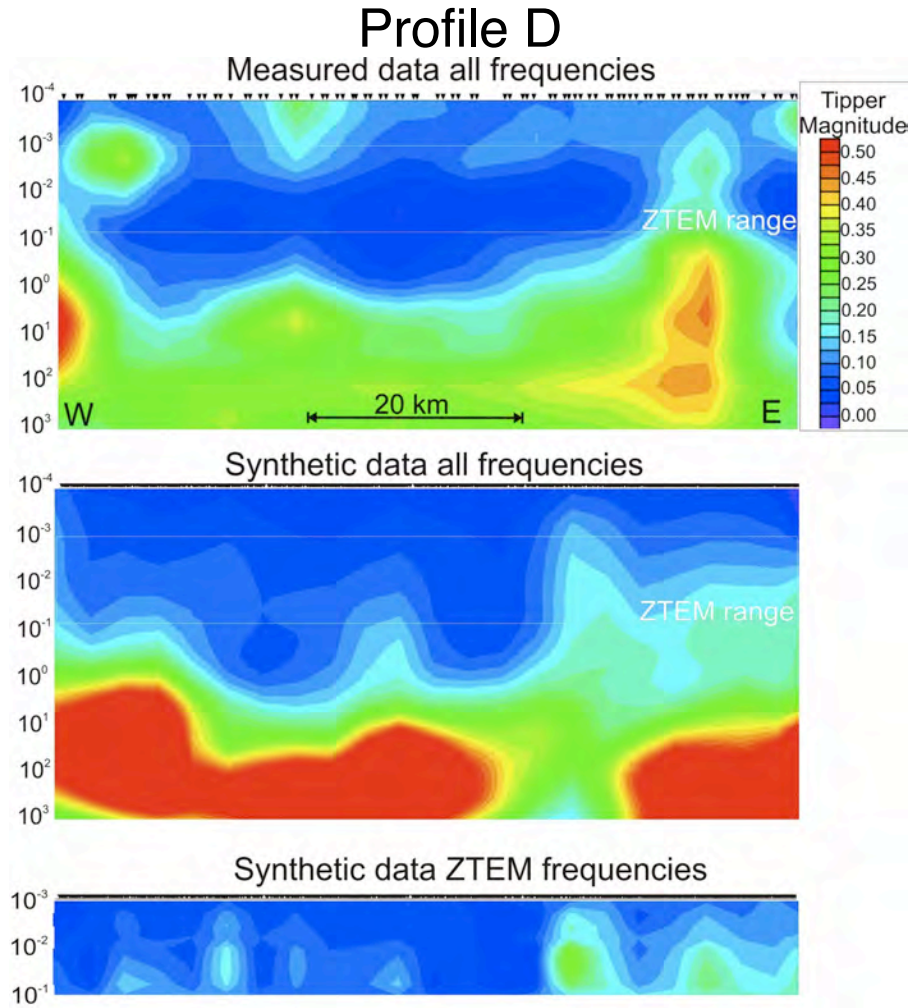


**Figure 8:** Pseudo-sections of the tipper data as function of frequency for profile D. (a) shows the 2007 MT measured data, the white box marks the ZTEM frequency range (b) shows the synthetic data derived from the 2-D models over the whole measurable frequency range, and (c) shows the synthetic data at the 6 specific ZTEM frequencies.

# Profile F

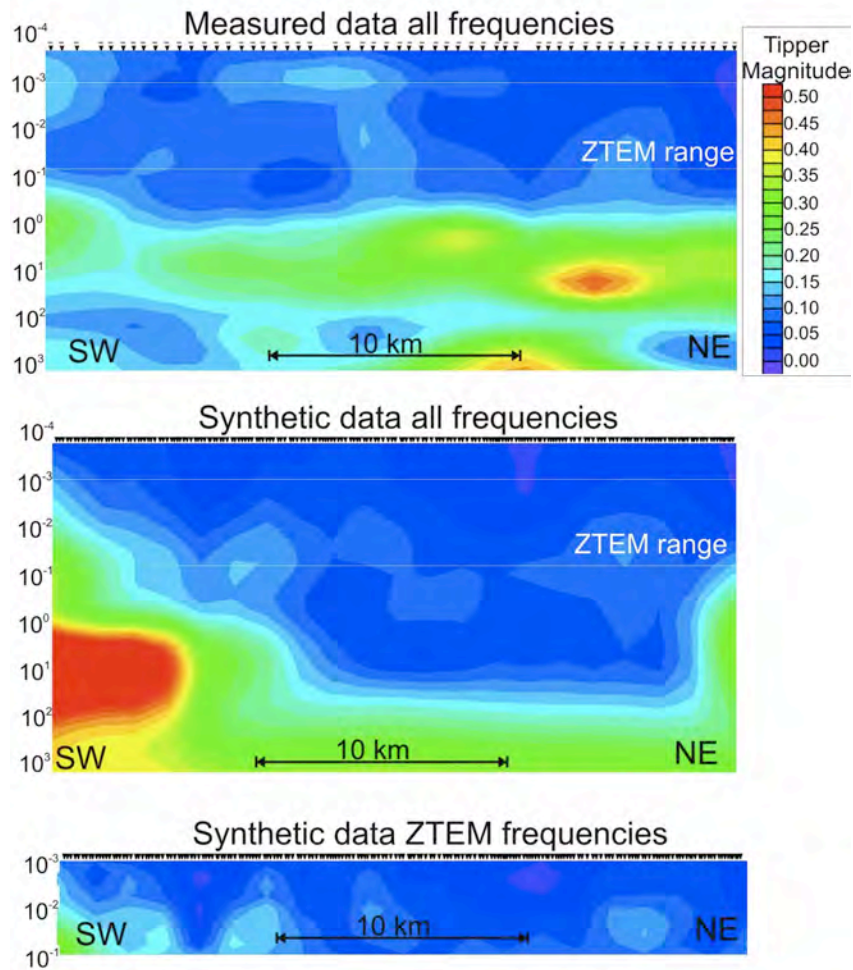


**Figure 9:** Pseudo-sections of the tipper data as function of frequency for profile F. (a) shows the 2007 MT measured data, the white box marks the ZTEM frequency range (b) shows the synthetic data derived from the 2-D models over the whole measurable frequency range, and (c) shows the synthetic data at the 6 specific ZTEM frequencies.

# Profile G

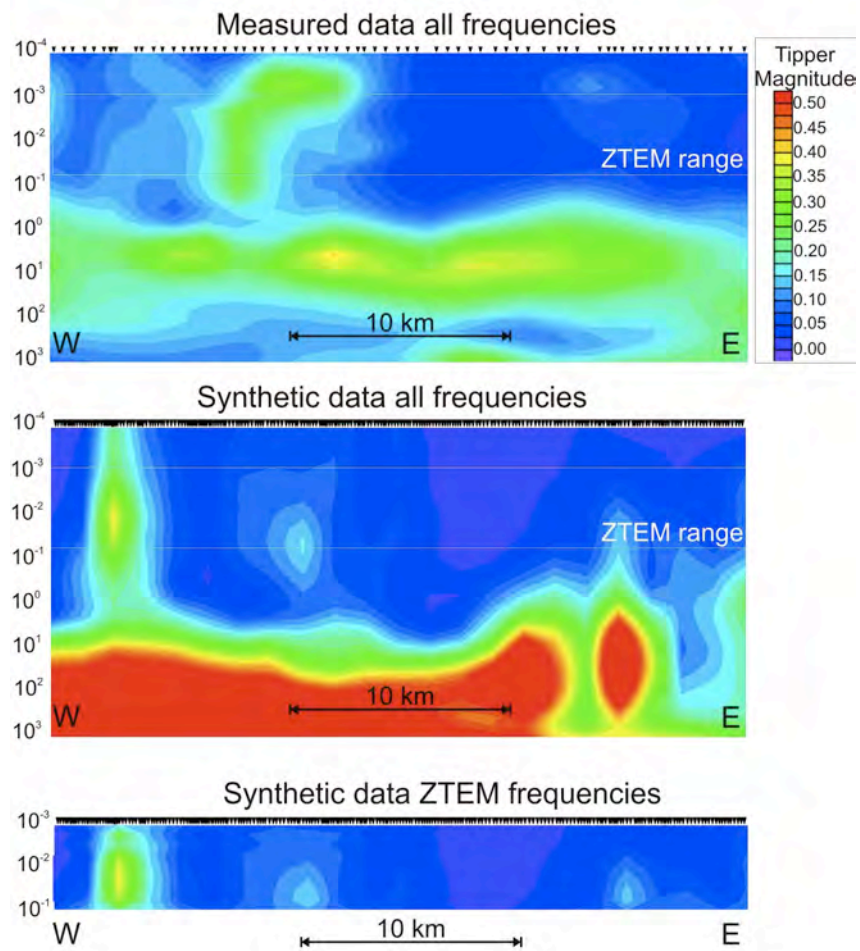


**Figure 10:** Pseudo-sections of the tipper data as function of frequency for profile G. (a) shows the 2007 MT measured data, the white box marks the ZTEM frequency range (b) shows the synthetic data derived from the 2-D models over the whole measurable frequency range, and (c) shows the synthetic data at the 6 specific ZTEM frequencies.



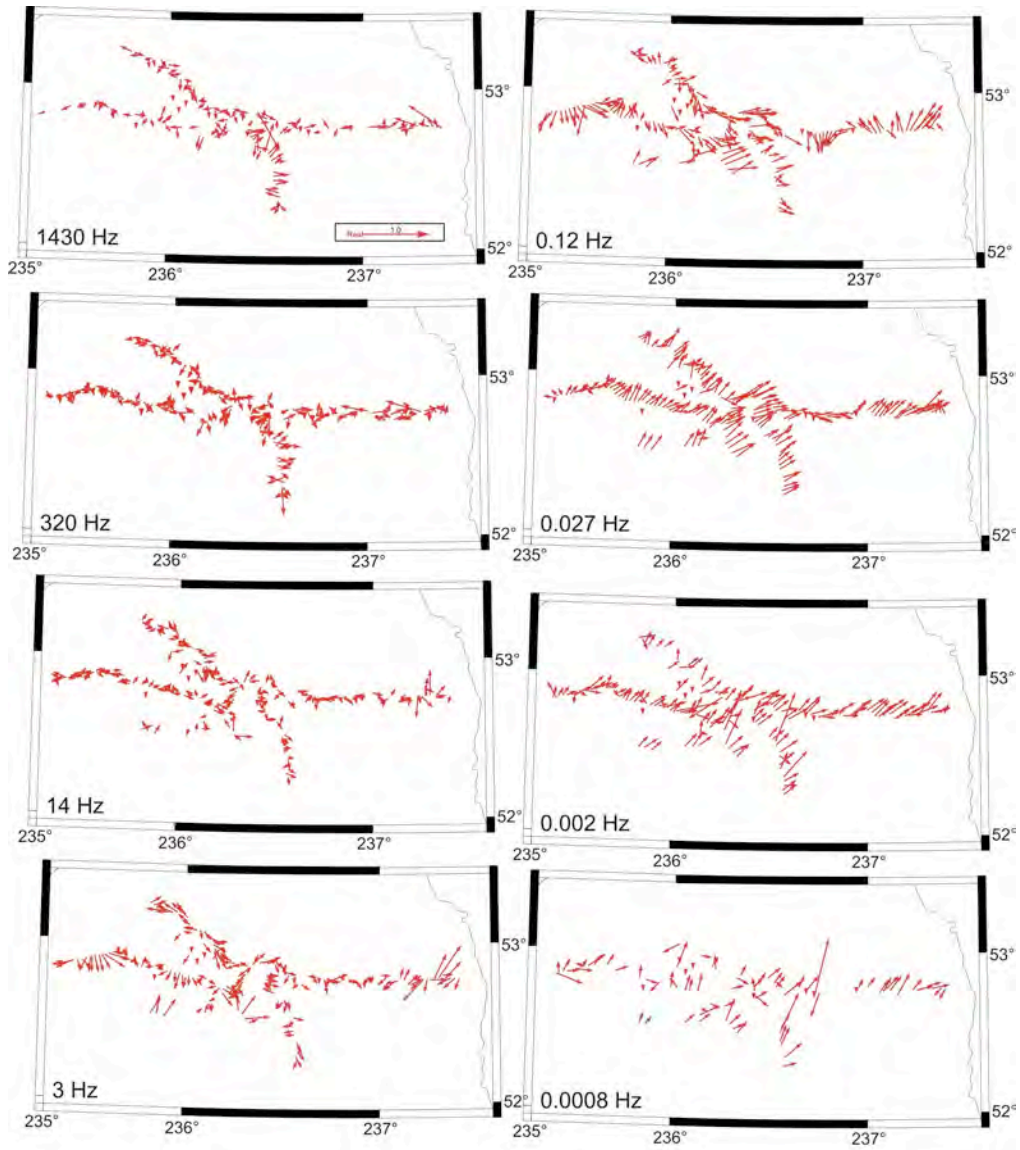


**Figure 12:** Plots of induction vectors of the 2007 measured MT data at the northern part of the MT survey area (includes profiles A, B, C, and D) at various frequencies. Plots are shows at one frequency per decade of measured data: 1430 Hz, 320 Hz, 14 Hz, 3 Hz, 0.12 Hz, 0.027 Hz, 0.002 Hz, and 0.0008 Hz.

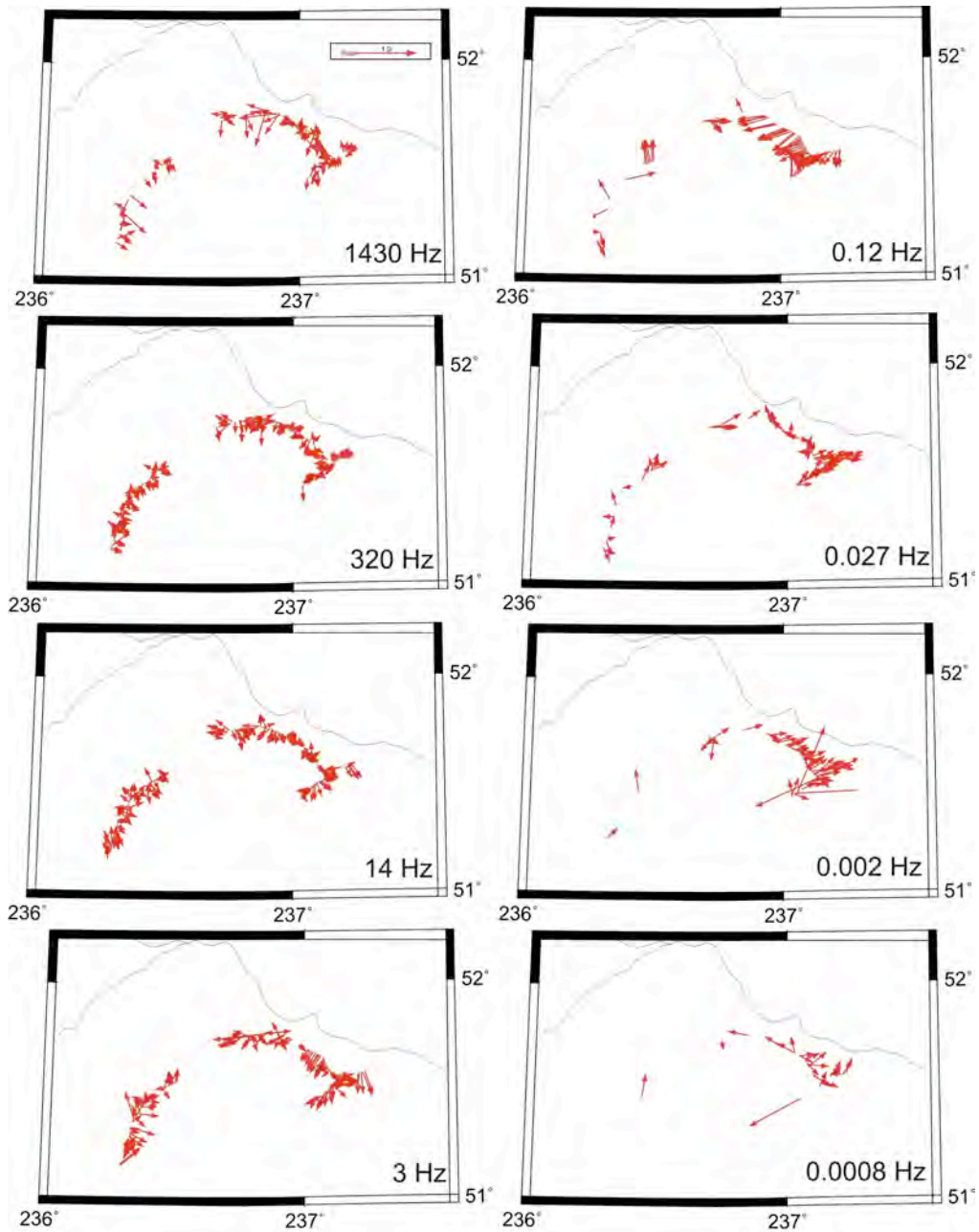


**Figure 13:** Plots of induction vectors of the 2007 measured MT data at the southern part of the MT survey area (includes profiles F, G, and H) at various frequencies. Plots are shown at one frequency per decade of measured data: 1430 Hz, 320 Hz, 14 Hz, 3 Hz, 0.12 Hz, 0.027 Hz, 0.002 Hz, and 0.0008 Hz.

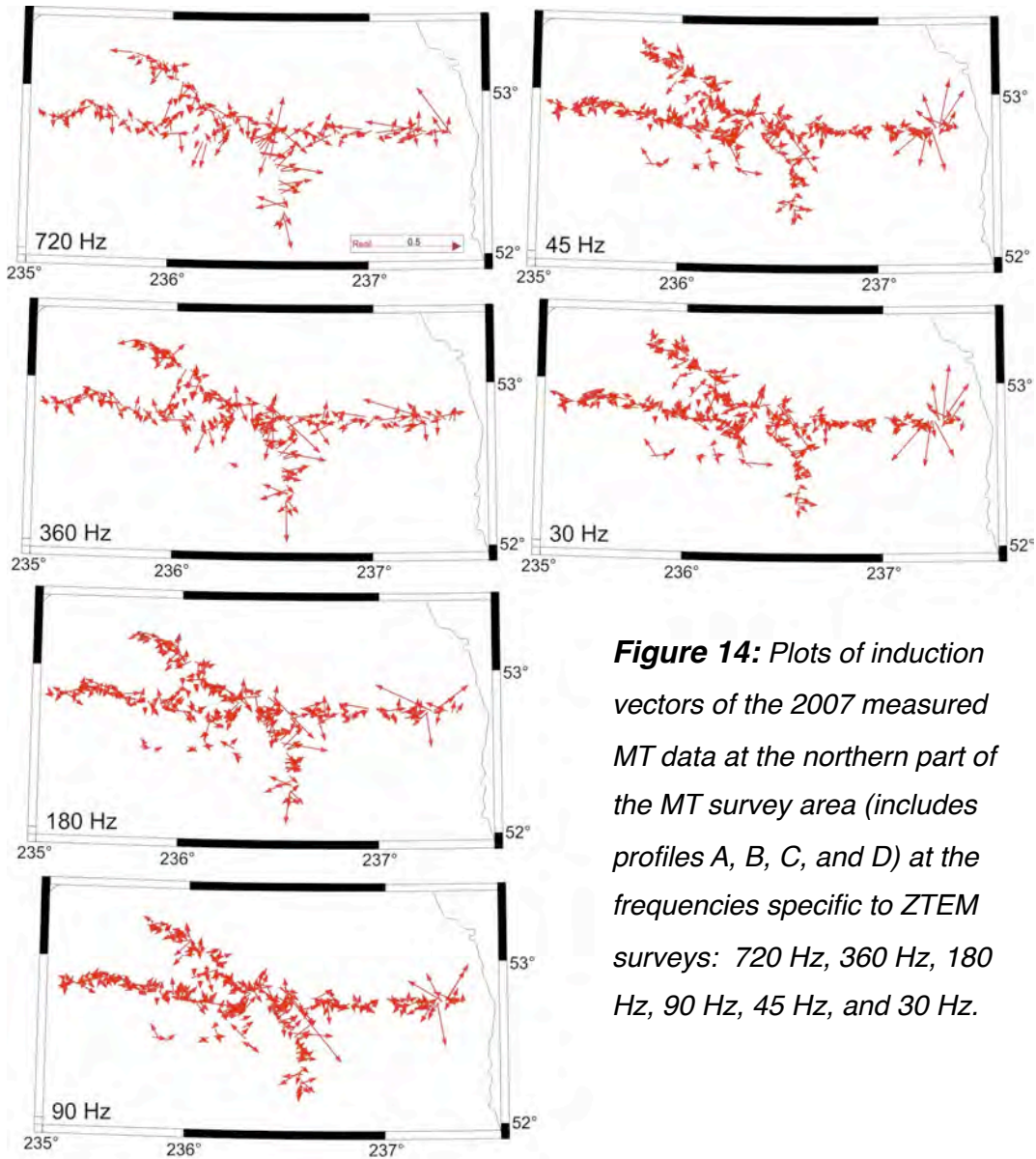


**Figure 14:** Plots of induction vectors of the 2007 measured MT data at the northern part of the MT survey area (includes profiles A, B, C, and D) at the frequencies specific to ZTEM surveys: 720 Hz, 360 Hz, 180 Hz, 90 Hz, 45 Hz, and 30 Hz.

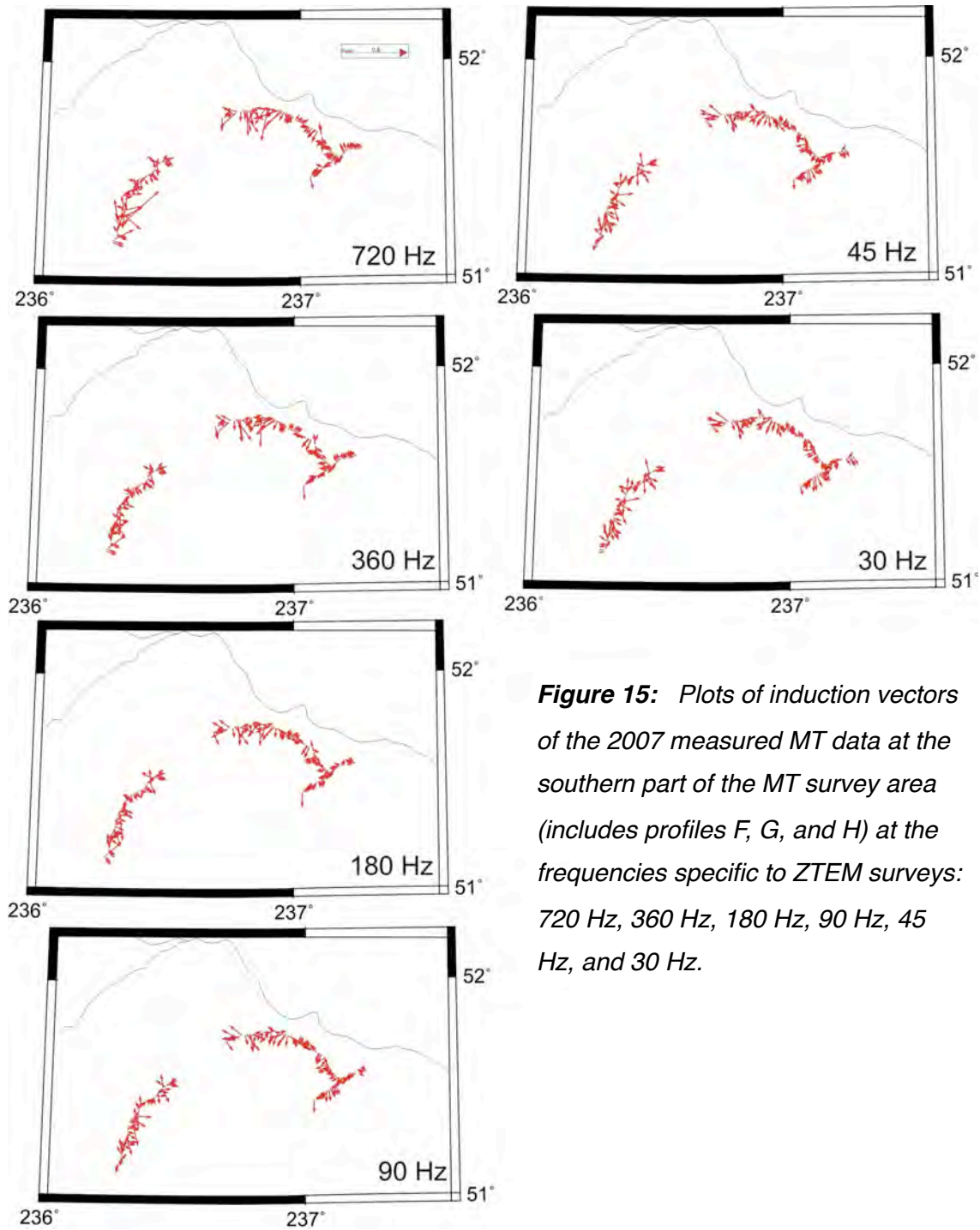


**Figure 15:** Plots of induction vectors of the 2007 measured MT data at the southern part of the MT survey area (includes profiles F, G, and H) at the frequencies specific to ZTEM surveys: 720 Hz, 360 Hz, 180 Hz, 90 Hz, 45 Hz, and 30 Hz.

Several 2-D conductivity models have been generated along the seven main MT profiles, using either the measured or the synthetic transfer-function data and the various frequency ranges. More than 200 iterations have been employed in the inversion for each model and each inversion was initiated with a uniform half space of 500 Ohm•m as a starting model. The iterations were stopped and restarted repeatedly, changing various inversion parameters until the conductivity structure most closely resembled the original 2-D model while still fitting the data. The inversions of measured data applied a smoothing value ( $\tau$ ) of 3, a Tyz absolute data-error floor of 0.01 and existing data errors. Each inversion of synthetic data used a  $\tau$  of 3, a Tyz absolute data-error floor of 0.001 and a standard deviation error of 1%.

Figures 16 to 22 show results of the various inversions for each profile as well as the original 2-D model derived from all three components of the data measured at each MT site location over the entire measured frequency range. Models derived using only the TF component of the measured data over the entire frequency range serve as a benchmark against which the results obtained from the synthetic ZTEM data can be measured. The subset of the measured vertical-field MT data that corresponds to the frequency range appropriate for ZTEM surveys has been modelled to show what can be obtained from ZTEM data were they to be collected along the MT profiles. Data measured on the ground represent the best possible conditions and will yield response curves with lower errors, however the data are limited to the site locations at a spacing of 200 – 500 m. Also shown are models generated using only the TF component of the synthetic data over the entire measurable frequency range (0.001–10000 Hz), at the recordable ZTEM frequency range (22–2800 Hz) and at the specific frequency used in ZTEM surveys (30, 45, 90, 180, 360, 720 Hz), all at a site spacing of < 100 m. For some profiles, models of synthetic TF data at the MT measured site spacing of ~ 500 m using the entire frequency range are also shown.

Modelling the transfer functions from measured MT data alone does not appear to resolve the subsurface-conductivity structure along any of the profiles, regardless of the frequency range that was inverted (Figures 16c, 16d, 17b, 17c, 18b, 18c, 19b, 19c, 20b,

20c, 21b, 21c, 22b, 22c). At the higher frequencies ranges, this may be due to the 1-D nature of the data. At the broader frequency ranges this may be a consequence of inherent errors associated with real data and, if so, it should be noted that we expect the airborne data to have higher errors. These results could also be due to the large station spacing (200 – 500 m) of the ground survey, compared to that of the airborne ZTEM surveys (~ 8 m).

#### *Profile A:*

Figure 16 shows the original 2-D model (Figure 16a) and the results of 2-D modelling of measured and synthetic TF data along profile A. In order to test the modelling parameters applied, a model was generated along profile A by inverting all three components of the synthetic MT data: TM-mode, TE-mode and transfer-function, TF, data (Figure 16b). When compared to the original 2-D model, the synthetic data show good resolution of the subsurface-conductivity structure, indicating that the modelling program and selected parameters are capable of generating an accurate image of the subsurface conductivity structure.

Inverting the synthetic TF data over the entire frequency range does not appear to resolve the subsurface conductivity structure (Figure 16e). Models of the synthetic TF data using frequencies limited to the ZTEM range at the measured site spacing of ~ 500 m, do not adequately image the structure (Figure 16f), however, at a site spacing of 100 m, the TF data at the ZTEM range reveal features that are similar to the original 2-D model and show reasonable conductivity values at appropriate depths and image significant structural detail (Figure 16g). This resolution is lost when further limiting the frequencies to the six ZTEM frequencies (Figure 16h). An additional model was generated for a small section at the easternmost end of profile A using synthetic TF data at a site spacing of 25 m (Figure 16j) to determine whether a denser station spacing would further resolve the conductivity structure. This was compared to images of focussed inversions generated from measured TE, TM, and TF data for this section of

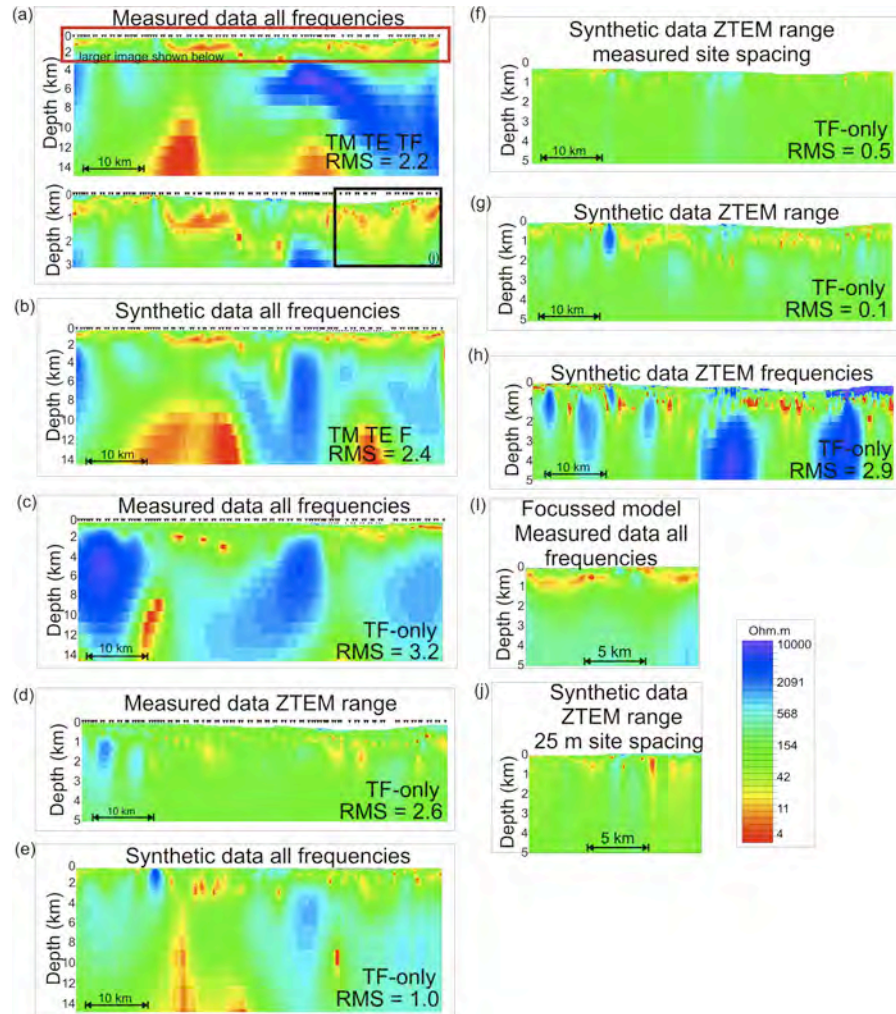


**Figure 16:** Results of two-dimensional modelling of measured and synthetic MT data along profile A. (a) shows the original 2-D model derived from all components of the measured MT data, the black box marks the section shown in i and j, (b) model of all three components of the synthetic data over 7 decade frequency range, (c) model of the measured TF data over the 7 decade frequency range, (d) model of the measured TF data over the ZTEM frequency range, (e) model of the synthetic TF data the 7 decade frequency range at a site spacing of 100 m, (f) model of the synthetic TF data over the ZTEM frequency range using a site spacing similar to the measured data, (g) model of the synthetic TF data over the ZTEM frequency range at a site spacing of 100m, (h) model of the synthetic data over the specific 6 ZTEM frequencies at site spacing of 100m, (i) focussed model of a section of profile A using all components of the measured MT data, and (j) model of section of profile with a site spacing of 25m, using synthetic data TF data at the ZTEM frequency range.

profile A (Figure 16i). The resulting model was much smoother, but the structural resolution did not improve with a higher station density suggesting that a spacing of 100 m is adequate for assessing ZTEM data.

Along profile A, a minimum site spacing of 100 m and transfer function data over a broad frequency range (0.001 – 10000 Hz) is required to reveal the general conductivity structure of the subsurface.

*Profile B:*

Figure 17 shows the original 2-D model (Figure 17a) and the results of 2-D modelling of measured and synthetic TF data along profile B. Models of the synthetic TF data using frequencies over the whole range at the measured site spacing of ~500 m, in this case, show strong similarities to the original 2-D model (Figure 17d), imaging a highly conductive layer consistent with the interpretation of Eocene volcanoclastics to the north and Cretaceous sedimentary rock to the south (Figure 2b). This suggests that a site spacing of 500 m is enough to image the general subsurface structure. The synthetic TF data over the entire frequency range at a site spacing of 100 m reveals the general subsurface-conductivity structure, including the highly conductive Eocene volcanoclastic rocks at the north end of the profile and the laterally variable and moderate conductivities of the Cretaceous sediments over the southern half of the profile, and it shows an appropriate basin depth of beneath the entire profile (Figure 17e). Results using both the ZTEM range and the six specific ZTEM frequencies show the highly conductive Eocene units, but these are only observed to depths of <200 m (Figure 17f and g). The Cretaceous sedimentary rocks are imaged as laterally variable and moderately conductive in the ZTEM-based models (Figure 17f and g), consistent with the key signature observed in the original MT data-based models; however, the overall structure and specific conductivity variations within this unit are significantly different from the original 2-D model.

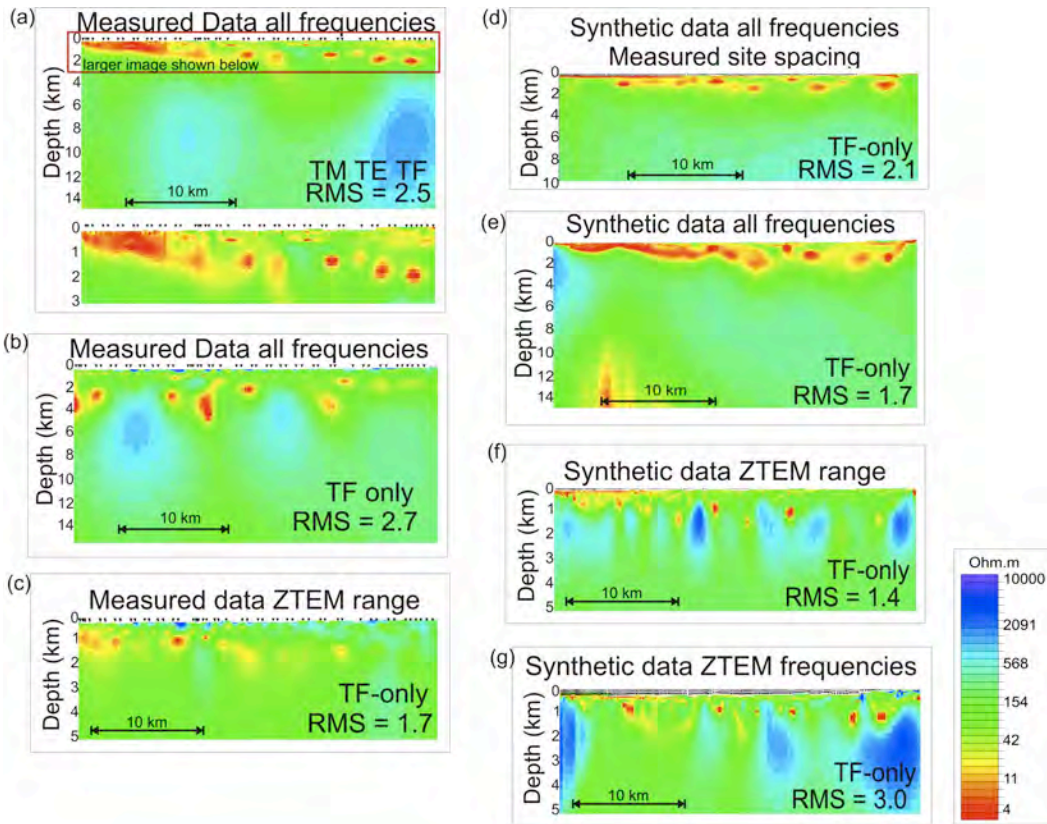


**Figure 17:** Results of two-dimensional modelling of 2007 measured MT data and synthetic MT data along profile B. (a) shows the original 2-D model derived from all components of the measured MT data, (b) model of the measured TF data over the 7 decade frequency range, (c) model of the measured TF data over the ZTEM frequency range, (d) model of the synthetic TF data the 7 decade frequency range at a site spacing of 100 m, (e) model of the synthetic TF data over the ZTEM frequency range using a site spacing similar to the measured data, (g) model of the synthetic TF data over the ZTEM frequency range at a site spacing of 100 m, and (h) model of the synthetic data over the specific 6 ZTEM frequencies at site spacing of 100 m.

Along profile B, a minimum site spacing of  $\sim 500$  m and a broad frequency range is required to image the conductivity structure to depths over 200m. The synthetic transfer function data at the ZTEM range and even the specific ZTEM frequencies can distinguish between the conductivity signatures typically associated with those of the Eocene volcanoclastics and those of the Cretaceous sediments at shallow depths, however, the structural features are not well resolved.

### *Profile C:*

Figure 18 shows the original 2-D model (Figure 18a) and the results of 2-D modelling of measured and synthetic TF data along profile C. These show that the synthetic data resolve well the resistive Hazelton Group units to reasonable depths of 2–3 km, regardless of the frequency distribution that is inverted (Figure 18d–f). The lateral continuity of the moderate conductivities at the southeastern end of the profile, interpreted as Cretaceous sedimentary rocks, is broken but the conductivity values are significantly lower ( $<4 \text{ Ohm}\cdot\text{m}$ ), closer to those of the Eocene groups. In addition, the overall structure and distribution of conductivity variations is different from that of the original 2-D model, particularly when using the six ZTEM frequencies (Figure 18f). The moderate conductivities at the northwestern end of the profile were interpreted as Eocene and/or Cretaceous groups in the original 2-D model because the conductivity signature was difficult to classify (Figure 18a). Although the synthetic data inverted over the ZTEM range image this feature reasonably well, the model including just the six ZTEM frequencies shows a laterally uniform, highly conductive unit that would be interpreted as Eocene volcanoclastic rocks (Figure 18f).

Along profile C, the general conductivity structure is revealed and the signatures associated with the various rocks types can be identified using synthetic transfer function data at the ZTEM range (22 – 2800 Hz), but not when limiting the frequencies to those specific to ZTEM surveys. In all examples the absence of an enhanced conductivity unit can be identified.

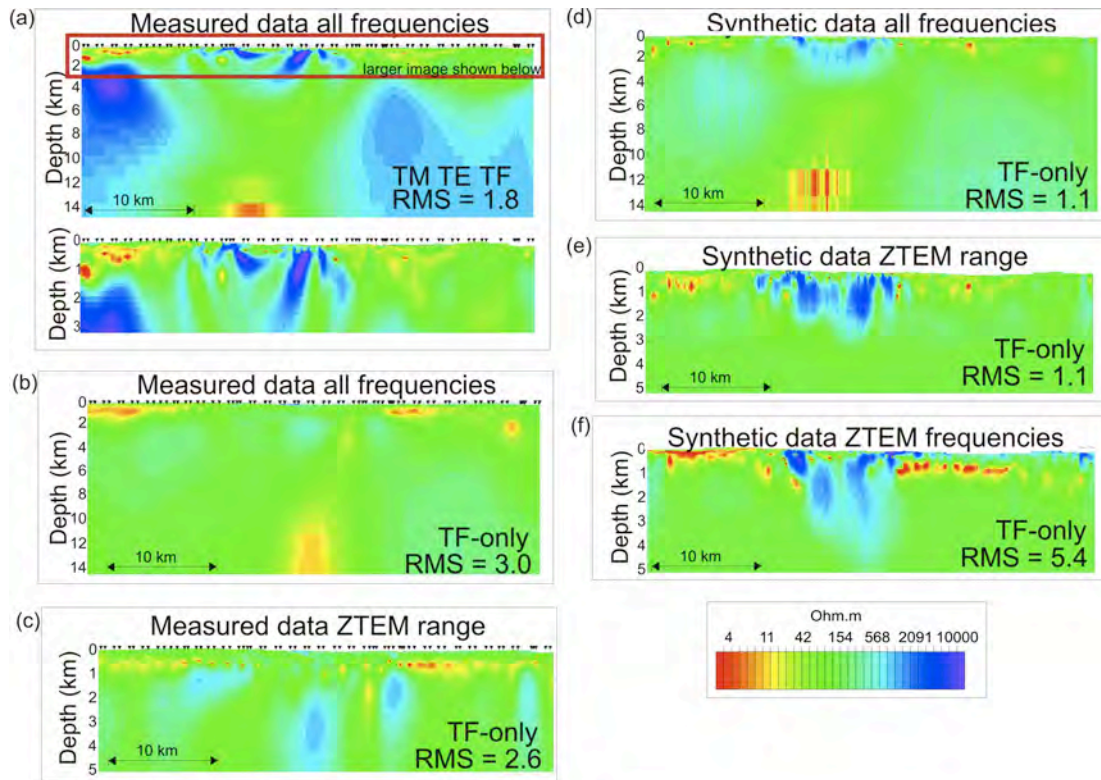


**Figure 18:** Results of two-dimensional modelling of 2007 measured MT data and synthetic MT data at a site spacing of 100 m along profile C. (a) shows the original 2-D model derived from all components of the measured MT data, (b) model of the measured TF data over the 7 decade frequency range, (c) model of the measured TF data over the ZTEM frequency range, (d) model of the synthetic TF data the 7 decade frequency range, (e) model of the synthetic TF data over the ZTEM frequency range, and (f) model of the synthetic data over the specific 6 ZTEM frequencies.

**Profile D:**

Figure 19 shows the original 2-D model (Figure 19a) and the results of 2-D modelling of measured and synthetic TF data along profile D. Inversions of the synthetic TF data over the whole measured frequency range (Figure 19d) result in a conductivity structure that strongly resembles that of the original 2-D model to depths of  $\sim 4$  km, but the deeper structure is not well resolved. The synthetic data over the ZTEM range results in a reasonable image of the Eocene volcanoclastic over most of the profile, however the

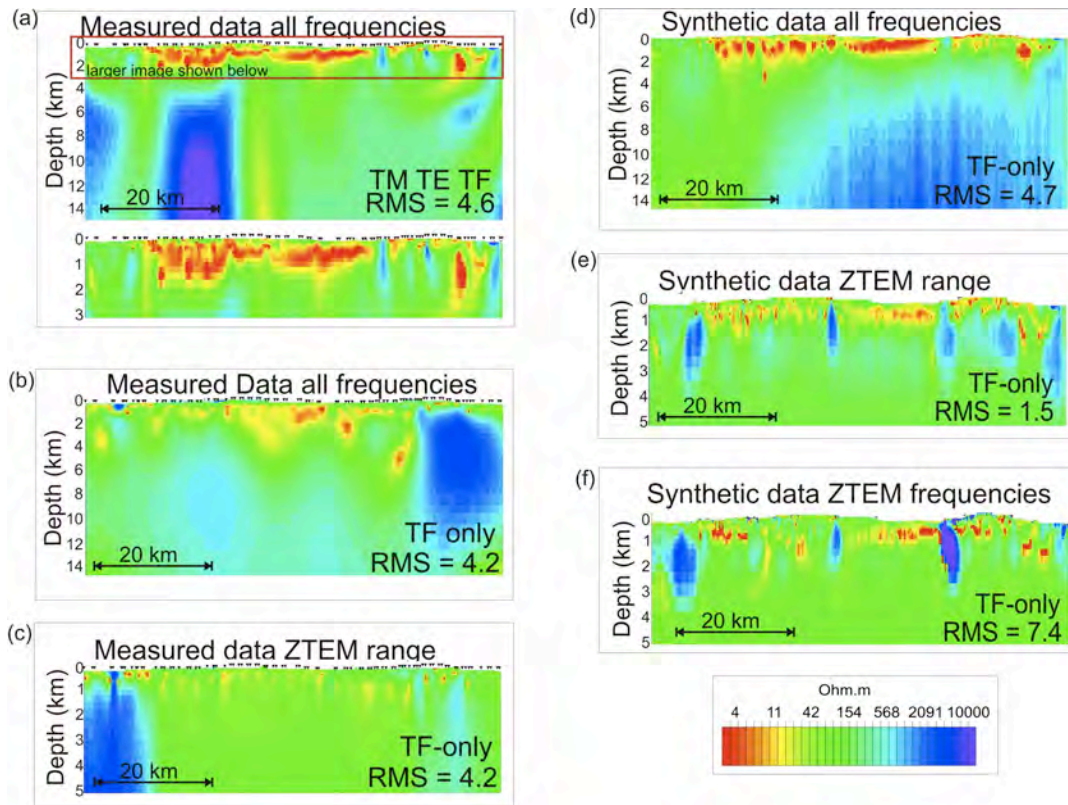


**Figure 19:** Results of two-dimensional modelling of 2007 measured MT data and synthetic MT data at a site spacing of 100 m along profile D. (a) shows the original 2-D model derived from all components of the measured MT data, (b) model of the measured TF data over the 7 decade frequency range, (c) model of the measured TF data over the ZTEM frequency range, (d) model of the synthetic TF data the 7 decade frequency range, (e) model of the synthetic TF data over the ZTEM frequency range, and (f) model of the synthetic data over the specific 6 ZTEM frequencies.

lateral continuity of the unit is broken up compared to the original model, particularly in the eastern half of the profile (Figure 19e). Inversions of the synthetic data at the specific ZTEM frequencies reveal a conductive layer to appropriate depths of 2 km, but the overall continuity and structure of the unit is lost (Figure 19f).

Along profile D, a broad frequency range of synthetic transfer function data is required to adequately image the subsurface conductivity structure and identify the units.

*Profile F:*

Figure 20 shows the original 2-D model (Figure 20a) and the results of 2-D modelling of measured and synthetic TF data along profile F. Here, consistent with borehole lithology, the original 2-D model reveals Cretaceous Taylor Creek sedimentary rocks to depths of 2–3 km (Figure 3a). Inversion of the synthetic TF data over the whole frequency range shows laterally variable conductivities that are comparable to those associated with Cretaceous sedimentary rocks (Figure 20d). The resolution of the general structure, distribution of the conductivity variations and depth of the units, is poor when using data at the ZTEM range (Figure 20e), particularly with just the six ZTEM frequencies (Figure 20f).

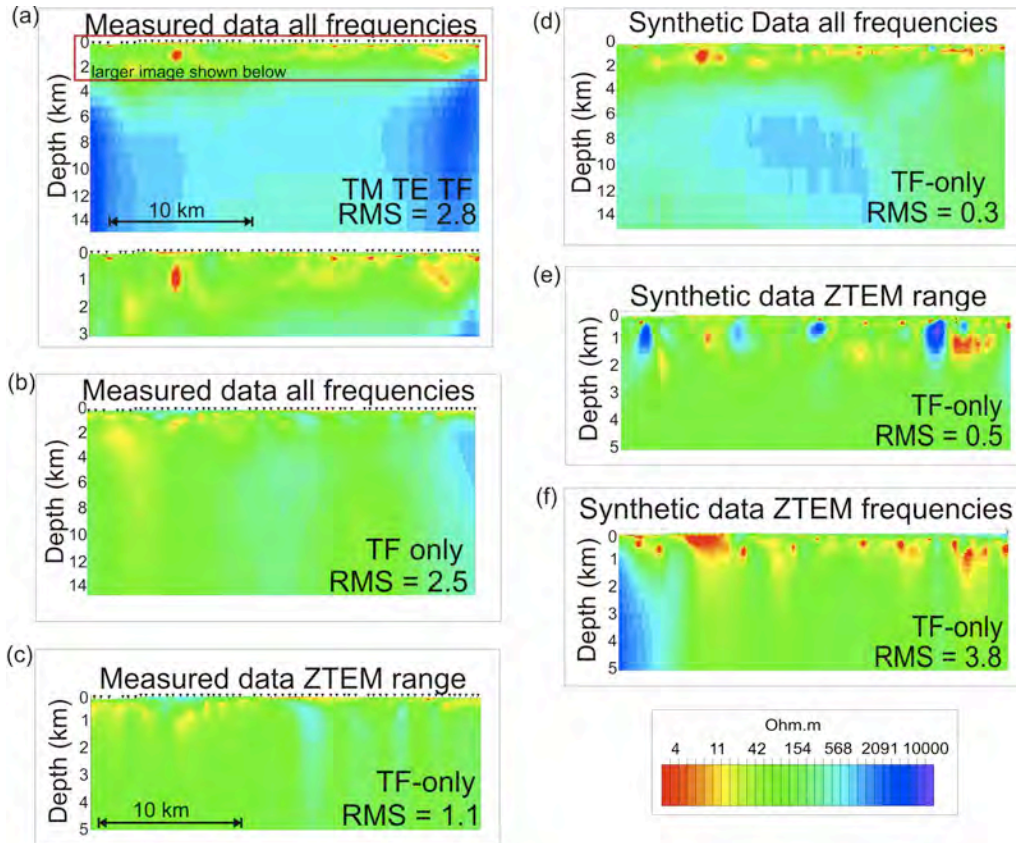
Along profile F, a broad frequency range is required for the synthetic transfer function data to adequately image the subsurface structure, however it may be possible to identify the conductivity signature typical of the Cretaceous sedimentary units using the ZTEM frequency range (22 – 2800 Hz), but not when limited to the 6 ZTEM frequencies.

*Profile G:*

Figure 21 shows the original 2-D model (Figure 21a) and the results of 2-D modelling of measured and synthetic TF data along profile G. Inversion of the synthetic TF data over the whole frequency range (Figure 21d) shows laterally continuous high conductivity values that are comparable to those associated with Eocene volcanoclastics rocks as interpreted in the original 2-D model (Figure 3b). Again, similar to profile F, the general structure, lateral continuity of the unit and thickness of the layer, is poorly resolved when using data at the ZTEM range (Figure 21e), particularly with just the six ZTEM frequencies (Figure 21f).

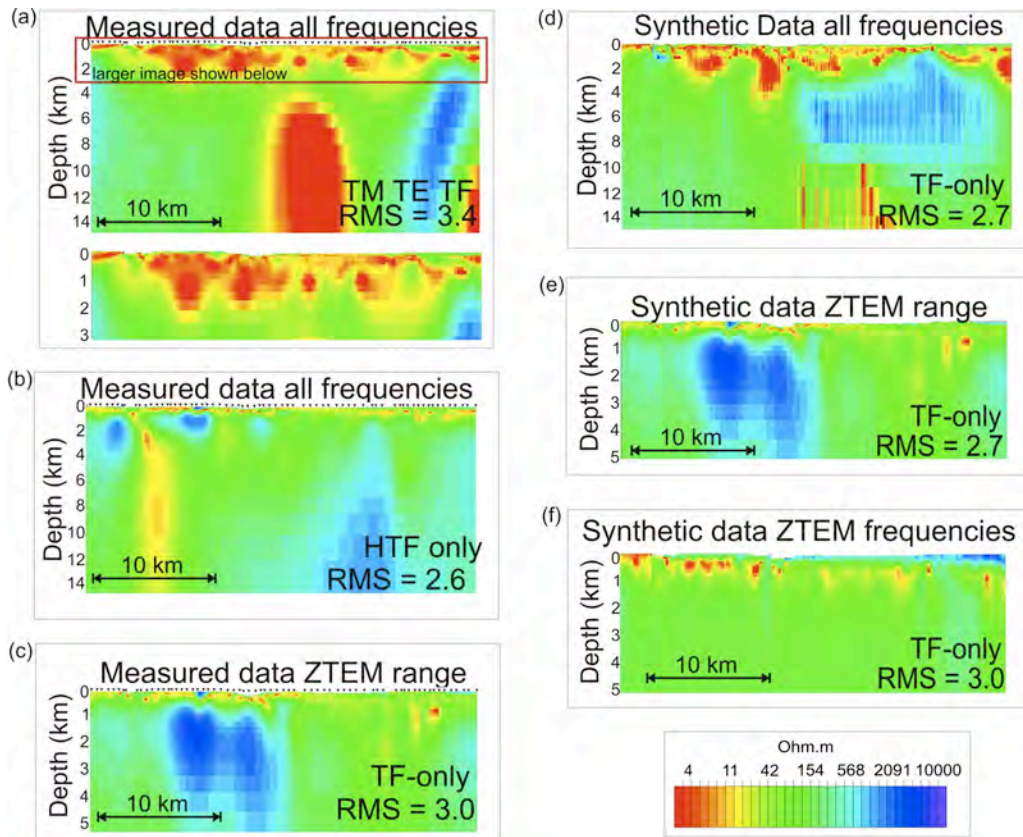
*Profile H:*

Figure 22 shows the original 2-D model (Figure 22a) and the results of 2-D modelling of



**Figure 20:** Results of two-dimensional modelling of 2007 measured MT data and synthetic MT data at a site spacing of 100 m along profile F. (a) shows the original 2-D model derived from all components of the measured MT data, (b) model of the measured TF data over the 7 decade frequency range, (c) model of the measured TF data over the ZTEM frequency range, (d) model of the synthetic TF data the 7 decade frequency range, (e) model of the synthetic TF data over the ZTEM frequency range, and (f) model of the synthetic data over the specific 6 ZTEM frequencies.

measured and synthetic TF data along profile H. Inversion of the synthetic TF data over the whole frequency range (Figure 22d) shows some similarities to the original 2-D model in that there is a conductive layer in the upper 2 km, but the overall structure is not comparable. Results of inversions using the TF data at the ZTEM range (Figure 22e) and the ZTEM frequencies (Figure 22f) do not reveal the features observed in the original 2-D model.



**Figure 21:** Results of two-dimensional modelling of 2007 measured MT data and synthetic MT data at a site spacing of 100 m along profile G. (a) shows the original 2-D model derived from all components of the measured MT data, (b) model of the measured TF data over the 7 decade frequency range, (c) model of the measured TF data over the ZTEM frequency range, (d) model of the synthetic TF data the 7 decade frequency range, (e) model of the synthetic TF data over the ZTEM frequency range, and (f) model of the synthetic data over the specific 6 ZTEM frequencies.

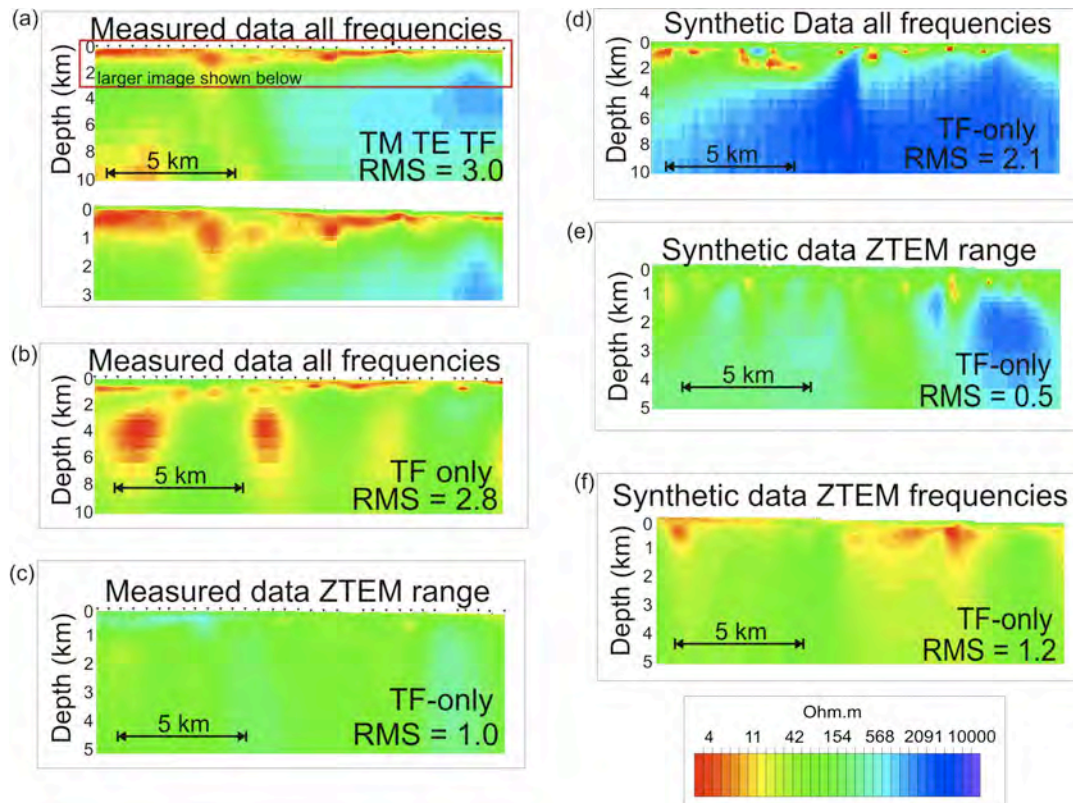


**Figure 22:** Results of two-dimensional modelling of 2007 measured MT data and synthetic MT data at a site spacing of 100 m along profile H. (a) shows the original 2-D model derived from all components of the measured MT data, (b) model of the measured TF data over the 7 decade frequency range, (c) model of the measured TF data over the ZTEM frequency range, (d) model of the synthetic TF data the 7 decade frequency range, (e) model of the synthetic TF data over the ZTEM frequency range, and (f) model of the synthetic data over the specific 6 ZTEM frequencies.

## Conclusions from 2-D modelling

Inversions of synthetic data indicate that modelling the transfer-function data alone can give a reasonable image of the conductivity structure of the subsurface; however, revealing specific features at depth is highly dependent on the frequencies included in the inversion. In specific geological terranes, where the depth to target, conductivity value and structure are suitable, the ZTEM method may be very useful in imaging the

conductivity structure. Within the Nechako Basin, the thickness of units, conductivity values and lateral structures are highly variable. The ZTEM method may be capable of identifying the conductive Eocene volcanoclastic rocks to shallow depths but incapable of differentiating between the Eocene groups and the Cretaceous sedimentary rocks.

## **Integration of MT Derived Models in a Tectonic History of the Nechako Basin**

A paper was written, submitted, and published on the results and interpretations of the 2007 MT data: J. Spratt and J. Craven, Near-surface and crustal-scale images of the Nechako basin, British Columbia, Canada, from magnetotelluric investigations, Canadian Journal of Earth Sciences, 2011, vol. 48, no. 6, pp. 987 – 999. Images and discussion on coincident MT and seismic data contributed to a second publication in the same volume: A.J. Calvert, N.E. Hayes, J.E. Spratt, and J.A. Craven, Seismic reflection constraints on upper crustal structures in the volcanic-covered central Nechako basin, British Columbia Canadian Journal of Earth Sciences, 2011, Vol. 48, No. 6 : pp. 1021-1037 . It is hopeful that these publications will aid in the interpretation of other studies within the Nechako basin and help in understanding the tectonic history of the region.

## **Seismic Reprocessing**

### **Goals**

Multichannel seismic reflection profiles were collected by Geoscience BC in 2008 to better characterize the Nechako Basin, British Columbia. The profiles revealed a complicated network of variably deformed sub-basins interspersed with near-surface volcanic units (Calvert et al., 2011). To extract as much information from these data as possible, the goals of this Geoscience BC-funded project were to reprocess select

seismic reflection profiles and, where possible, assess whether information derived from coincident magnetotelluric (MT) models could be used to help in the seismic processing. Specifically, we aimed to:

1) Perform a standard reprocessing of select seismic reflection profiles to try to improve upon the earlier processing results

2) Convert the inverted resistivities in the MT models to seismic velocities using empirically-derived relationships from well logs and physical property studies of the major rock units in the Nechako region and assess whether the derived velocities could be useful for the reprocessing

3) Link lithological contacts within the MT models to reflective boundaries on the reprocessed seismic sections

## **Regional Setting**

The Nechako Basin consists of a broad region of sub-basins on the interior plateau of southern British Columbia between the Coast Mountains and the Rocky Mountains (Fig. 1). The nature of the Nechako Basin remains enigmatic, despite some limited effort at exploration in the 1980s, because the basin is overlain by more recent sedimentary, volcanic and glacial deposits. Recently, Geoscience BC has endeavored to better characterize the Nechako Basin using a multi-disciplinary approach involving geological mapping, rock property analyses, magnetotelluric soundings and multichannel seismic reflection imaging.

To complement the 1300 km of multichannel seismic reflection lines acquired by Canadian Hunter (CH) during the early 1980s exploration phase of the Nechako Basin, Geoscience BC acquired 330 km of new Vibroseis seismic reflection data in 2008. These data were of better quality than the CH data but nonetheless revealed similar reflectivity patterns consistent with highly variable subsurface geology with no regionally

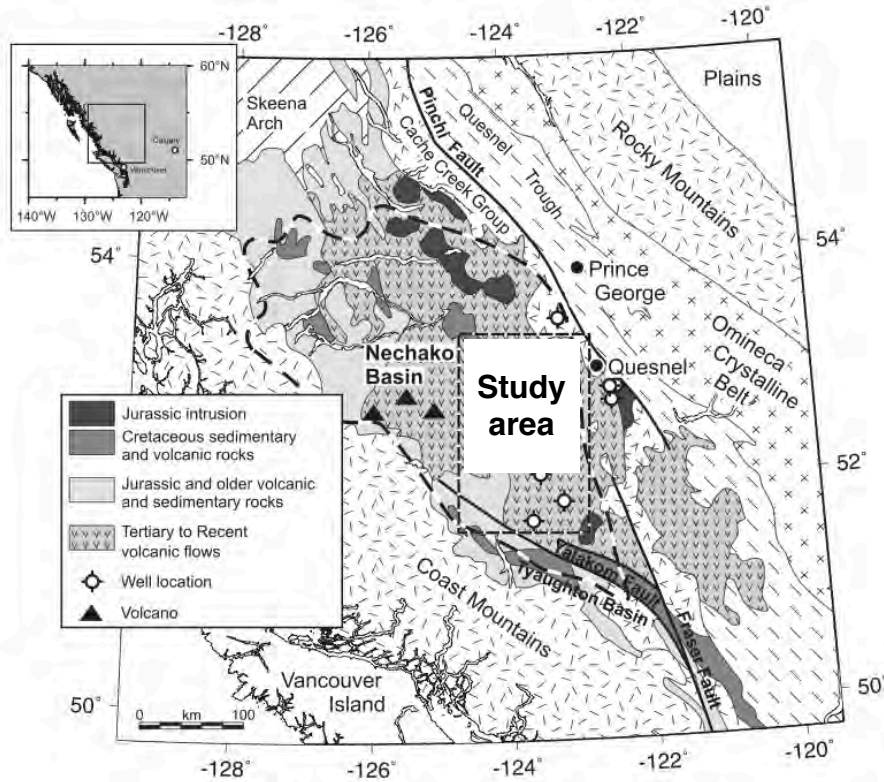


**Figure 23:** Regional geological map of southern British Columbia, adapted from Calvert et al., 2011. Study area highlighted with dashed black rectangle.

extensive stratigraphy discernible across the Nechako Basin (Calvert et al., 2011). Coincident magnetotelluric studies of the Nechako Basin have proven useful for delineating the depth extent of the volcanic units (Spratt and Craven, 2011) and so offer a complementary dataset against which to re-examine the Geoscience BC seismic reflection data. For our project, lines 2008-5, 2008-10, 2008-12 and 2008-13 have been reprocessed (Fig. 2). These four lines out of the original seven lines were specifically chosen to generate representative regional EW and NS cross-sections through the study area. As only two of these lines (2008-5 and 2008-10) corresponded with coincident magnetotelluric studies (profiles B and A, respectively), the usefulness of MT-derived information for reprocessing of multichannel seismic reflection data is only assessed for those two lines.

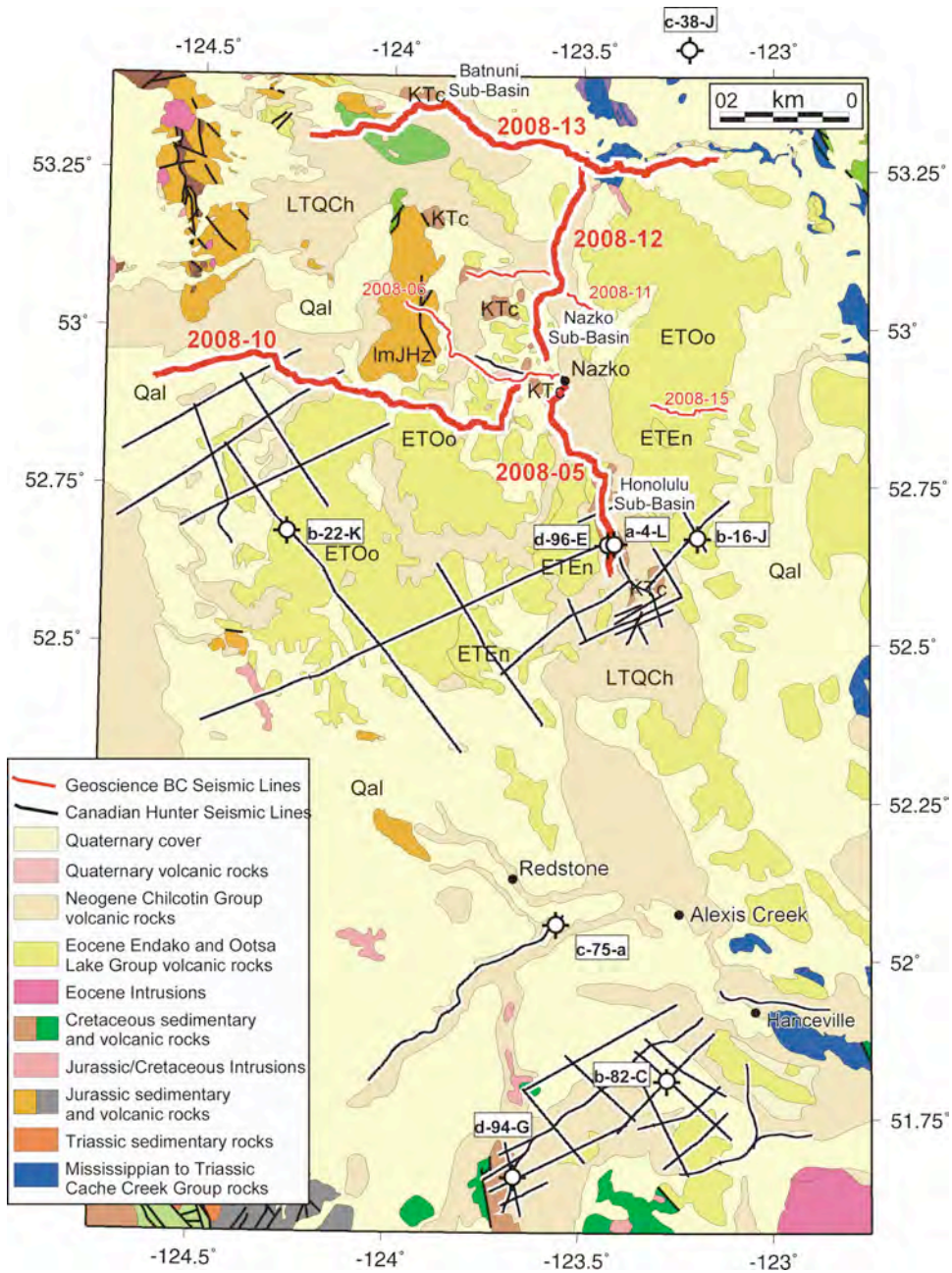


**Figure 24:** Detailed geological map of study area, adapted from Stiller (2006) and provided by Nathan Hayward and Andy Calvert (pers. comm., 2012). The Geoscience BC seismic lines reprocessed for this report are highlighted with thicker red lines.

# Standard Reprocessing of Vibroseis Data

## Overview

The Vibroseis data collected by Geoscience BC across the Nechako Basin, southern British Columbia, are of good quality but their ability to capture significant structures at depth is hampered by the geological complexity of the shallow subsurface and widespread occurrences of highly reflective near-surface volcanics. Consequently, the goals of the reprocessing of the data were to minimize noise where possible and generate as clear a stack as possible. To this end, a fairly standard processing flow, similar to that used by CGG Veritas for the original processing, was undertaken.

The reprocessing of the Geoscience BC data was performed using the Globe Claritas Seismic Processing Software from GNS Science in New Zealand. As the original processing was performed using CGG Veritas' in-house proprietary software, the processors used for both studies, while often similar, were not identical.

## Data

The multichannel seismic reflection data provided to Memorial University were 18 second extended correlated shot gathers and common midpoint (CMP) gathers containing both geometry and static information within the trace headers.

## Processing Summary

1. Amplitude Recovery:  $t^1 \times \text{offset}^{(0.8)}$
2. Crooked Line 2D Geometry (CMP interval: 10 m)
3. Frequency Filtering (10-20 Hz High Pass and 57-58-64-70 Hz Notch)
4. Tapered Front Mute (200 ms cosine on-taper past first break pick)

5. ~~Surface Consistent Deconvolution~~ (not applied)
6. Static Corrections
7. Sorting to Common Midpoint (CMP) Gathers
8. Automatic Gain Control (500 ms, Normal)
9. Velocity Analysis and Normal Moveout (NMO) Correction
10. Stack
11. Migration
12. Coherency Filtering



## Description of Key Processors

### Gain Recovery

In order to account for the seismic wave amplitude attenuation from geometrical spreading of the wavefront and energy dissipation, an empirically-derived gain of two-way travelttime ( $t^1$ ) multiplied by offset raised to the power of 0.8 ( $\text{offset}^{(0.8)}$ ) was applied to enhance reflections at late arrival times and far offsets. This gain was preferred over the  $t^{2.5}$  scaling used by CGG Veritas because it did a better job of balancing the shot gathers and did not overly enhance unwanted noise at late times.

### Crooked Line 2D Geometry

Multichannel seismic reflection data acquisition over the Nechako Basin was done along the available logging roads and highways in the region. Since these roads were very crooked and involved significant variations in elevation, setting up the geometry for such a complicated survey is of the utmost importance. While the geometry information used for the original processing was available, the geometry for all the reprocessed lines was rebuilt to ensure quality control and consistency with the requirements of the Globe Claritas seismic processing software.

Using the Field Record Number (FFID) values in the trace headers along with the survey positions and elevations in the SEGP1 formatted observer files, the geometry for each line was reconstructed and verified using the geometry QC tools available within Globe Claritas. The geometry parameters for the four reprocessed lines are presented in Table 1.

<b>Table 1: Geometry parameters</b>				
	<b>2008-05</b>	<b>2008-10</b>	<b>2008-12</b>	<b>2008-13</b>
<b># traces</b>	1017600	1898880	859200	2071680
<b># receivers</b>	3178	5941	2980	6495
<b># vibe points</b>	1060	1978	4579	2158
<b>max traces/vibe point</b>	960	960	960	960
<b># hitpoints for crooked line</b>	20	40	40	40
<b>receiver spacing</b>	20 m	20 m	20 m	20 m
<b>vibe point spacing</b>	40 m	40 m	40 m	40 m
<b>nominal CMP spacing</b>	10 m	10 m	10 m	10 m
<b>CMP bin half-width perpendicular to line</b>	2500 m	2300 m	2000 m	2000 m
<b># of CMPs</b>	3664	7052	3667	7485
<b>max CMP fold</b>	346	517	320	541
<b>average CMP fold</b>	270	270	230	270
<b>vibe sweep</b>	28 s, 8-64 Hz			
<b>uncorrelated trace length</b>	34000 ms	34000 ms	34000 ms	34000 ms
<b>correlated trace length</b>	17998 ms	17998 ms	17998 ms	17998 ms
<b>sampling rate</b>	2 ms	2 ms	2 ms	2 ms

To map the seismic traces from the shots gathers to the common midpoint (CMP) gathers needed for subsequent stacking, a binning geometry must be defined for each line. Given the crookedness of the acquisition lines, the CMP binning was achieved by defining hit points through which the CMP bin centre line would track for each seismic line. Figures 25 through 28 display maps of the geometry setup for each line.

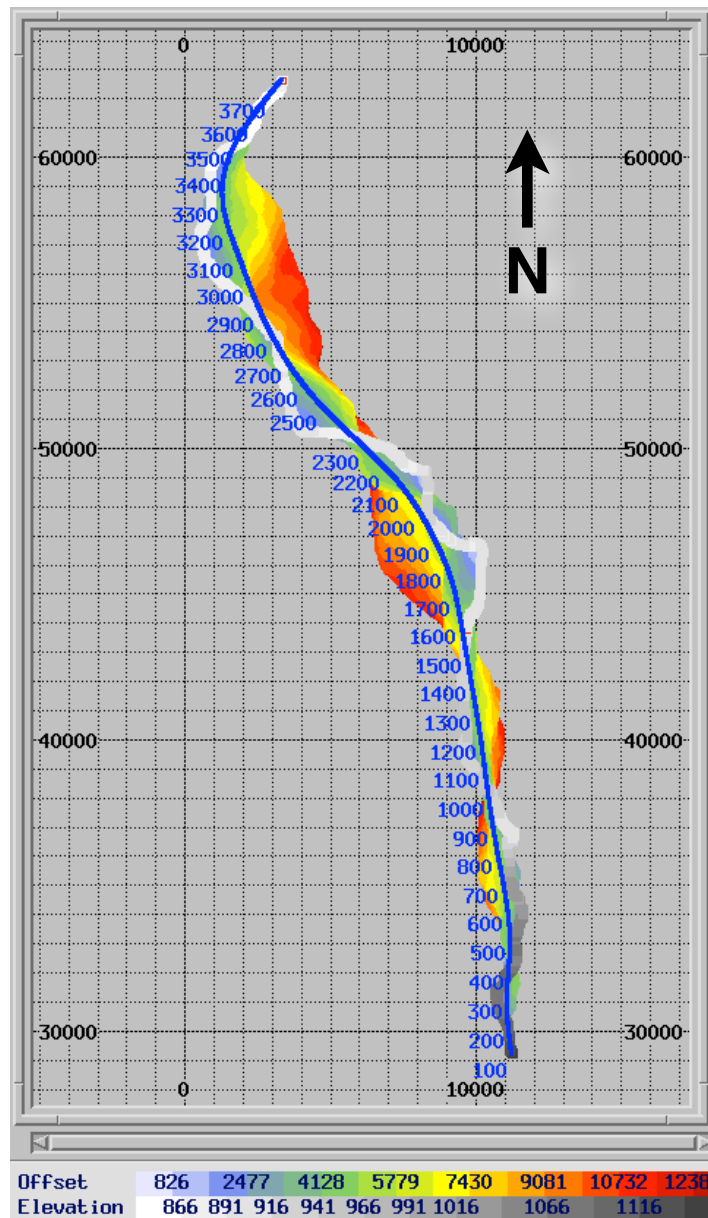


**Figure 25:** Map of Line 2008-05 geometry with the acquisition line (coloured by grayscale elevation), the CMP bin centre line (blue line with CMP labels) and the shot-receiver midpoint locations (coloured by offset). Grid squares are 1 km by 1 km.

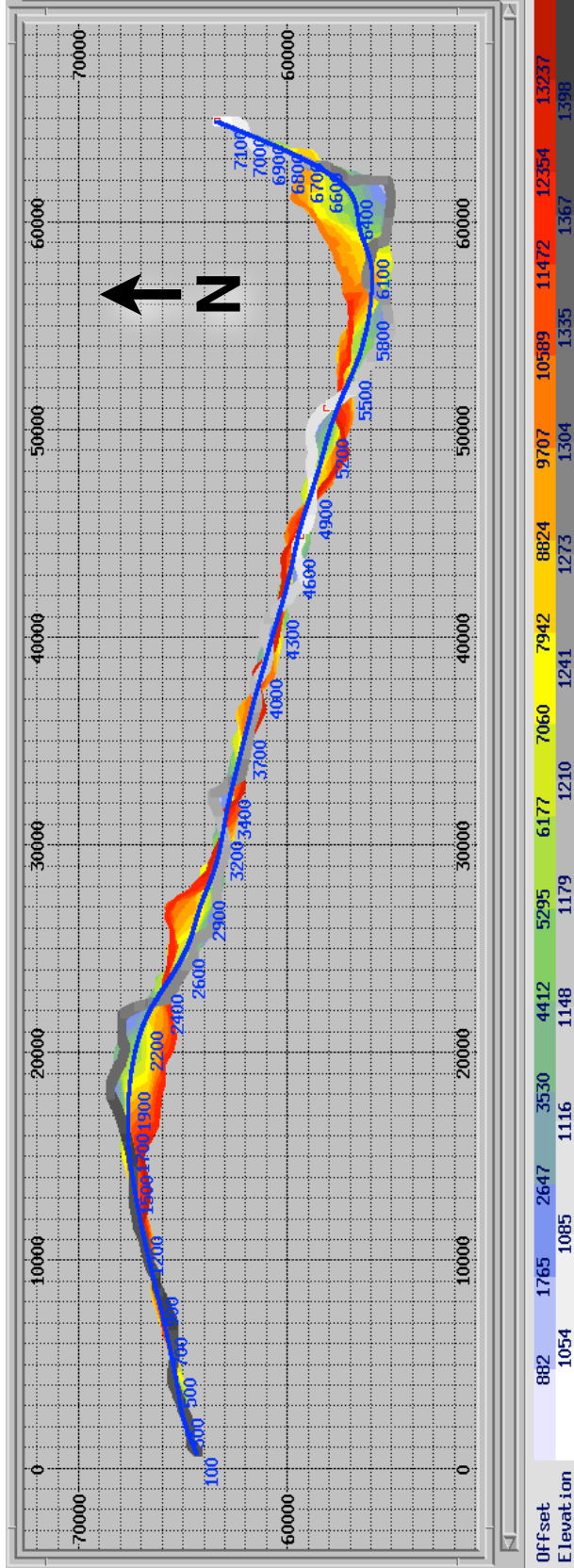


**Figure 26:** Map of Line 2008-10 geometry with the acquisition line (coloured by grayscale elevation), the CMP bin centre line (blue line with CMP labels) and the shot-receiver midpoint locations (coloured by offset). Grid squares are 1 km by 1 km.

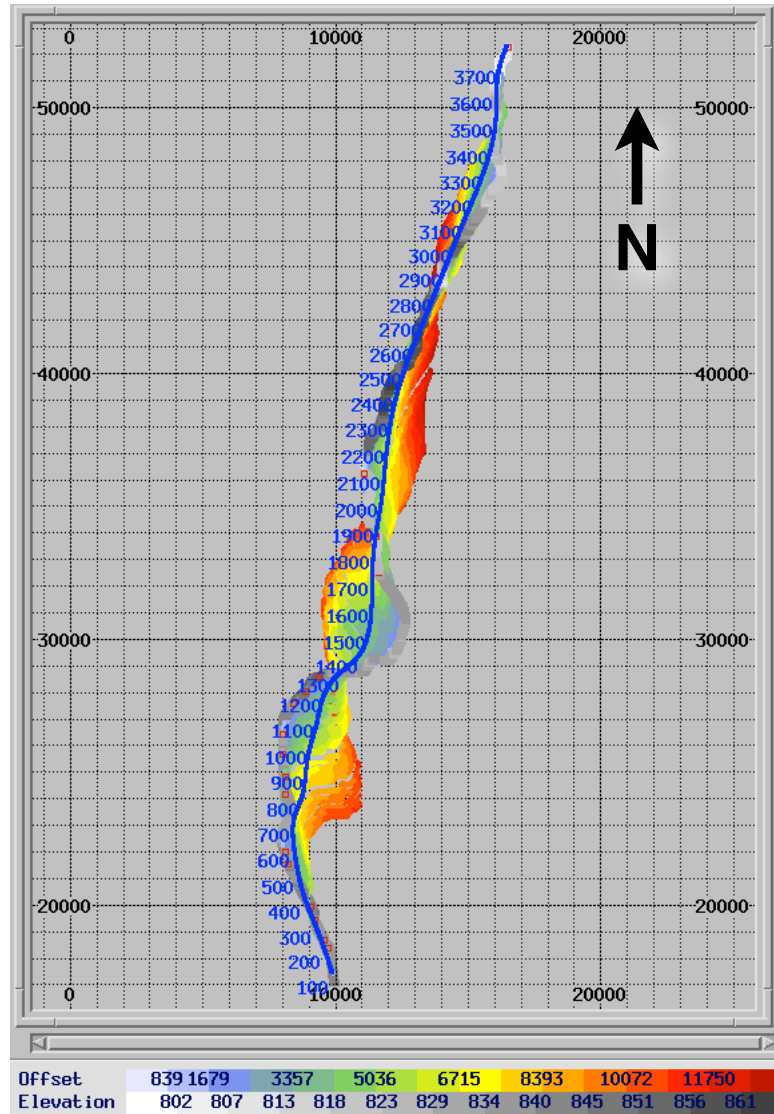


**Figure 27:** Map of Line 2008-12 geometry with the acquisition line (coloured by grayscale elevation), the CMP bin centre line (blue line with CMP labels) and the shot-receiver midpoint locations (coloured by offset). Grid squares are 1 km by 1 km.

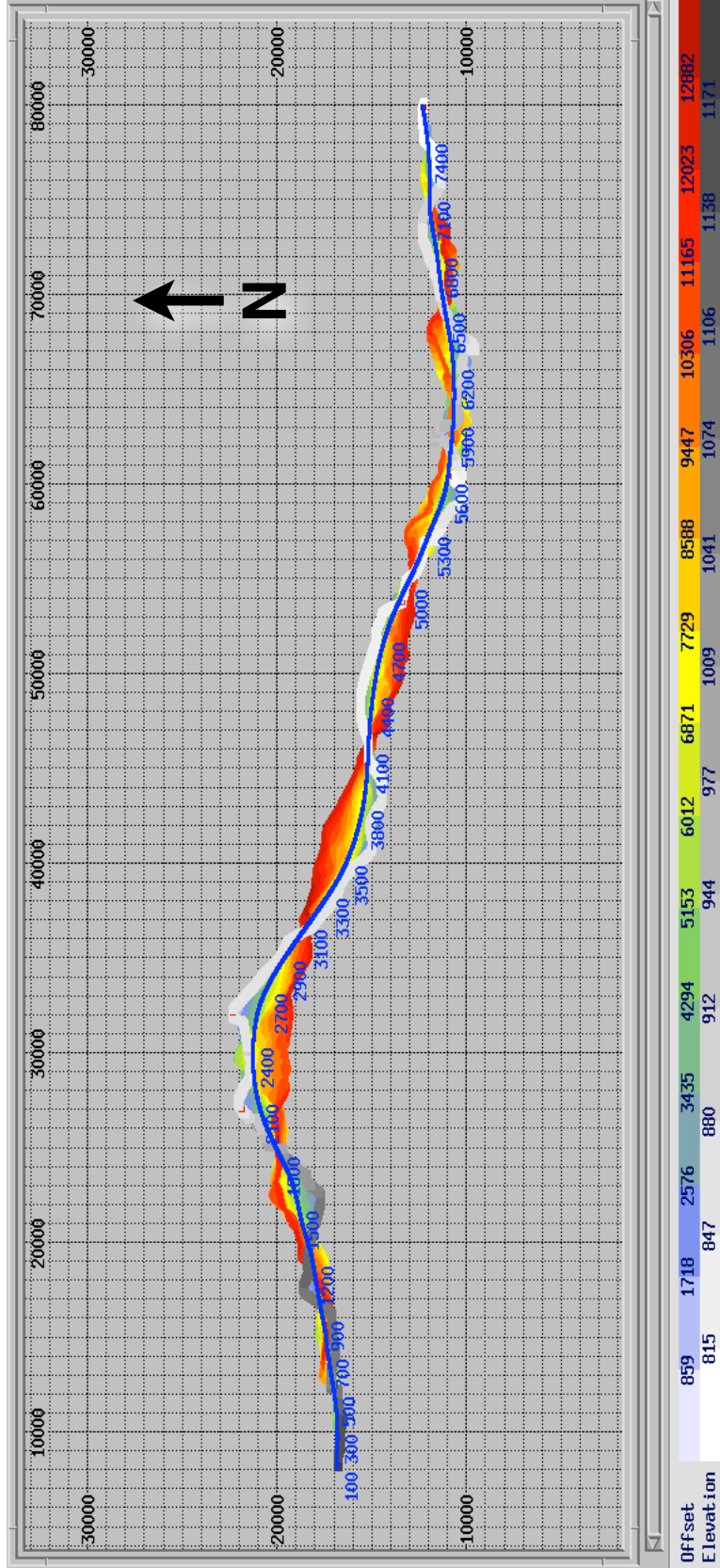


**Figure 28:** Map of Line 2008-13 geometry with the acquisition line (coloured by grayscale elevation), the CMP bin centre line (blue line with CMP labels) and the shot-receiver midpoint locations (coloured by offset). Grid squares are 1 km by 1 km.

## **Frequency Filtering**

Two zero-phase filters with quasi-trapezoidal amplitude spectra were applied to the shot gathers. The first filter applied was a high pass filter (10-20 Hz) designed to remove long wavelength noise in the data. The second filter applied was a notch filter (57-58-64-70 Hz) to remove powerline noise.

## **Surface Consistent Deconvolution**

Note that deconvolution was not applied for the reprocessing of the Nechako data undertaken for this report. This choice was made for two reasons. First, the tests done to determine the optimal deconvolution parameters revealed only marginal improvements in the sharpening of the wavelet while also introducing significant high frequency noise (likely due to the violation of the minimum phase assumption with the zero phase Ricker wavelet resulting from the initial correlations). Second, since the goals of the reprocessing were to try to pull out as many coherent reflectors at depth in the complex subsurface, it was felt that broader seismic wavelets might result in better chances for constructive stacking, even in the presence of residual static problems.

## **Near Surface Statics**

For the original processing of the Nechako seismic data, CGG Veritas undertook a two step approach to computing refraction statics to account for variability in the near-surface weathered layer. Following first break picking which was undertaken out to 3000 m of offset, a generalized linear inversion (GLI) approach was used to construct a two-layer initial model. This model was subsequently refined using a tomographic turning ray approach.

The refraction statics solution available within Globe Claritas is a stratified ray tracing approach, more akin to CGG Veritas' initial GLI approach. These layer-based approaches generally do a poorer job of characterizing complex velocity variations

compared with tomographic methods. Nonetheless, it was hoped that comparable static solutions could be obtained for the Nechako Basin data by using first break picks to greater offsets and by exploiting the ability to increase the complexity of the Globe Claritas near-surface model with additional layers and model nodes. Unfortunately, all attempts to improve upon the static solutions obtained by CGG Veritas proved unsuccessful and the refraction static corrections from the original processing (long wavelength and surface consistent short wavelength) were ultimately used for this reprocessing. These were extracted directly from the data headers and no datum corrections were applied beyond those performed by CGG Veritas.

It is hoped that the first break arrivals picked for this reprocessing study (which extended and often adjusted the original automatic CGG Veritas picks out to the full shot offsets) can ultimately be used to develop deeper tomographic models for the four reprocessed lines in the future.

### **Velocity Analysis and Normal Moveout (NMO)**

Once static corrections have been applied to the data, the accuracy and quality of the subsequent velocity analysis is key to generating an interpretable section from the CMP gathers. To this end, careful velocity analysis was performed for every 100th CMP along the four reprocessed lines using a combination of semblance, constant velocity gathers and constant velocity stacks. A second pass at velocity analysis was then performed focusing specifically on the shallowest arrivals where data fold is limited. The CMP gathers were then corrected for Normal Moveout (NMO) using a stretch mute of 15% with a 50 ms taper. This relatively harsh stretch mute ensured that the wide bins used for stacking did not adversely affect the shallow stacked seismic section through the incorporation of shallow noise or poorly aligned arrivals from far offset traces. No cross-dip corrections were applied prior to stack.

## **Residual Statics**

Prior to stack, remaining time shifts within the CMP gathers can be corrected by computing residual statics. For this study, two methods of computing residual statics were tested. The first, stack-power surface-consistent residual statics, which involves first cross-correlating the shot gathers and then the receiver gathers against the best available stack, determines the necessary surface consistent static corrections required to maximize the stack power (Ronen and Claerbout, 1985). The second, a CMP-aligned, non surface-consistent static correction, simply adjusts the static shifts for each trace within a CMP gather by cross-correlating each trace with a pilot trace formed from the NMO-corrected stack of part or the whole of the CMP gather.

Neither of the tested methods provided significant improvements to the stack for early iterations and both led to poorer stacks with increasing iterations as the cumulative static corrections diverged and caused more jittery gathers. The failure of these algorithms is not likely due to any intrinsic flaws in their design but rather due to the sheer complexity of the subsurface geology to be imaged. Within classic sedimentary basins where laterally coherent reflections are the norm, the resulting static calculations from both methods would likely have their intended effect and improve the stack. However, for the Nechako Basin dataset where there is a lack of significant coherent reflectivity against which to focus the stack improvements, it seems that the algorithms failed to converge for the targets of interest and found improved stacks through the stacking of noise. Consequently, it was decided that no residual statics, other than the original long and short wavelength refraction statics from the original CGG Veritas processing, would be used in the reprocessing.

## **Stack**

Following the application of a 500 ms Automatic Gain (AGC), the NMO-corrected CMP gathers were stacked with a square root normalization. The resulting stacks were then compared with the original stacked results from CGG Veritas. The whole velocity analysis-NMO-stack process was then repeated to generate as clear a stack as possible for each of the lines. The final stacks are compared with the original stacks from the CGG Veritas processing in Figures A-1, A-2, A-3 and A-4 (these same sections with underlain interpretations are presented in Figs. A-5, A-6, A-7, and A-8). The stack comparisons show similar reflectivity patterns from the two processing approaches.

## **Migration**

For the original processing of the Nechako seismic reflection data, CGG Veritas applied a post-stack phase shift time migration using the stacking velocities scaled by 85%. Since the equivalent phase shift migration algorithm in Globe Claritas only allows for vertically varying velocities, two alternate migration routines that allowed for laterally variable velocities were used, namely finite-difference time migration and Kirchhoff time migration. The finite-difference migration algorithm required interval velocities so the stacking velocities were first smoothed horizontally and then converted to interval velocities using the Dix equation. These velocities were further scaled by 85%. As the Kirchhoff time migration required stacking velocities, these were simply smoothed horizontally and then scaled by 85%. The two migration approaches used in this study are compared with the migration results from the CGG Veritas processing in Figures A-9, A-10, A-11, and A-12 (these same sections with underlain interpretations are presented in Figs. A-13, A-14, A-15, and A-16).

Overall, whether for the original processing from CGG Veritas or for the reprocessing from this study, migrating the stacked sections did not help generate significantly more interpretable sections. In fact, steepened dips and moderately collapsed diffractions aside, interpreting the stacked sections is arguably easier than doing so on the migrated sections.

## **Coherency Filtering**

In order to further enhance as much coherent seismic reflectivity as possible from the seismic sections, all the reprocessed data sections presented herein were subjected to a coherency filter prior to plotting. Note that the coherency filter was not applied to the results from the original CGG Veritas processing.

The post-stack coherency filter used for this study is a variant of a spatial linear signal detector which seeks out linear features over a prescribed number of traces. By applying the filter laterally using a sliding window, the entire seismic section can be filtered. This coherency filter, originally adapted from Milkereit and Spencer (1989) and used extensively by the Lithoprobe project, was designed to help highlight reflectivity from deep crustal seismic data where background noise can be significant. Given the lack of regionally extensive stratigraphy and the complex subsurface geology of the Nechako Basin, this coherency filter is ideal for the Geoscience BC dataset.

The coherency filter is computed and applied in the tau-p domain. For all the reprocessed seismic sections (both stacked and migrated), the sliding window was 50 traces wide and dips were limited to a maximum slowness of 0.5 ms/m across 101 slowness traces in the tau-p domain. As an extra feature in Globe Claritas, 50% of the original seismic data was added back to the coherency filtered output to maintain its seismic appearance.

## Interpretation of the Reprocessed Sections

Due to the limited view provided by the sparse wells, the complexity and heterogeneous nature of the near-surface geology and the lack of significant coherent reflectivity in the Nechako Basin, interpreting the original and reprocessed seismic sections is difficult, and generally beyond the scope of this reprocessing project. Nonetheless, boundaries interpreted from 2-D magnetotelluric models (Spratt and Craven, 2011), extrapolations from wells, and earlier seismic interpretations (Calvert et al., 2011) are useful for gauging the success of the reprocessing and assessing whether improvements over the original processing have been made. The final stacked and migrated sections from the original processing and the reprocessing from this study are plotted with available interpretations in Figures A-5, A-6, A-7, A-8, A-13, A-14, A-15, and A-16.

Of the four reprocessed lines, Line 2008-5 (Figs. A-5 and A-13) has been interpreted to the greatest extent (Calvert et al., 2011), aided significantly by its close proximity to well a-7-L. For both the original processed section and the reprocessed section, the interpreted horizons at the southern end of the line from Calvert et al. (2011) can be easily located and correlated with imaged coherent reflections. At the northern end of the line, there is significantly less reflectivity and the base of the sedimentary units interpreted by Spratt and Craven (2011) and shown by the dashed orange line, does match up with several coherent reflectors and marks a subtle but abrupt decrease in reflectivity with depth. However, the southernmost extent of the base of sediments interpreted by Spratt and Craven (2011) does not show any correlation with the imaged stratigraphy beneath the Cretaceous sedimentary cover.

Line 2008-12 extends northward from Line 2008-5 and provides the poorest shallow section of all the lines considered. Apart from the base of the Cretaceous sediments interpreted from Calvert et al. (2011), shallow reflectivity is poor and there are few coherent reflections from which any interpretation can be extracted. Nonetheless, the

inferred Cretaceous sediments are arguably imaged more clearly on the reprocessed section than on the original section, albeit with lower frequency content.

Line 2008-10 shows the best correspondence between the MT-derived interpretations and the imaged seismic reflectivity. The base of the sedimentary units interpreted by Spratt and Craven (2011) and shown by the dashed orange lines in Figures A-7 and A-15 does generally follow variations in the shallow reflectivity and all the interpreted faults correspond with imaged faults on the seismic section. At the eastern limit of the profile, both the original section and the reprocessed section show evidence for parallel westward dipping reflectors that may extend to greater depth. Unfortunately, the surface outcrop of whatever structure they delimit is overlain by Quaternary sediments.

Reprocessing enhanced the overall reflectivity observed for Line 2008-13 (Figs. A-8 and A-16) with a gradual decrease in reflectivity observed from the west to the east. Shallow faults of varying dip are imaged within the shallowest part of the section along the entire line and a greater number of deeper coherent reflections, of unknown origin, are observed, particularly in the west. However, imaging of a potential, faulted, sub-basin in the centre of the line beneath the Chilcotin Group volcanics (Calvert et al., 2011) was not improved significantly by the reprocessing, despite a careful examination of CMP gathers and their stacks in the vicinity of the inferred basin, and the existence and extent of the inferred sub-basin remains uncertain.

Coherency-filtered final stacks from the four multichannel seismic reflection lines are plotted down to their full extended correlation length of 18 s two-way-time (TWT) in Figures A-17 to A-20. As previously observed by Calvert et al. (2011), the base of the crust or Moho along all the lines appears to correspond with a decrease in reflectivity at 11.5 s TWT, consistent with the base of the crust at 35 to 38 km depth. Lateral amplitude changes are observed where there are larger changes in the orientation of the seismic lines.

## **Assessing Contribution of MT Results to Reprocessing of Vibroseis Data**

It was proposed to use the models derived from the MT data to guide reprocessing of Vibroseis data collected by Geoscience BC in 2008 with the aim of improving the results of the seismic data effected by scattering off and within the overlying Eocene volcanoclastics. With the guidance of Jim Craven the conductivities of the 2-D MT-derived models were transformed to seismic velocities using relationships determined from the seismic velocities and conductivities measured in samples of the major rock units in the Nechako region.

### **Physical Property Measurements and Well Logs**

Geophysical laboratory measurements on rock samples from three key units of the Nechako Basin (the Eocene volcanic units, the Jurassic to Cretaceous sedimentary units and the older basement and Mesozoic rocks) reveal a poorly constrained and scattered relationship between the physical properties of interest to this study, namely electrical resistivity and P-wave seismic velocity (Andrews et al., 2011; Fig. 7). From these and an independent study of available well logs (Mwenifumbo and Mwenifumbo,

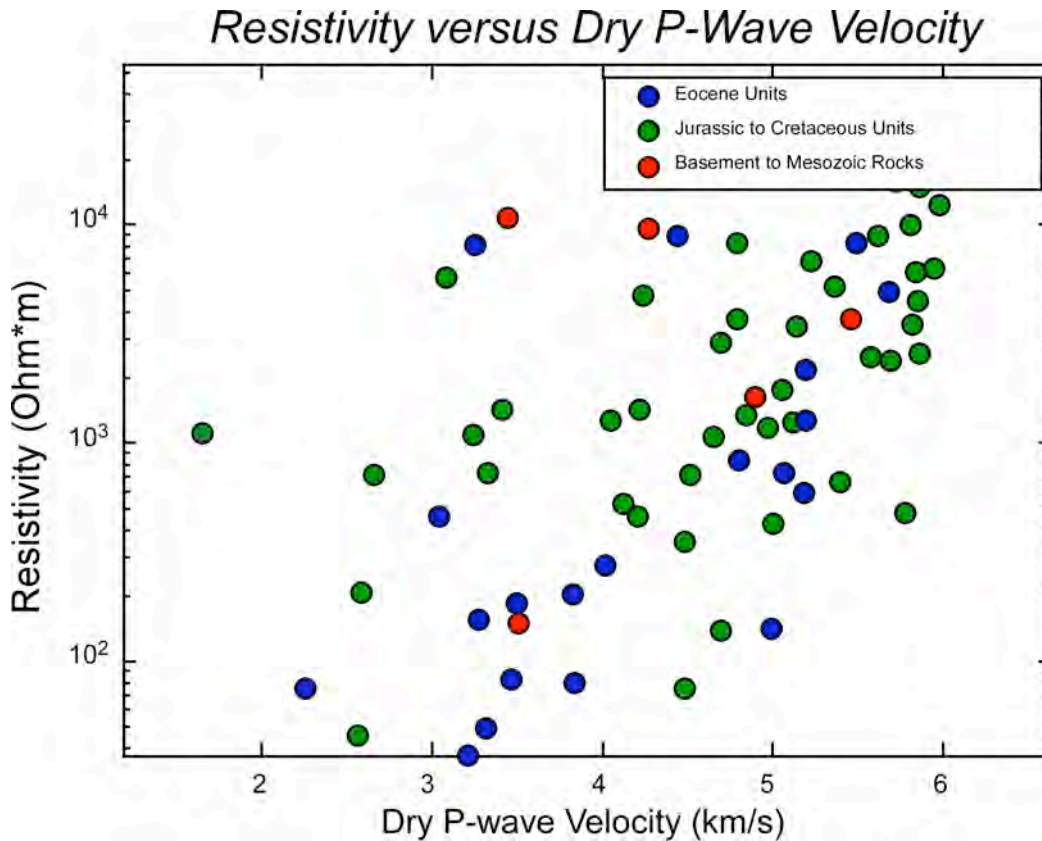


**Figure 29:** Plot of dry P-wave velocity (km/s) versus resistivity (Ohm\*m) measured from representative rock samples from the main lithologies of the Nechako Basin.

2010), three simple empirical relationships were derived.

The first applies to the entire stratigraphic column (Mwenifumbo and Mwenifumbo, 2010):

$$\text{velocity (km/s)} = 2.375 + 1.39 \cdot \log_{10}(\text{resistivity (Ohm*m)}).$$

The second applies to shales and sandstones, the potential reservoir rocks (Mwenifumbo and Mwenifumbo, 2010):

$$\text{velocity (km/s)} = 1.915 + \log_{10}(\text{resistivity (Ohm*m)})$$

and the third, taken from Richard Kellett's presentation at the Nechako workshop January 2010, applies to the shallow top few hundred meters, where there is

predominantly Chilcotin and Eocene volcanic units:

$$\text{velocity (km/s)} = 1.077 + 1.010 \cdot \log_{10}(\text{resistivity (Ohm}\cdot\text{m)}).$$

While these empirical relationships can be derived from the data, it is clear from Figure 29 that the relationship between P-wave velocity and resistivity in the Nechako Basin is complicated for all lithologies and that the equations used in this study to convert from resistivity to P-wave velocity are highly non-unique.

## **Resistivity to Velocity Conversion**

Using the empirical relationships between resistivity and P-wave velocity derived from the well logs and physical property measurements of the key Nechako Basin units, three velocity models were constructed from the resistivity models for lines 2008-5 and 2008-10. Model A is appropriate for the entire stratigraphic column, Model B is appropriate for reservoir rocks (shales and sandstones) and Model C is appropriate for the shallow volcanic units. The original resistivity model (with interpretation from Spratt and Craven, 2011) and the three velocity models for Line 2008-5 are shown in Figure 30. The equivalent models for Line 2008-10 are shown in Figure 31.

Attempts were made to further classify the resistivity values of the 2-D MT models with known rock types in the region, and thereby further define the locations of various units in the models. The location of interfaces between the units could then be used to help guide the seismic reprocessing. Histograms were generated for the data beneath profile A by plotting the number of occurrences of specific ranges of resistivities (Figure 32). The intent was to try to find a relationship between the histograms and the resistivities measured in samples, but this was not completed. Another attempt to assign specific rock types to specific resistivity values in the MT models was done by comparing 1-D models of MT sites to 1-D models generated from synthetic MT response curves calculated from the resistivity measured in nearby borehole logs (Figure 33). Although

there are strong similarities between the 1-D models from the well logs and those from the MT sites, the differences were large enough to prevent a direct comparison with the borehole resistivity logs and the stratigraphic columns. This is likely due to the complex subsurface structure specifically within the Cretaceous sedimentary units where there are strong lateral variations over short distances.

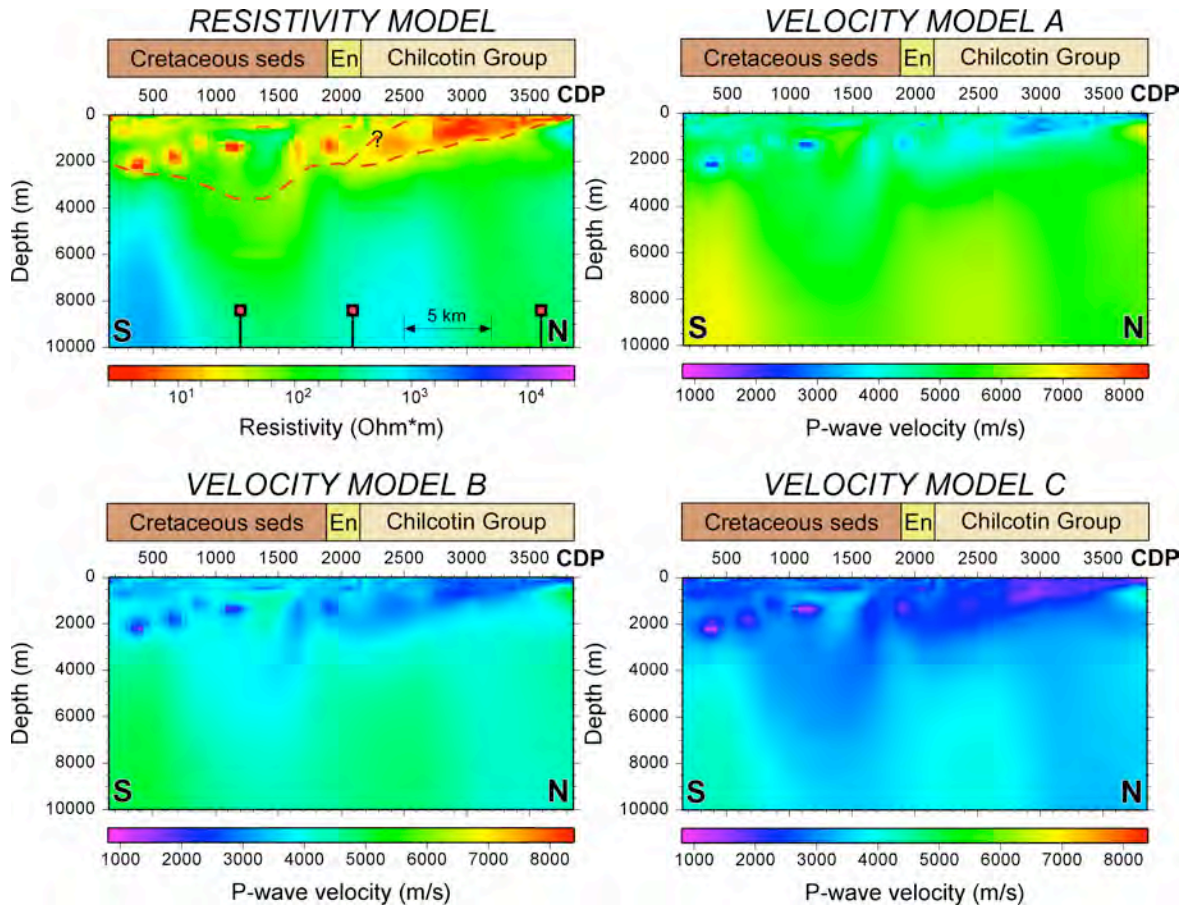


**Figure 30:** Resistivity model for Line 2008-5 derived from MT studies (top left) and P-wave velocity models derived from the resistivity model using three lithology-specific empirical relationships (A - top right, B - bottom left, C - bottom right). The dashed orange line on the resistivity model plot is the base of the Nechako sedimentary units interpreted by Spratt and Craven (2011). The red squares along the bottom of the same plot show the locations of the velocity comparisons in Figure 34.

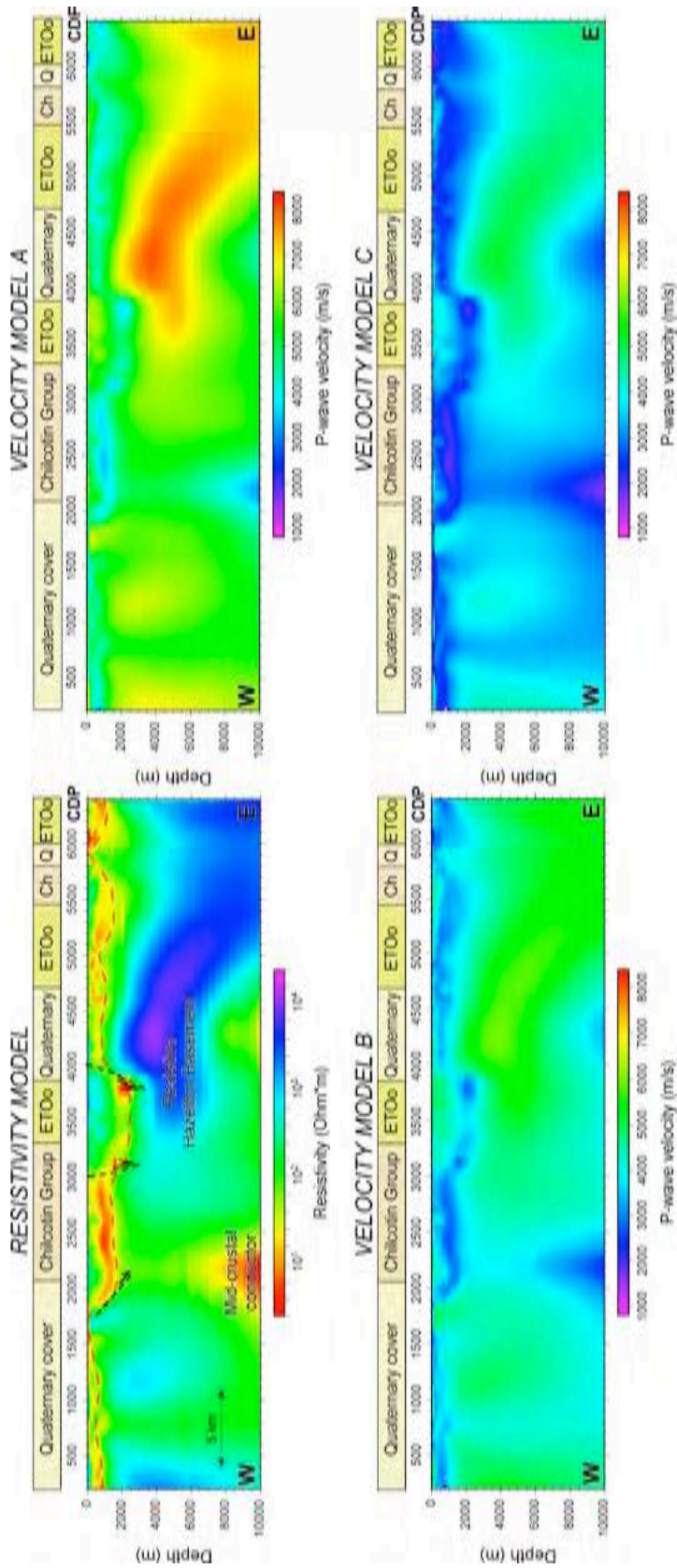


**Figure 31:** Resistivity model for Line 2008-10 derived from MT studies (top left) and P-wave velocity models derived from the resistivity model using three lithology-specific empirical relationships (A - top right, B - bottom left, C - bottom right). The dashed orange line on the resistivity model plot is the base of the Nechako sedimentary units interpreted by Spratt and Craven (2011). The dashed black faults are also from the interpretation by Spratt and Craven (2011).

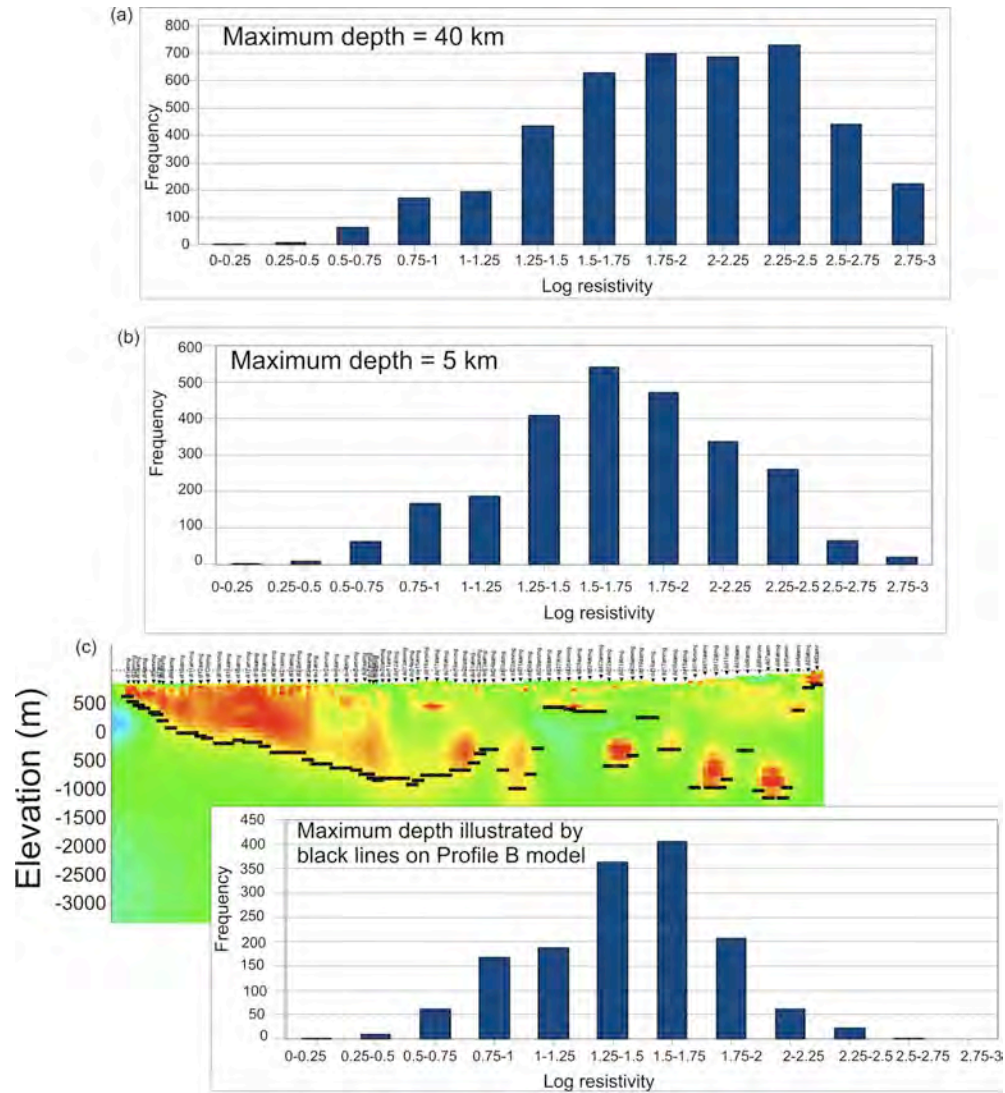


**Figure 32:** Histograms of the occurrence of resistivity values in the 2-D model along profile B. (a) shows the results to a depth of 40 km, (b) shows the results to a depth of 5 km, and (c) shows the results to the base of the high conductivity layer observed along the profile.

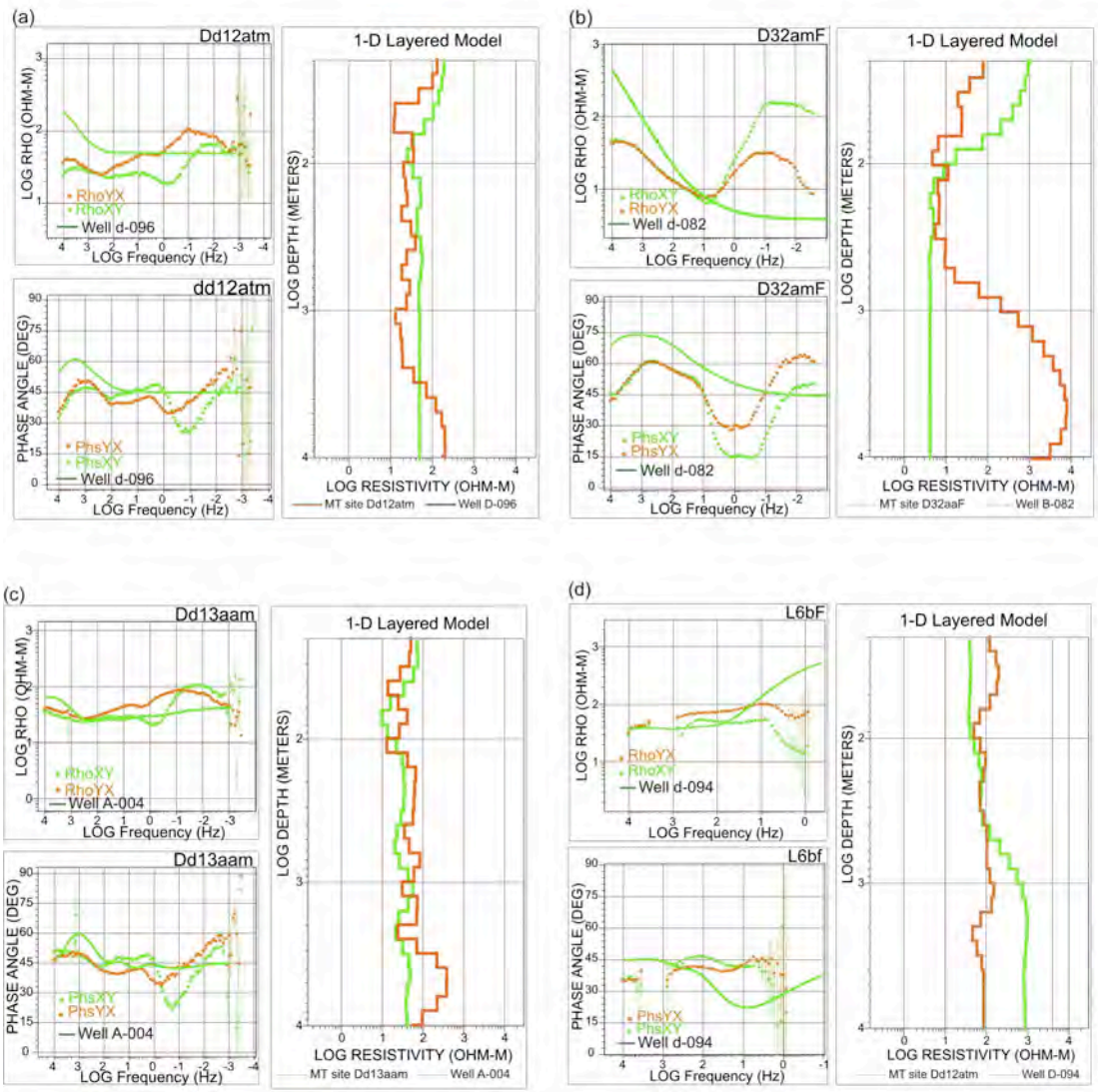


**Figure 33:** Comparison of the results of 1-D models calculated from MT site locations and those generated from synthetic response curves derived from the resistivity borehole logs. (a) shows a comparison between well d-096 and site dd12atm located at the south end of profile B, (b) shows a comparison between well b-082 and site d32amf located at the west end of profile G, (c) shows a comparison between well A-004 and site dd13aam located at the south end of profile B, and (d) shows a comparison between well D-094 and site L6bf located a the southwest end of profile F.

## Building the Optimal Velocity Model

To gauge how appropriate the empirically-derived velocities were for Line 2008-5, the velocities in Figure 30 were compared against stacking velocities (converted to interval velocities using the Dix equation) derived from reprocessing of the seismic data alone. Comparisons from three specific CDP locations (shown as red squares on the resistivity model in Fig. 30) are shown in Figure 34.

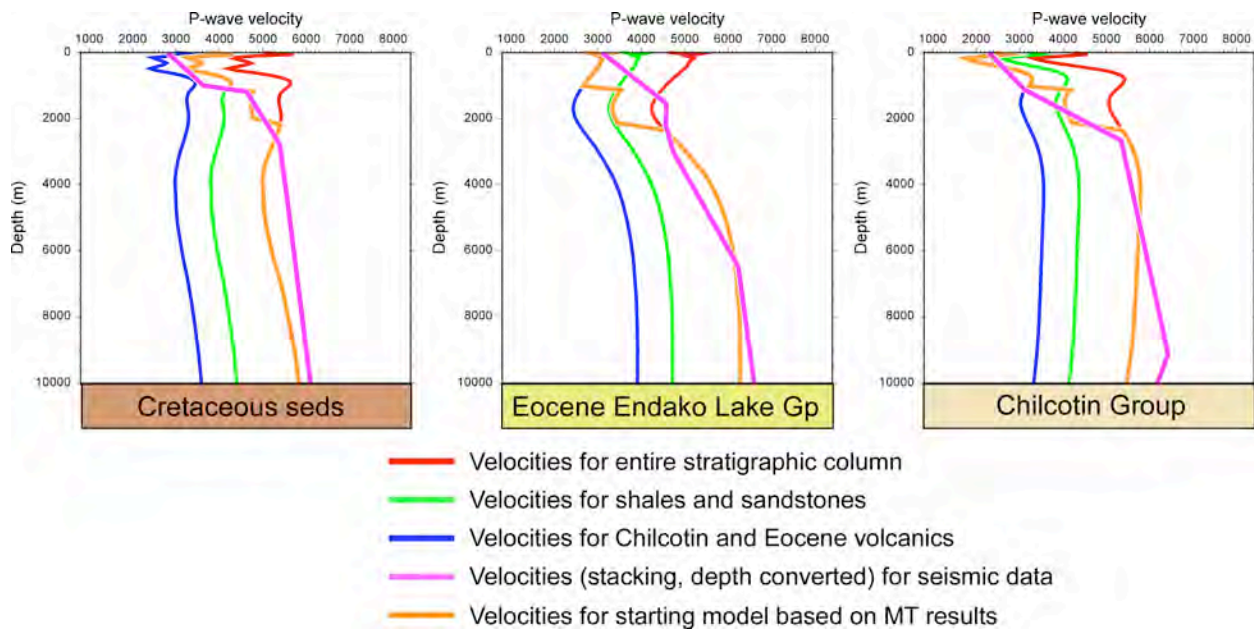


**Figure 34:** Comparison between the stacking velocities (converted to interval velocities using the Dix equation) and the empirically-derived velocities from the resistivity model at three specific CMP locations (shown in Fig. 30).

Based on these comparisons, the optimal starting velocity model was constructed using lithology-appropriate MT-derived velocities for the top 1 km, MT-derived velocities for the entire stratigraphic column below 2 km and an average of the two between 1 and 2 km. The resulting models for Line 2008-5 and for Line 2008-10 are shown in Figures 35 and 36, respectively.

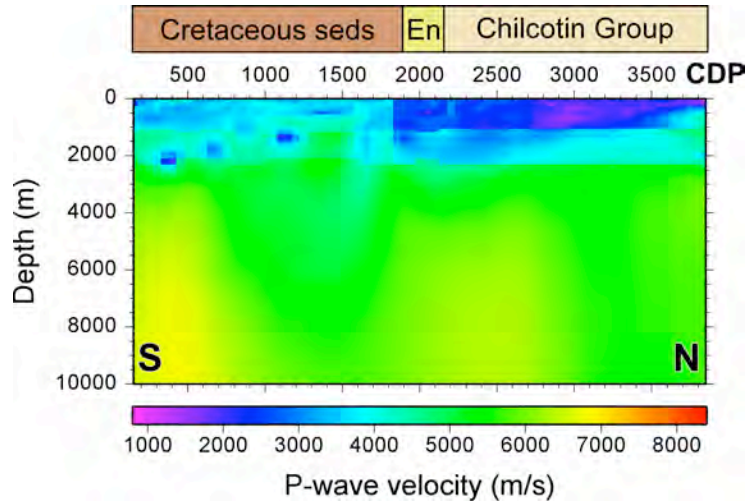


**Figure 35:** Optimal velocity model for Line 2008-5 based on lithology-specific application of velocities empirically-derived from the resistivity model.

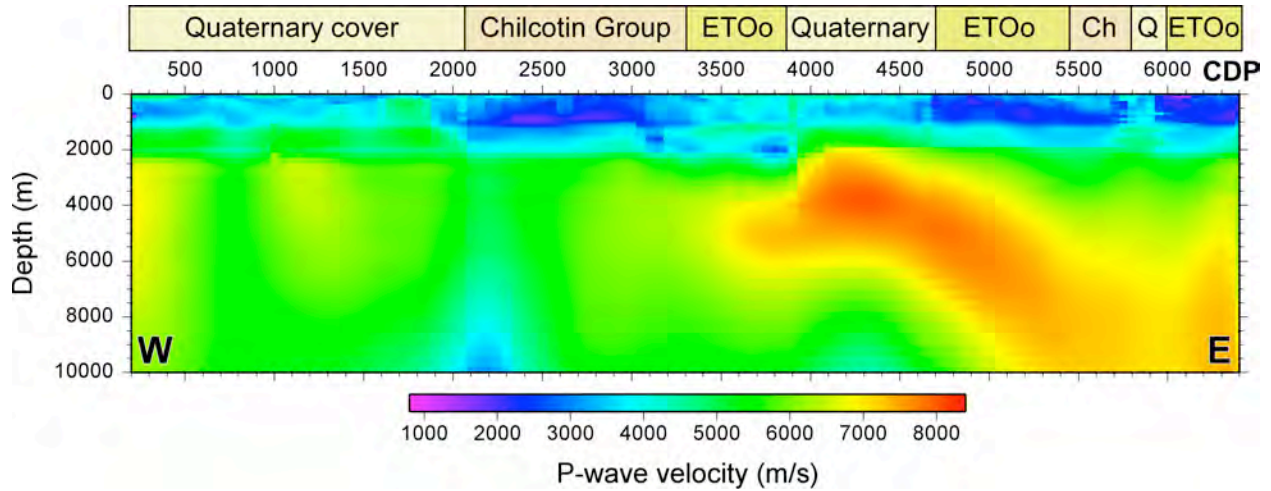


**Figure 36:** Optimal velocity model for Line 2008-10 based on lithology-specific application of velocities empirically-derived from the resistivity model.

## Stack Comparison

A comparison of the stacked results using only the MT-derived optimal velocity models (converted to RMS velocity) and the best stacked results obtained from the seismic data show that, as a first approximation, the MT-derived velocities do an adequate job of capturing many of the key reflections (Figs. A-21, A-22). They do, however, do a poor

job in the shallowest part of the section where detailed velocity analysis is essential. As such, an educated guess at stacking velocities would likely have produced similar results.

## Joint Interpretation

The best stacks for both lines were depth-converted using highly smoothed versions of their stacking velocities converted to interval velocities (using the Dix equation). These depth-converted sections were overlain on the resistivity models to look for similar structures to those interpreted by Spratt and Craven (2011).

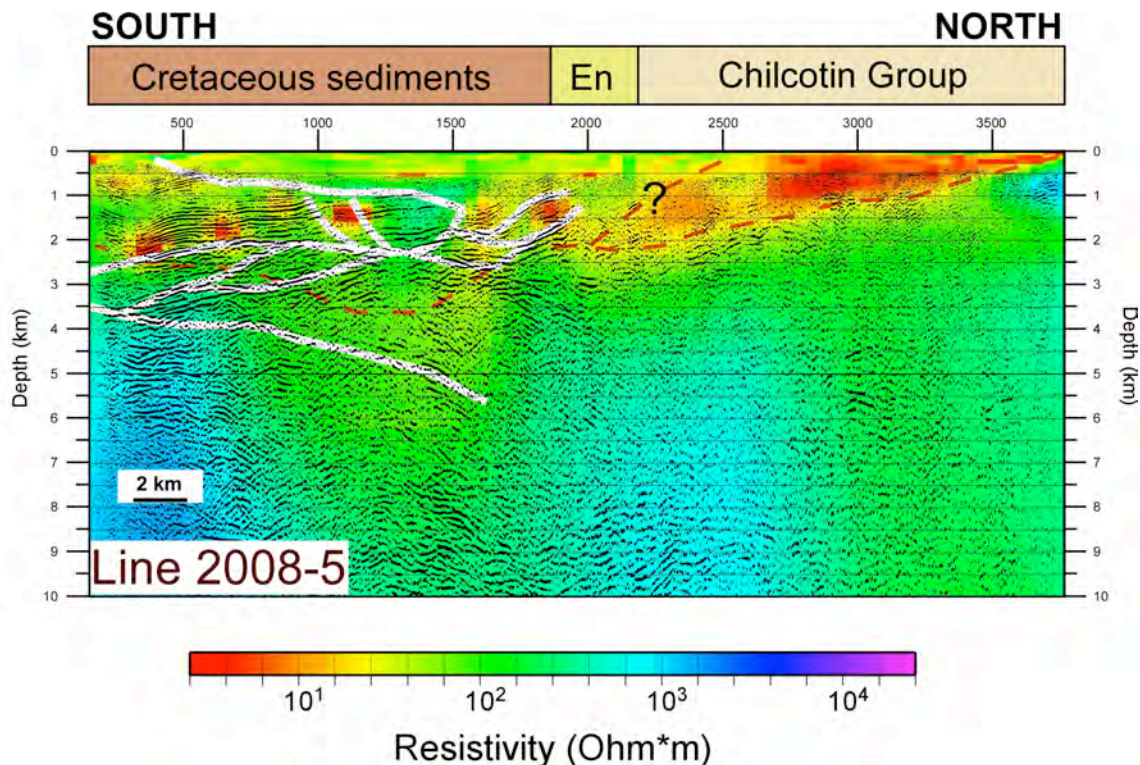


**Figure 37:** Depth-converted final stack for Line 208-5 overlain on the MT-derived resistivity model. The dashed orange lines show the base of the Nechako sedimentary units interpreted by Spratt and Craven (2011) while the white lines show the seismic interpretation from Calvert et al. (2011).

For Line 208-5 (Fig. 13), the match between the MT-interpreted structures with the more detailed seismic interpretation from Calvert et al. (2011; shown by white lines) shows significant disagreement beneath the Cretaceous sediments while a better match

is obtained beneath the Chilcotin Group volcanics. In fact, the upper bound of the conductive volcanics corresponds with a westward dipping reflector.

For Line 2008-10, there is generally a good correspondence between the faults and boundaries interpreted from the MT sections and those observed on the seismic sections (Fig. 14). The easternmost fault which is evident on the seismic section but was not interpreted on the original resistivity model appears to separate more highly conductive material to the east (Eocene Ootsa Lake Group volcanics) from more resistive Quaternary sediments to the west.

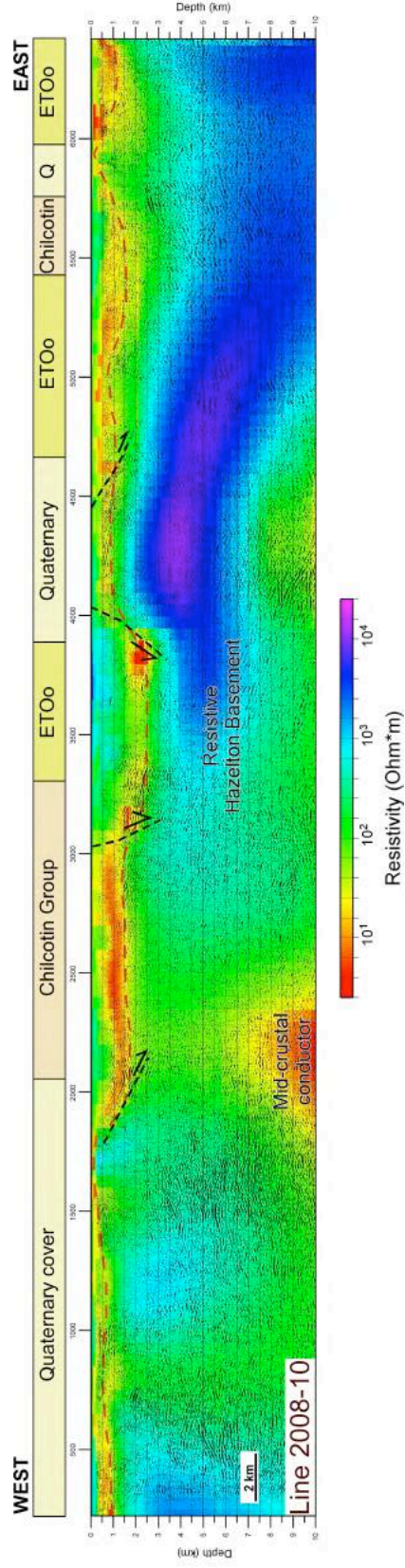


**Figure 38:** Depth-converted final stack for Line 2008-10 overlain on the MT-derived resistivity model. The dashed orange lines show the base of the Nechako sedimentary units interpreted by Spratt and Craven (2011). The easternmost dashed black fault was interpreted based on the seismic section and the resistivity model while the remaining faults are from the interpretation by Spratt and Craven (2011).

## **Key Findings from the Seismic Reprocessing**

- Reprocessing of key profiles from the Geoscience BC 2008 seismic survey generated comparable sections to the original processing by CGG Veritas with moderately more pronounced reflectivity along Lines 2008-5, 2008-10 and 2008-13.
- Reprocessing of the Geoscience BC 2008 data did not reveal any new reflective structures that were not already apparent to some extent in the original processed sections, indicating that the original processing was done well.
- To a first approximation, the MT-derived velocities based on well logs and physical property measurements in the Nechako Basin provided a surprisingly decent starting model for velocity analysis of the reprocessed lines. Although it must be stressed that the same information could have been obtained from the seismic data themselves, albeit in a more time-consuming manner.
- However, for the shallowest seismic data, the MT-derived velocities are consistently too high and must be lowered significantly during the velocity analysis to create an interpretable shallow section.
- Interpretation of the MT and seismic data together shows some good correspondence between structures, particularly for Line 2008-10, but limitations remain due to the differing resolutions and targeted physical properties of the two methods.

## Future Work

- First breaks were picked for all shot gathers out to the full offsets for Lines 2008-5, 2008-10 and 2008-13 for use in the computation of refraction statics. Ultimately, these did not provide as good a static correction solution as the original CGG Veritas refraction static solution due to differences in the software available to them to build the near-surface model and calculate the statics. Nonetheless, these picks could be useful for generating near surface velocity models for the three lines using alternate tomographic software, ideally in 3-D to better deal with the crooked acquisition lines. Recently developed software at MUN could be used for this task.

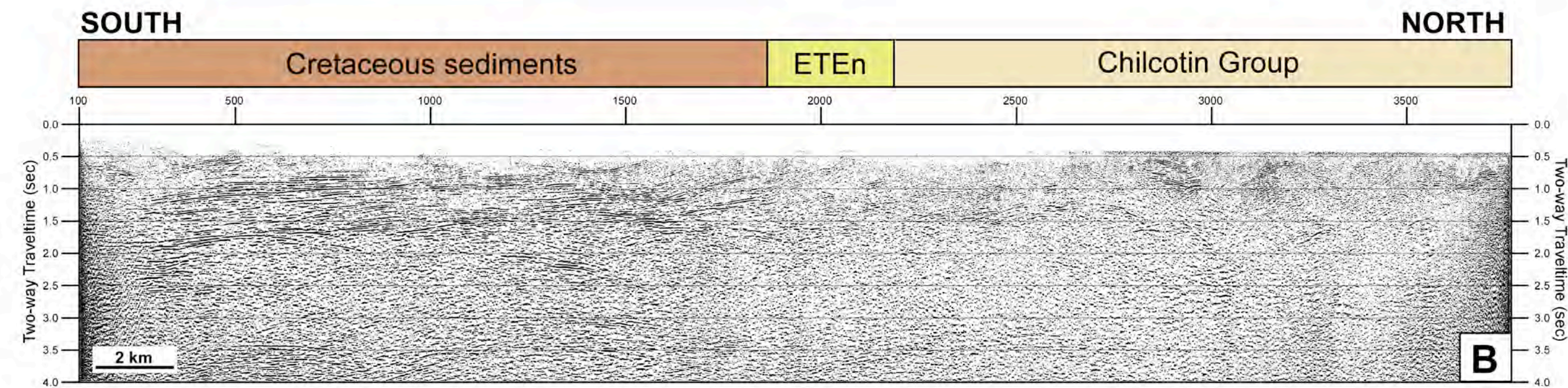
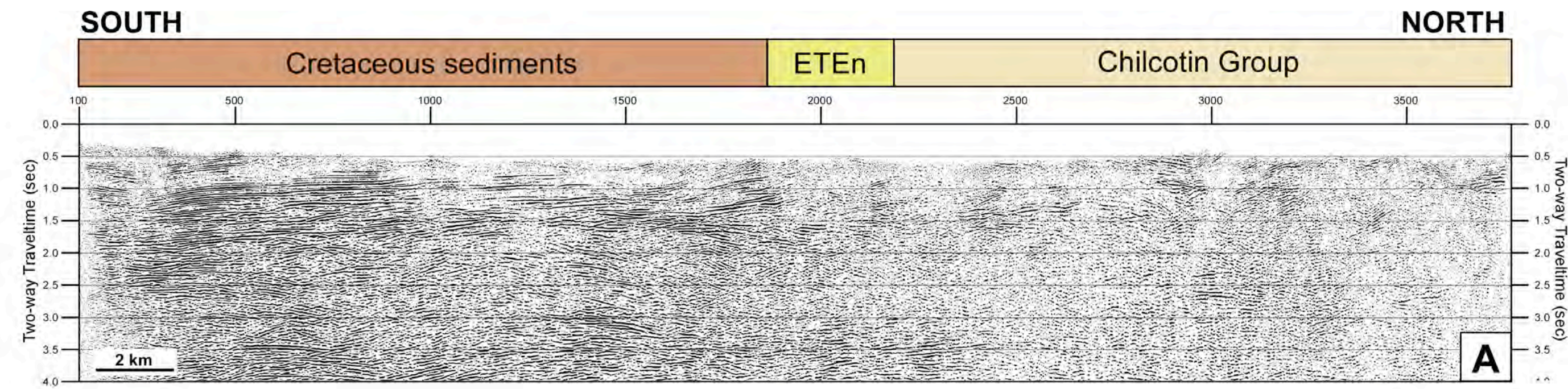
## References

- Andrews, G., Quane, S., Enkin, R.J., Russell, K., Kushnir, A., Kennedy, L., Hayward, N., and Heap, M., 2011. Rock physical property measurements to aid geophysical surveys in the Nechako Basin Oil and Gas Region, central British Columbia. Geoscience BC Report 2011-10, 40 pp.
- Calvert, A.J., Hayward, N., Spratt, J.E., and Craven, J.A., 2011. Seismic reflection constraints on upper crustal structures in the volcanic-covered central Nechako Basin, British Columbia. *Canadian Journal of Earth Sciences*, 48, 1021-1037.
- Geotech Limited (2009a): Helicopter-borne Z-Axis Tipper Electromagnetic (ZTEM) and Aeromagnetic Survey, Mt. Milligan Test Block; Geoscience BC, Report 2009-7, 51 p.
- Geotech Limited (2009b): Preliminary Report on ZTEM Airborne Geophysical Survey, Shea Creek Test Block, northwestern Saskatchewan, for AREVA Resources Canada Ltd., April-2009.
- Holtham, E. and Oldenburg, W. (2010): Three-dimensional inversion of ZTEM data; *Geophysical Journal International*, v.182, p. 168–192, doi:10.1111/j.1365-246X.2010.04634.x
- Lo, B., Legault, J., Kuzmin, P., and Combrinck, M., 2009. Z-TEM (airborne AFMAG) tests over unconformity uranium deposits, ASEG Extended Abstracts, 2009 , no. 1, 1-6.
- Milkereit, B., and Spencer, C., 1989. Noise suppression and coherency enhancement of seismic data. In *Statistical application in the Earth Sciences*, (eds) Agterberg, F.P., and Bonham-Carter, G.F., Geological Survey of Canada, paper 89-9, 243-248.
- Mwenifumbo, C.J., and Mwenifumbo, A.L., 2010. Analysis of well logs from the Nechako Basin. Geological Survey of Canada, Open File 6542, 36 pp.
- Riddell, J.M. (compiler), 2006. Geology of the southern Nechako Basin, NTS 92N, 92O, 93B, 93F, 93G. BC Ministry of Energy and Mines and Petroleum Resources, Petroleum Geology Map, 2006-1, 3 sheets, 1:400 000 scale.
- Ronen, J., and Claerbout, J., 1985. Surface-consistent residual statics estimation by stack-power maximization. *Geophysics*, 50, 2759-2767.

- Sattel, D., Witherly, K., Becken, M. (2010): A brief analysis of ZTEM data from the Forrestanian test site, WA. ASEG Extended Abstracts, September, v. 2010 (1), p. 1 – 4.
- Spratt, J.E., and Craven, J.A. (2009): Preliminary images of the conductivity structure of the Nechako Basin, south-central British Columbia (NTS 092N, O, 093B, C, F,G) from magnetotelluric methods. *In* Geoscience BC Summary of Activities 2008, Geoscience BC, Report 2009-1.
- Spratt, J.E., and Craven, J.A., 2011. Near-surface and crustal-scale images of the Nechako Basin, British Columbia, Canada, from magnetotelluric investigations. *Canadian Journal of Earth Sciences*, 48, 987-999.

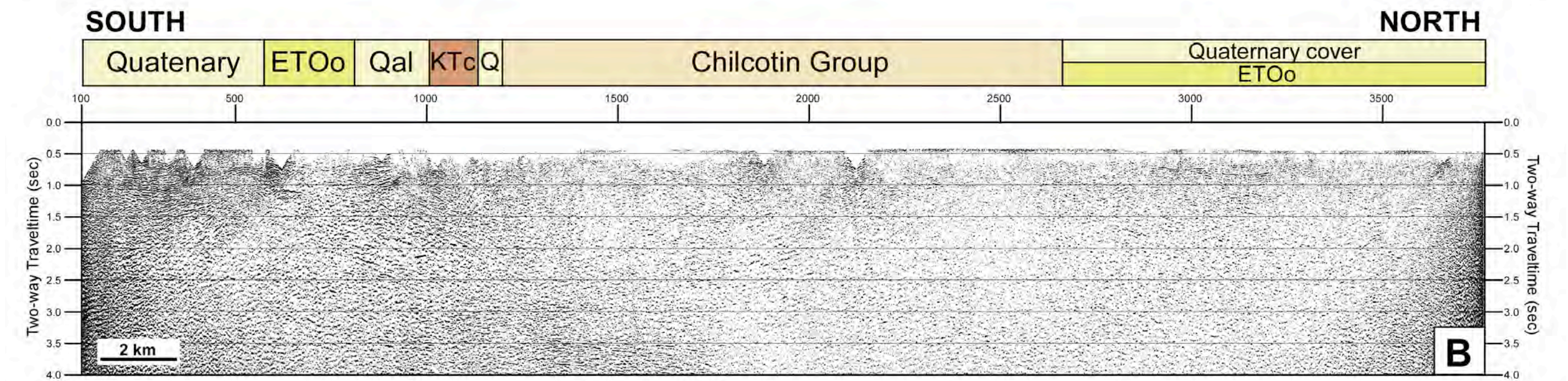
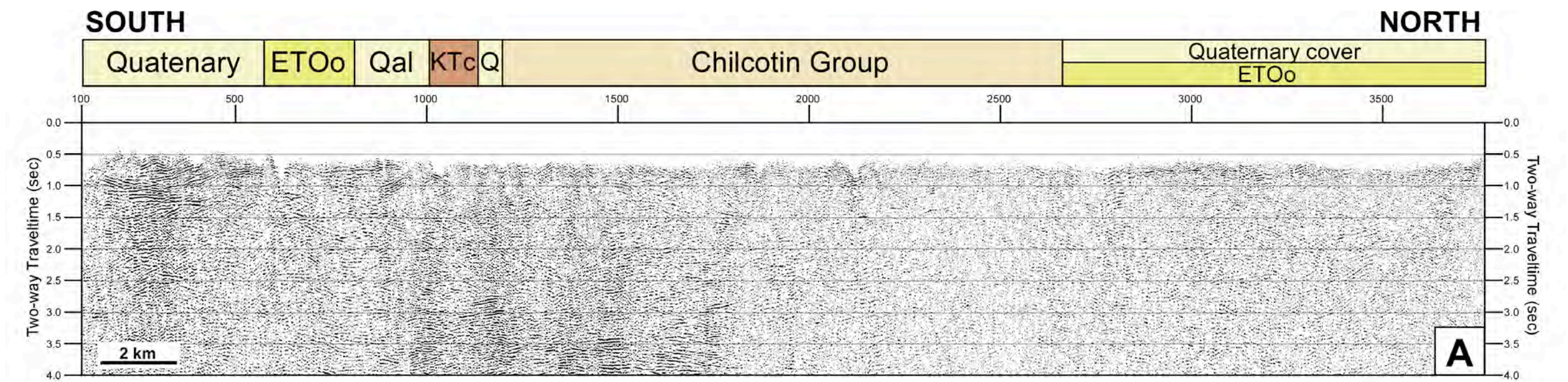
## **Appendix: Fold-out sections**

The seismic sections from this study are reproduced on the following fold-out pages which are three times the normal page width.



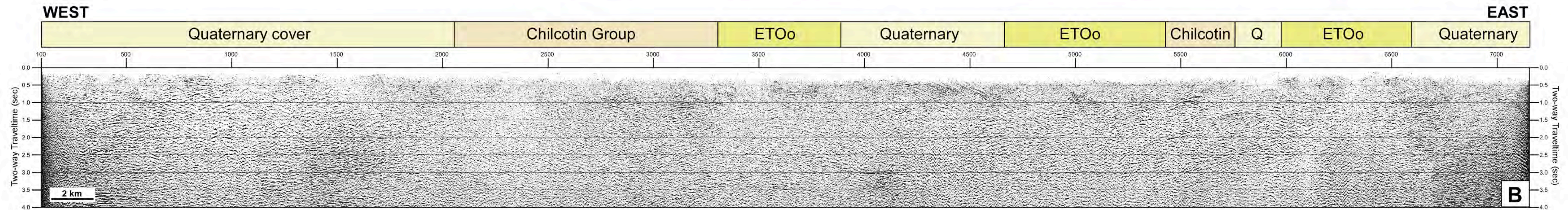
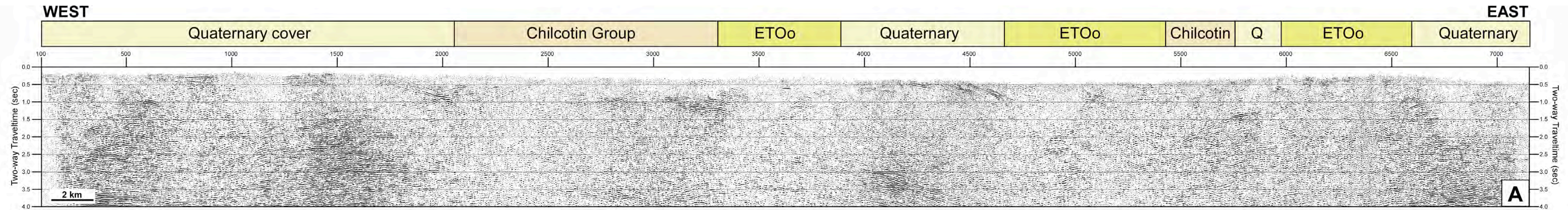
## Line 2008-5

**Figure A-1:** Comparison of final stacks from this study (A) and from the original CGG Veritas processing (B) for Line 2008-5. Surface geology along the line (from Fig. 24) is labelled along the top of each seismic section.



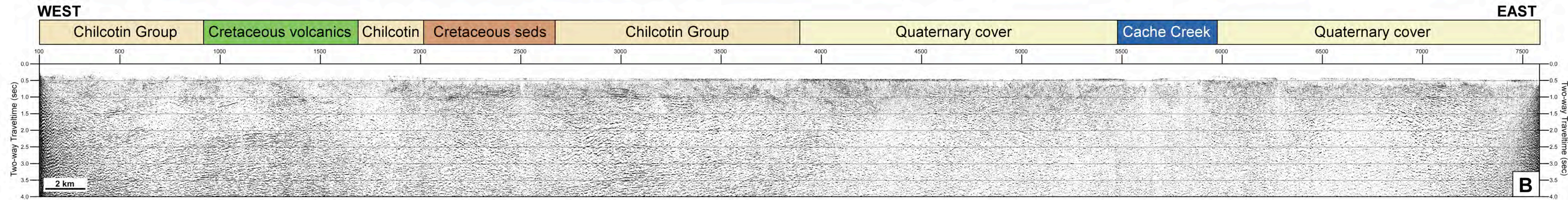
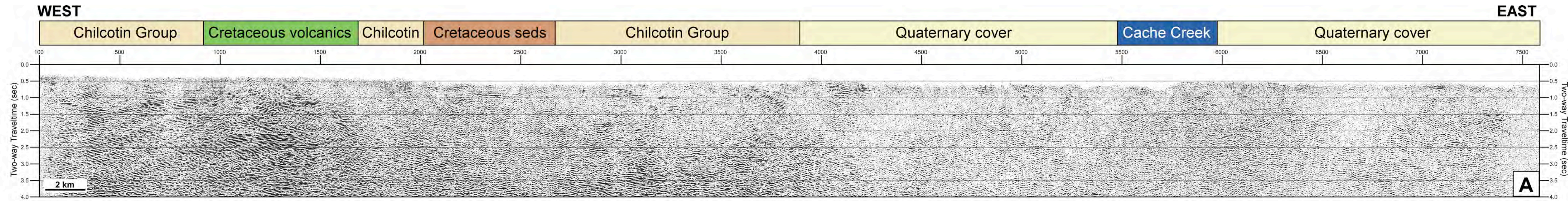
## Line 2008-12

**Figure A-2:** Comparison of final stacks from this study (A) and from the original CGG Veritas processing (B) for Line 2008-12. Surface geology along the line (from Fig. 24) is labelled along the top of each seismic section.



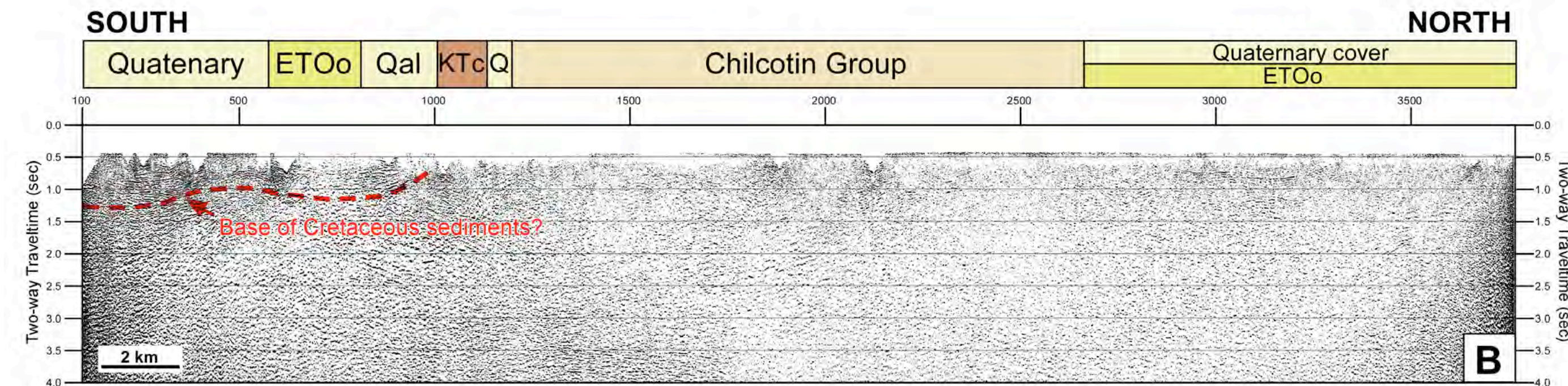
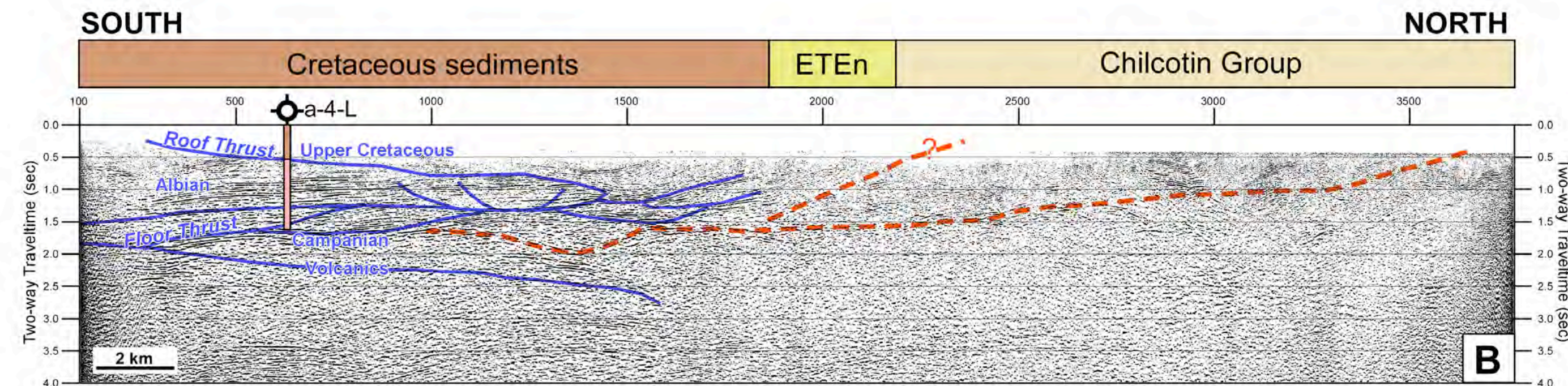
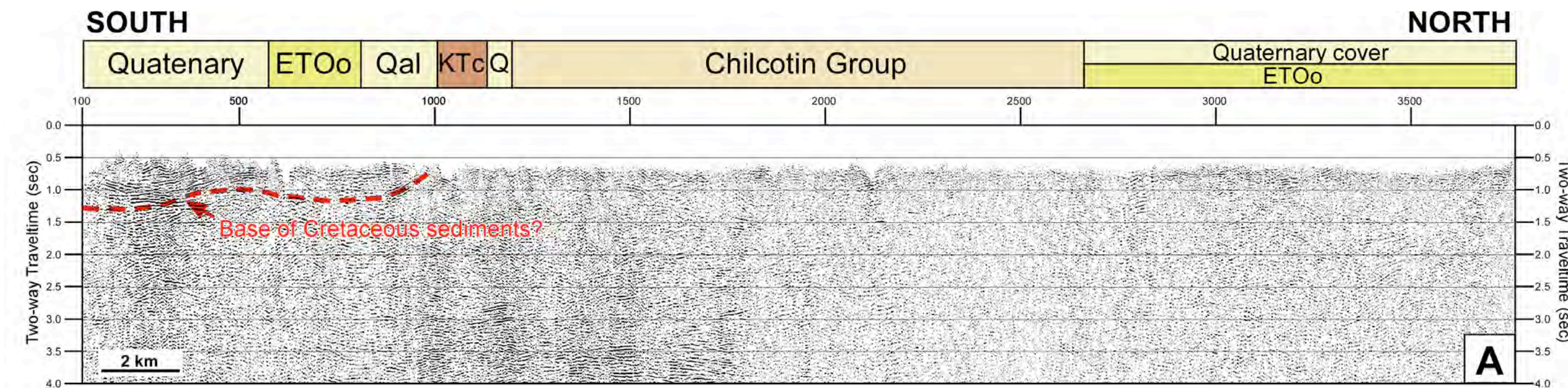
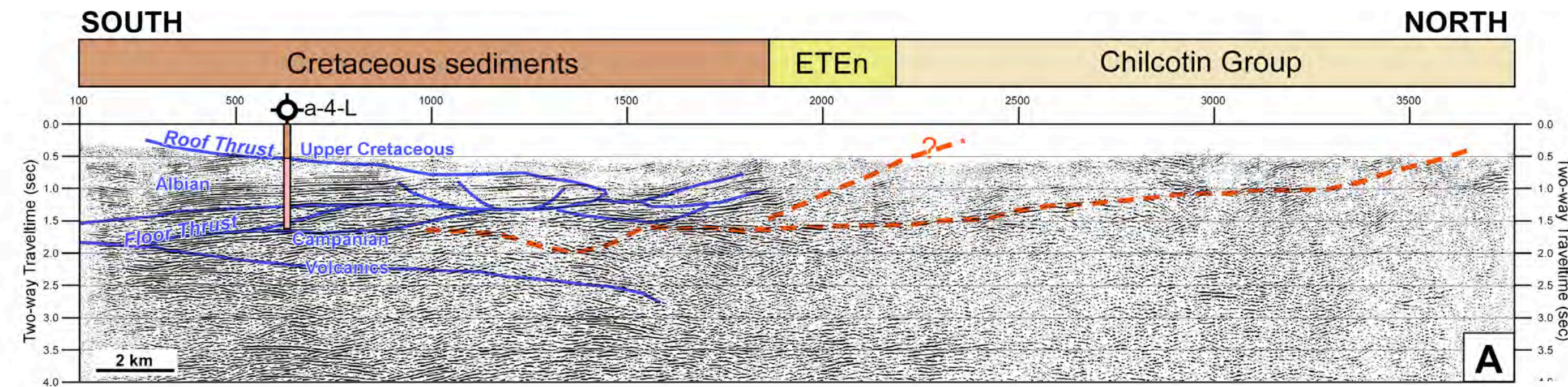
## Line 2008-10

**Figure A-3:** Comparison of final stacks from this study (A) and from the original CGG Veritas processing (B) for Line 2008-10. Surface geology along the line (from Fig. 24) is labelled along the top of each seismic section.



## Line 2008-13

**Figure A-4:** Comparison of final stacks from this study (A) and from the original CGG Veritas processing (B) for Line 2008-13. Surface geology along the line (from Fig. 24) is labelled along the top of each seismic section.

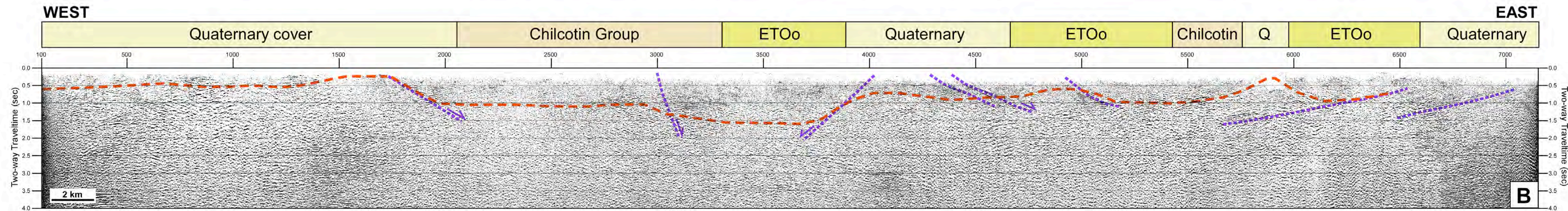
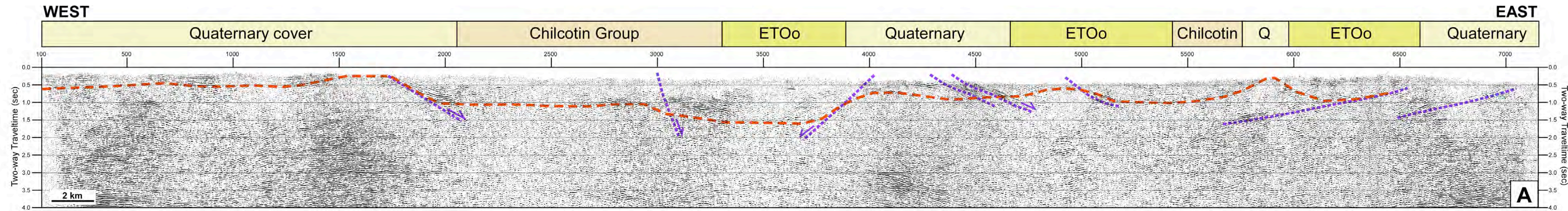


## Line 2008-5

**Figure A-5:** Comparison of interpreted final stacks from this study (A) and from the original CGG Veritas processing (B) for Line 2008-5. The location and lithologies from well a-4-L are shown. The blue lines show the seismic interpretation from Calvert et al. (2011). Dashed orange lines show the MT interpretation from Spratt and Craven (2011). Surface geology along the line (from Fig. 24) is labelled along the top of each seismic section.

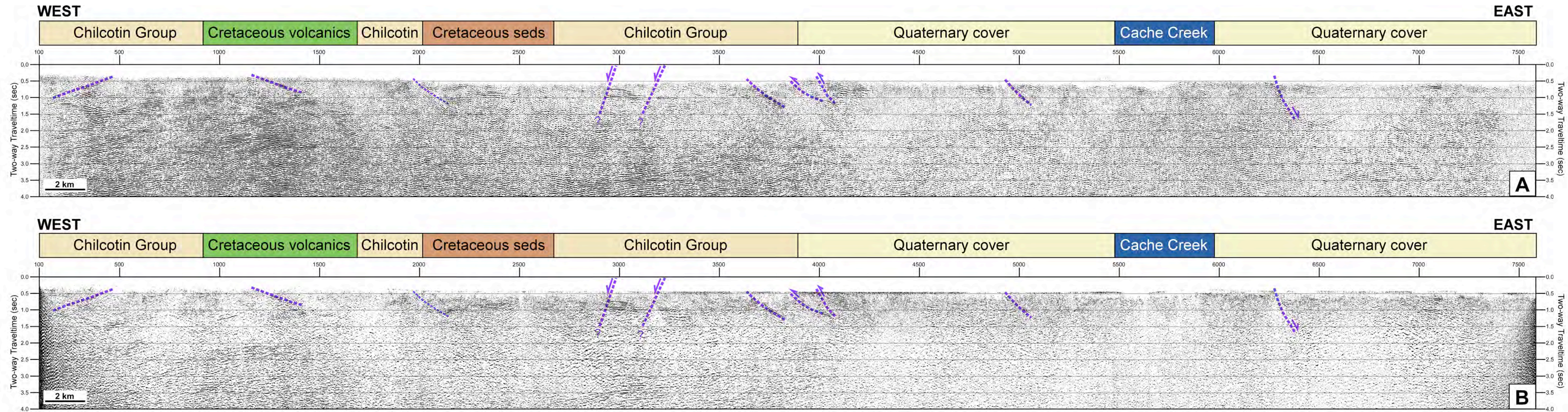
## Line 2008-12

**Figure A-6:** Comparison of interpreted final stacks from this study (A) and from the original CGG Veritas processing (B) for Line 2008-12. The red dashed line shows the seismic interpretation from Calvert et al. (2011). Surface geology along the line (from Fig. 24) is labelled along the top of each seismic section.



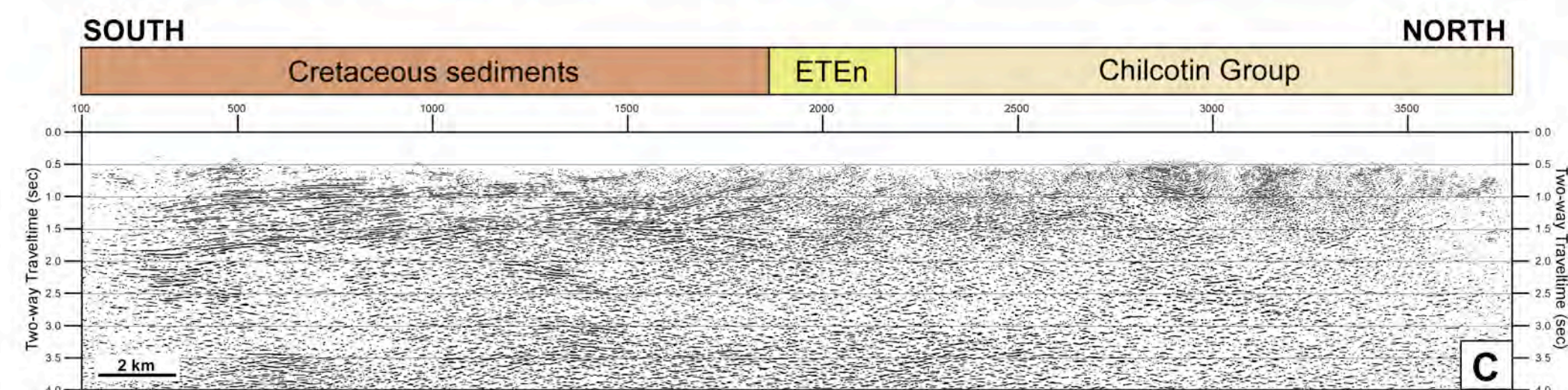
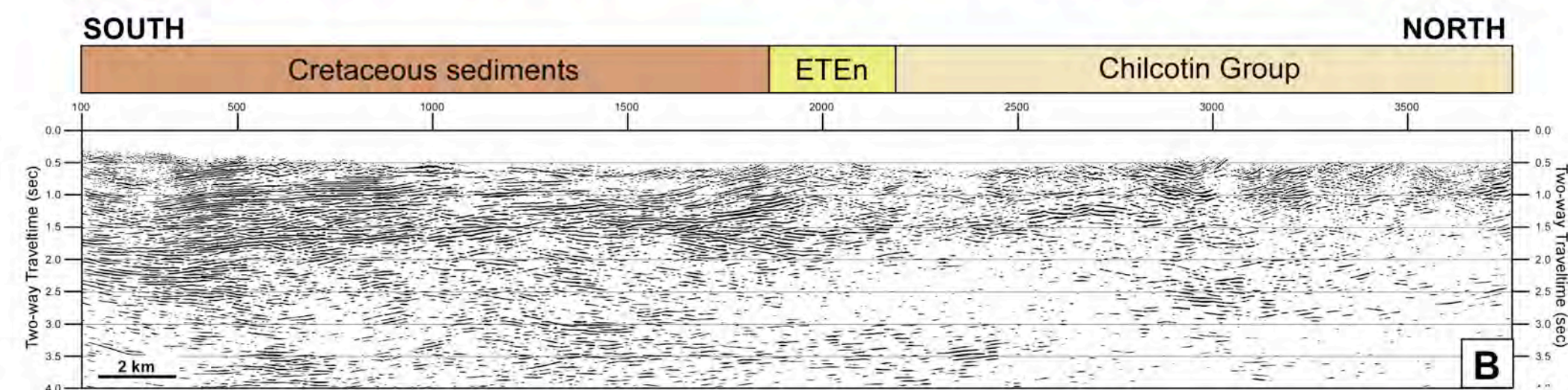
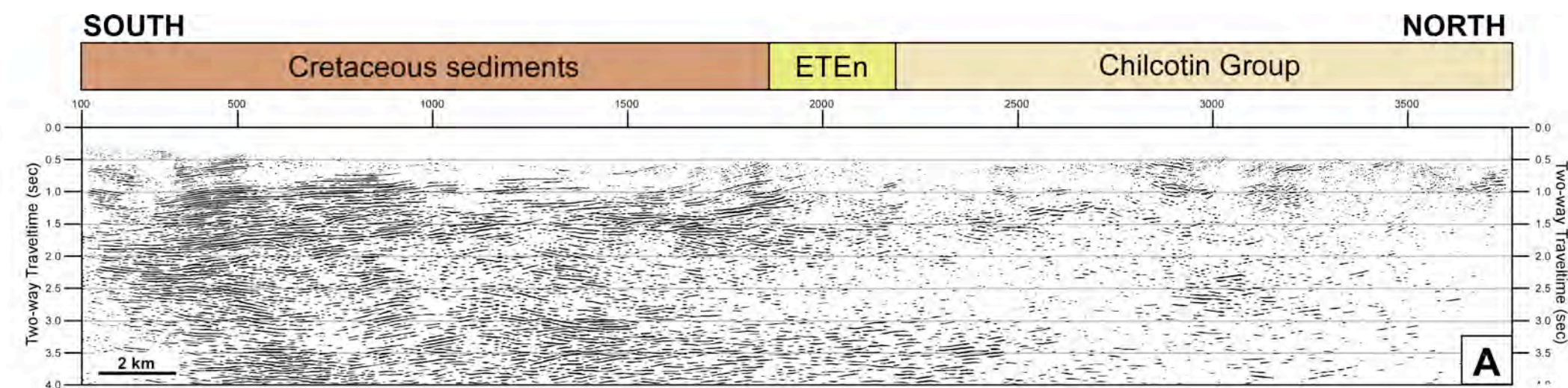
## Line 2008-10

**Figure A-7:** Comparison of interpreted final stacks from this study (A) and from the original CGG Veritas processing (B) for Line 2008-10. The dashed purple lines are faults interpreted by Calvert et al. (2011), Spratt and Craven (2011) and from this study. Dashed orange lines show the MT interpretation from Spratt and Craven (2011). Surface geology along the line (from Fig. 24) is labelled along the top of each seismic section.



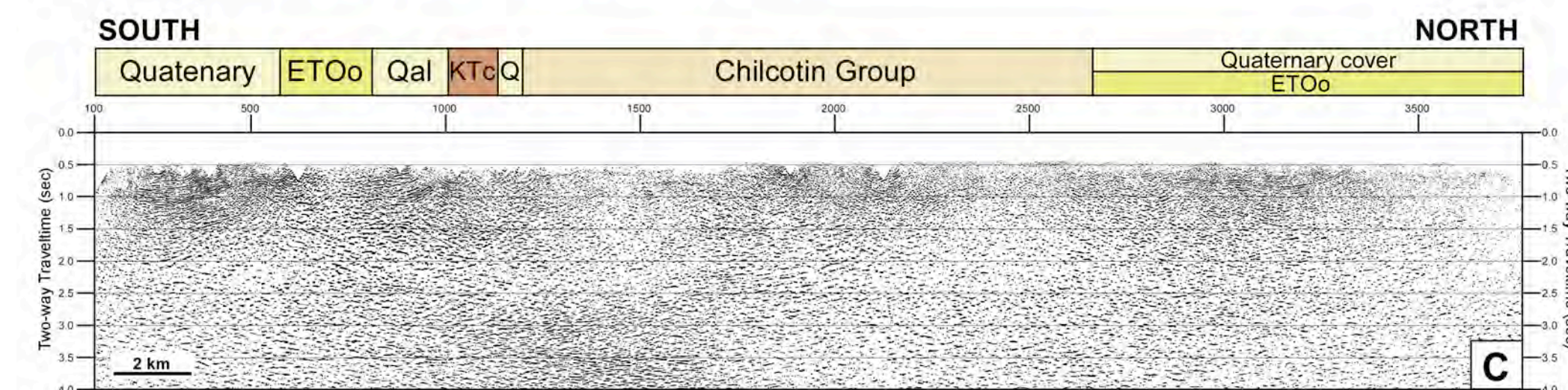
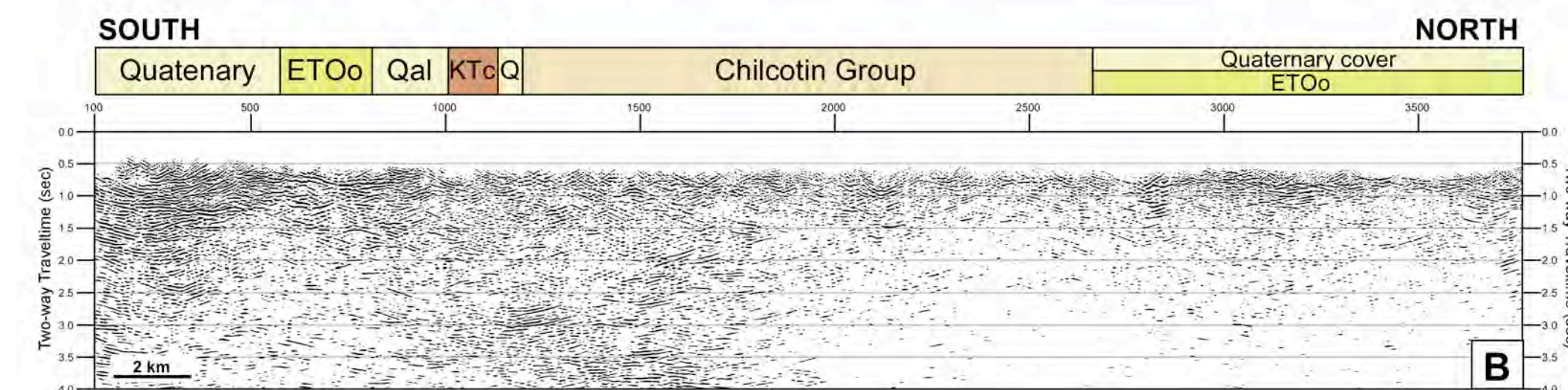
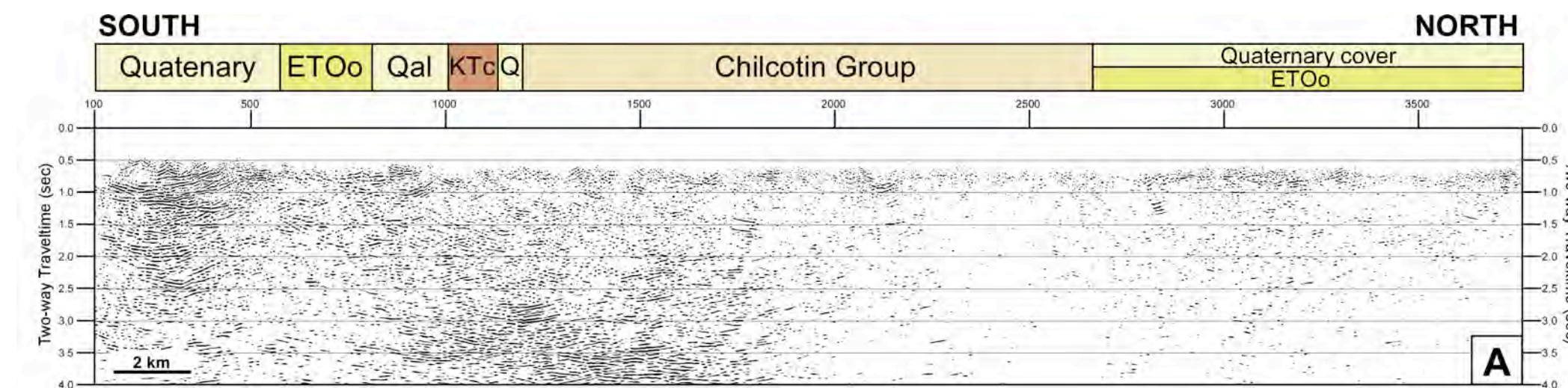
## Line 2008-13

**Figure A-8:** Comparison of interpreted final stacks from this study (A) and from the original CGG Veritas processing (B) for Line 2008-13. The dashed purple lines are faults interpreted from this study and by Calvert et al. (2011). Surface geology along the line (from Fig. 24) is labelled along the top of each seismic section.



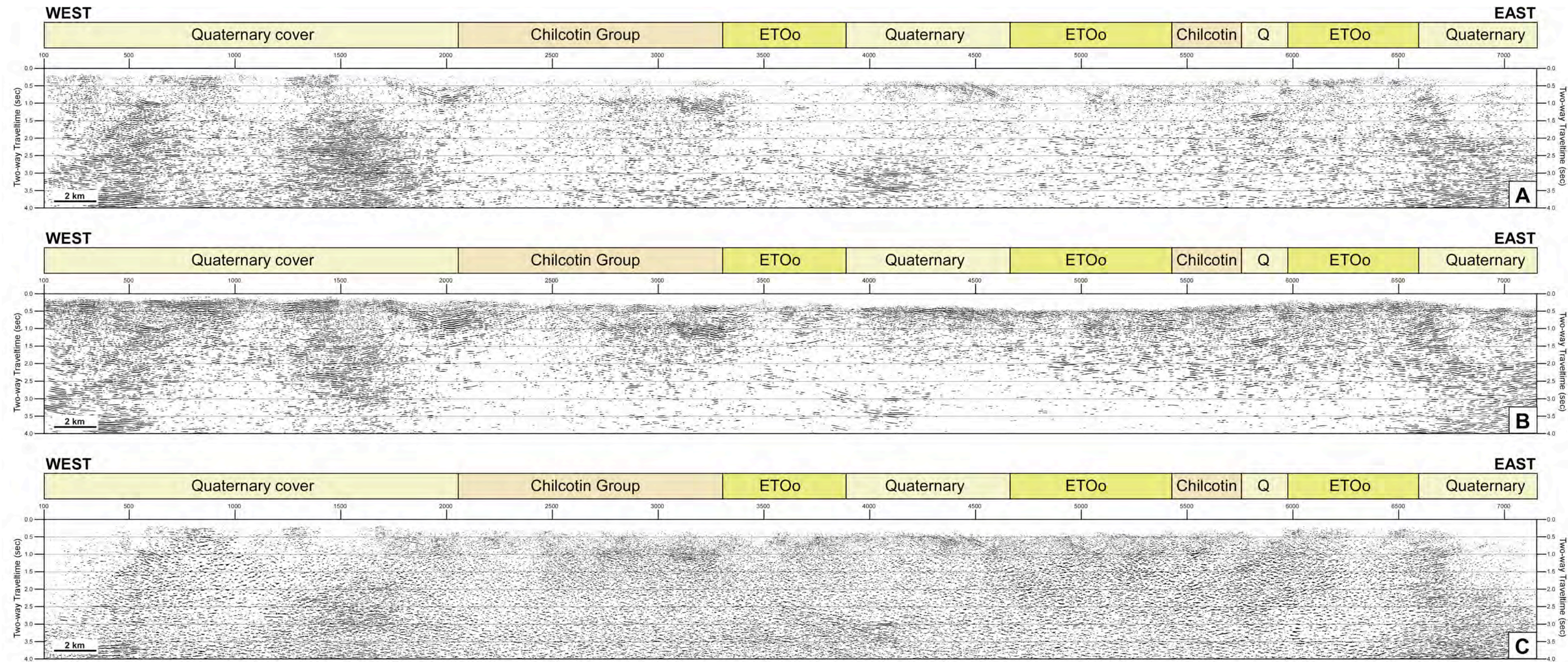
Line 2008-5

**Figure A-9:** Post-stack migrated sections for Line 2008-5; (A) finite-difference with laterally variable velocities (85% smoothed interval velocities), this study; (B) Kirchhoff with laterally variable velocities (85% smoothed stacking velocities), this study; (C) F-K phase-shift with laterally variable velocities (85% smoothed stacking velocities), CGG Veritas processing. Surface geology along the line (from Fig. 24) is labelled along the top of each seismic section.



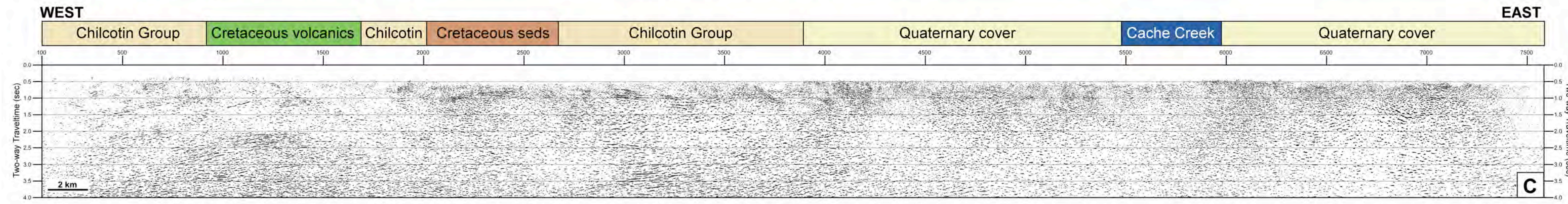
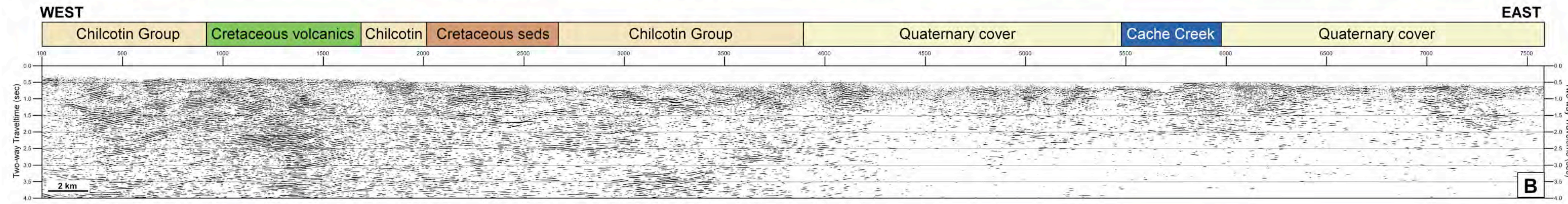
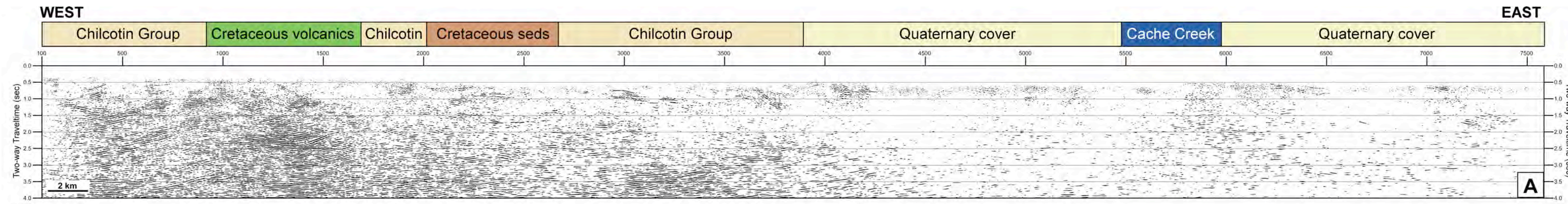
Line 2008-12

**Figure A-10:** Post-stack migrated sections for Line 2008-12; (A) finite-difference with laterally variable velocities (85% smoothed interval velocities), this study; (B) Kirchhoff with laterally variable velocities (85% smoothed stacking velocities), this study; (C) F-K phase-shift with laterally variable velocities (85% smoothed stacking velocities), CGG Veritas processing. Surface geology along the line (from Fig. 24) is labelled along the top of each seismic section.



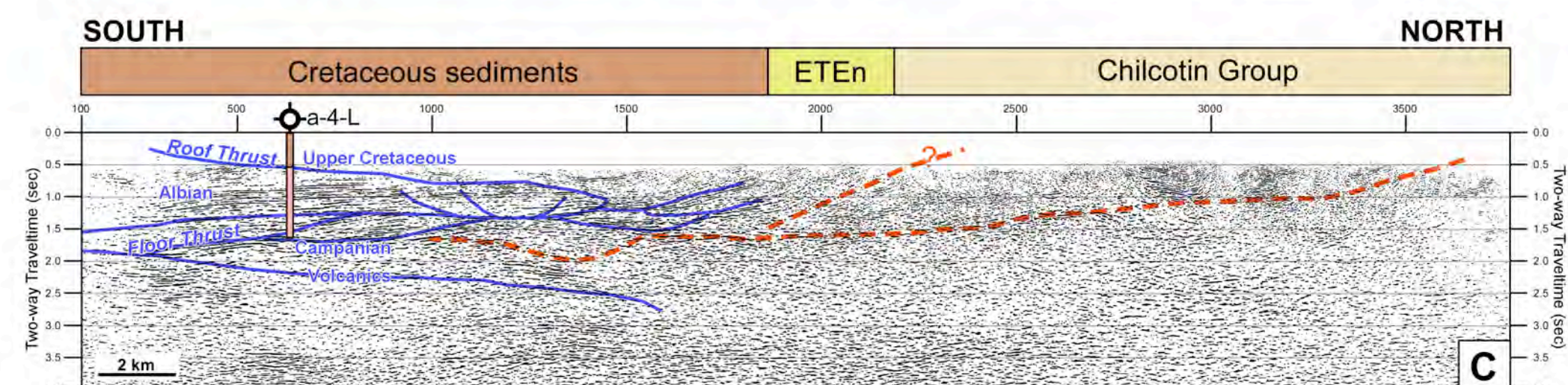
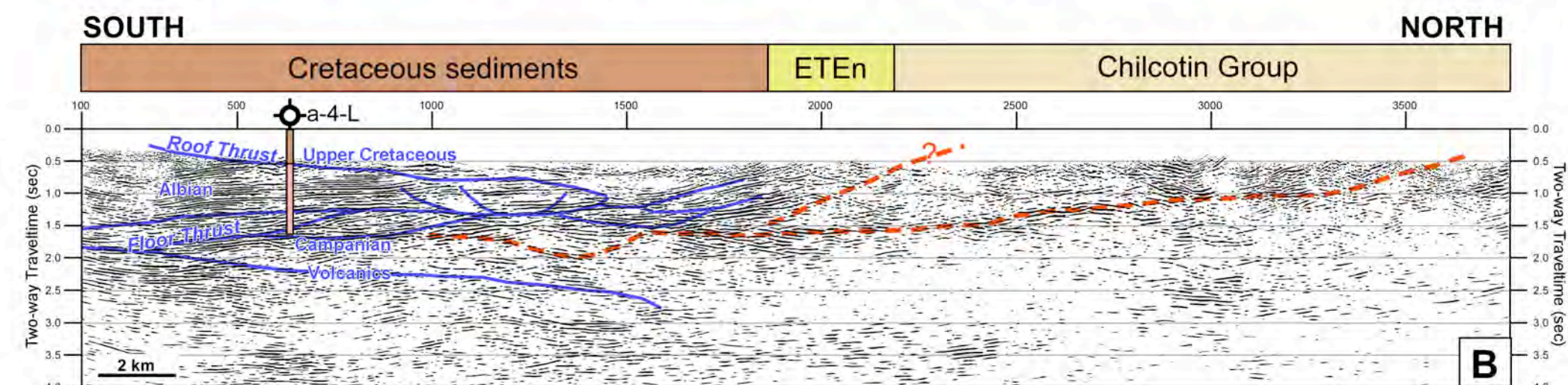
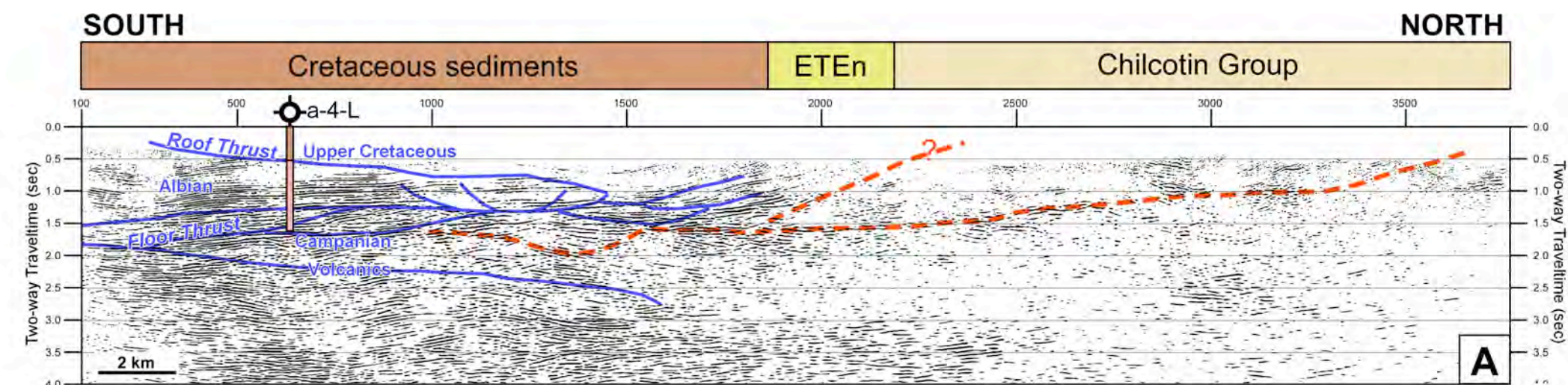
Line 2008-10

**Figure A-11:** Post-stack migrated sections for Line 2008-10; (A) finite-difference with laterally variable velocities (85% smoothed interval velocities), this study; (B) Kirchhoff with laterally variable velocities (85% smoothed stacking velocities), this study; (C) F-K phase-shift with laterally variable velocities (85% smoothed stacking velocities), CGG Veritas processing. Surface geology along the line (from Fig. 24) is labelled along the top of each seismic section.



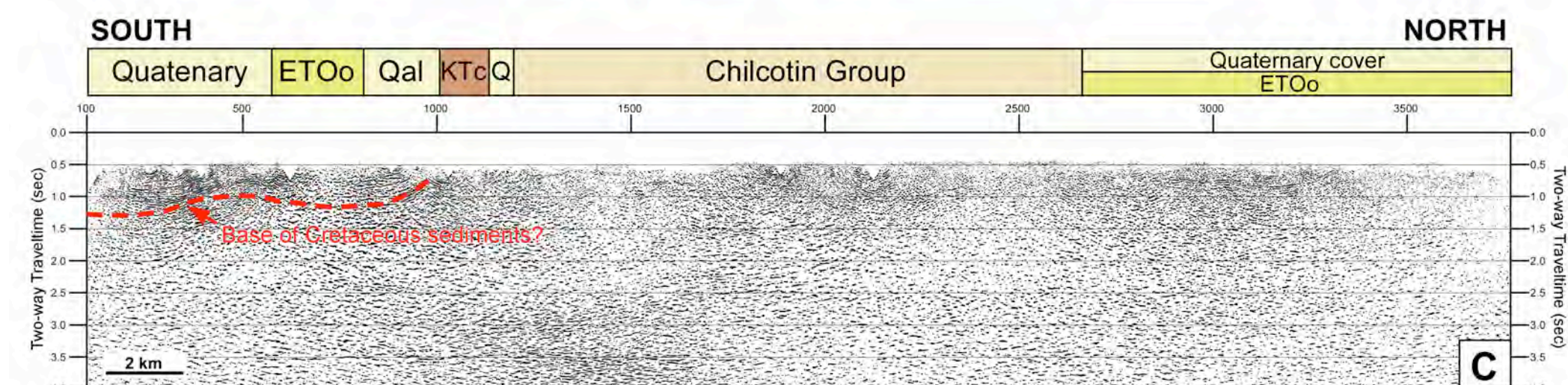
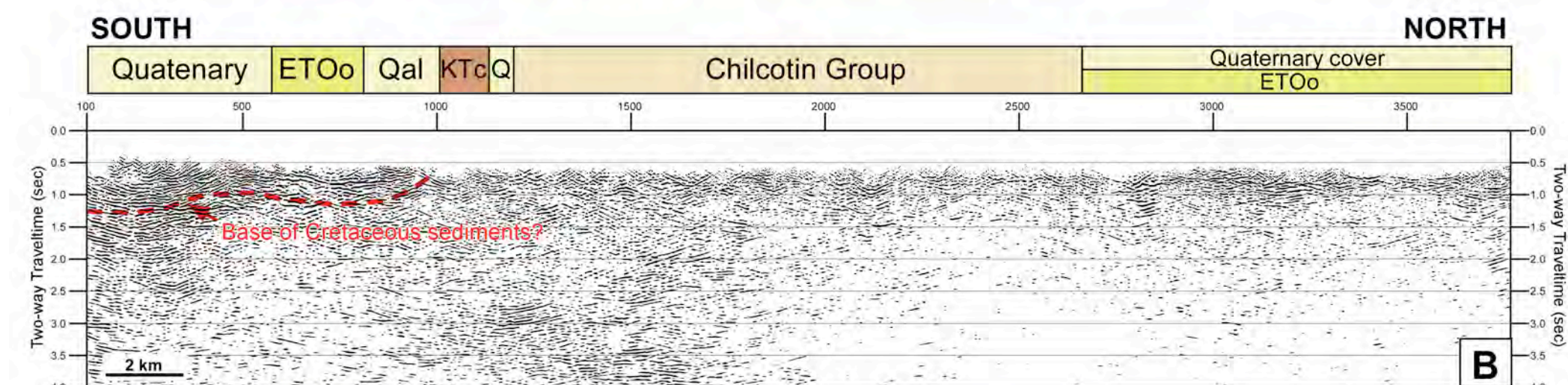
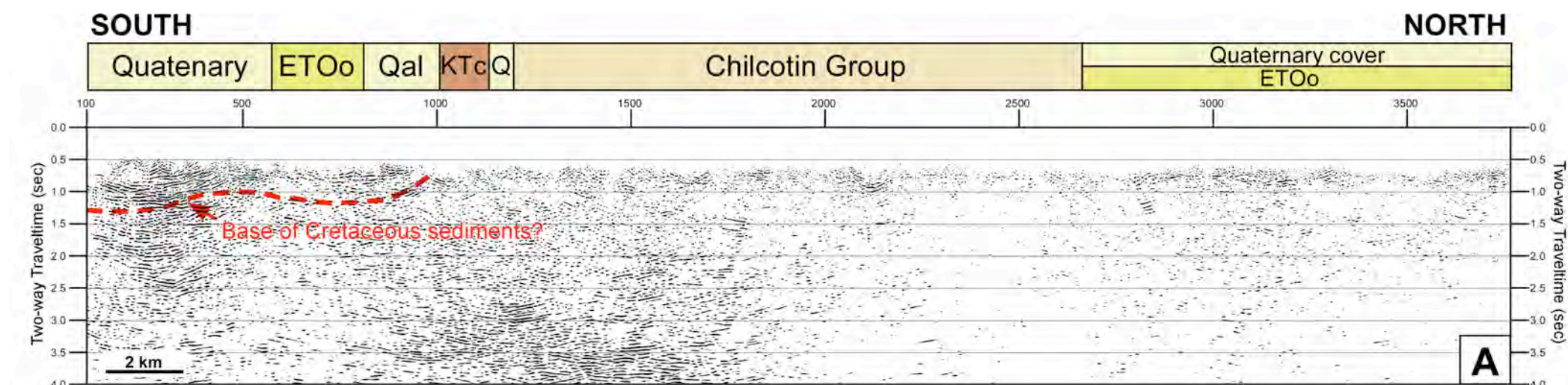
Line 2008-13

**Figure A-12:** Post-stack migrated sections for Line 2008-13; (A) finite-difference with laterally variable velocities (85% smoothed interval velocities), this study; (B) Kirchhoff with laterally variable velocities (85% smoothed stacking velocities), this study; (C) F-K phase-shift with laterally variable velocities (85% smoothed stacking velocities), CGG Veritas processing. Surface geology along the line (from Fig. 24) is labelled along the top of each seismic section.



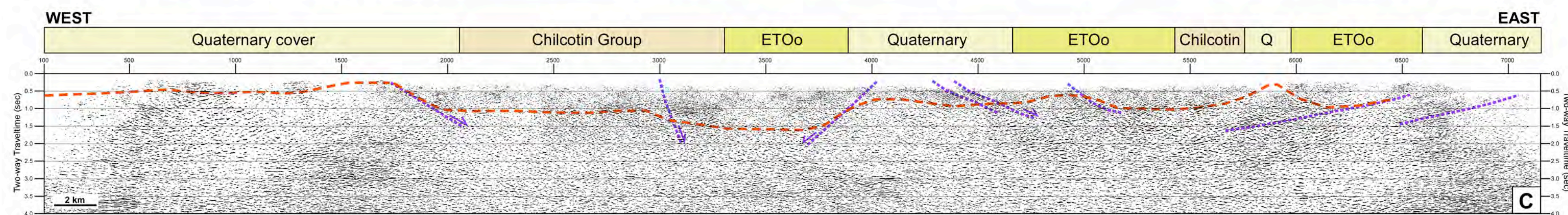
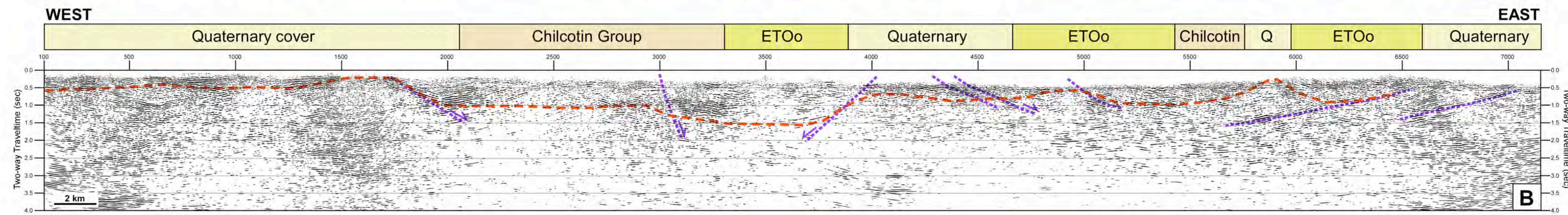
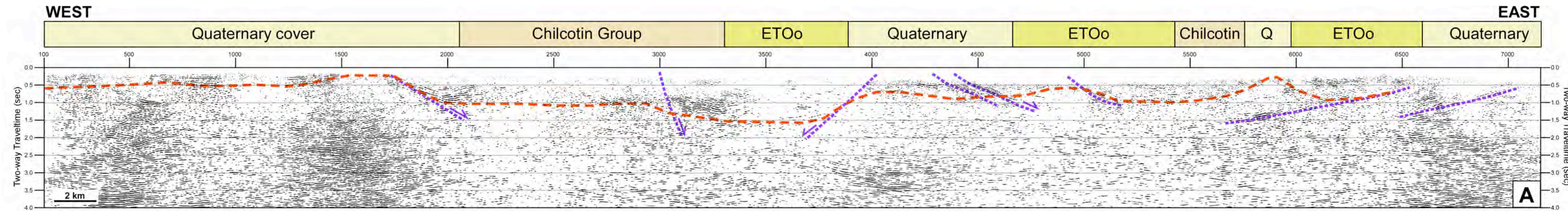
Line 2008-5

**Figure A-13:** Interpreted migrated sections for Line 2008-5; (A) finite-difference with laterally variable velocities (85% smoothed interval velocities), this study; (B) Kirchhoff with laterally variable velocities (85% smoothed stacking velocities), this study; (C) F-K phase-shift with laterally variable velocities (85% smoothed stacking velocities), CGG Veritas processing. The location and lithologies from well a-4-L are shown. The blue lines show the seismic interpretation from Calvert et al. (2011). Dashed orange lines show the MT interpretation from Spratt and Craven (2011). Surface geology along the line (from Fig. 24) is labelled along the top of each seismic section.



Line 2008-12

**Figure A-14:** Interpreted migrated sections for Line 2008-12; (A) finite-difference with laterally variable velocities (85% smoothed interval velocities), this study; (B) Kirchhoff with laterally variable velocities (85% smoothed stacking velocities), this study; (C) F-K phase-shift with laterally variable velocities (85% smoothed stacking velocities), CGG Veritas processing. The red dashed line shows the seismic interpretation from Calvert et al. (2011). Surface geology along the line (from Fig. 24) is labelled along the top of each seismic section.



Line 2008-10

**Figure A-15:** Interpreted migrated sections for Line 2008-10; (A) finite-difference with laterally variable velocities (85% smoothed interval velocities), this study; (B) Kirchhoff with laterally variable velocities (85% smoothed stacking velocities), this study; (C) F-K phase-shift with laterally variable velocities (85% smoothed stacking velocities), CGG Veritas processing. The dashed purple lines are faults interpreted by Calvert et al. (2011), Spratt and Craven (2011) and from this study. Dashed orange lines show the MT interpretation from Spratt and Craven (2011). Surface geology along the line (from Fig. 24) is labelled along the top of each seismic section.

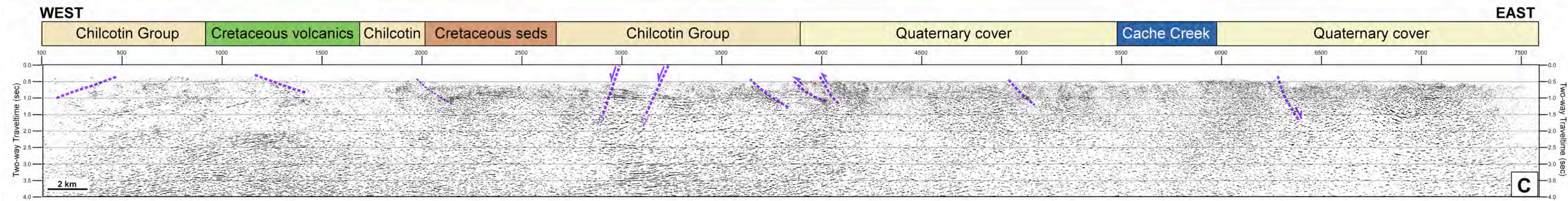
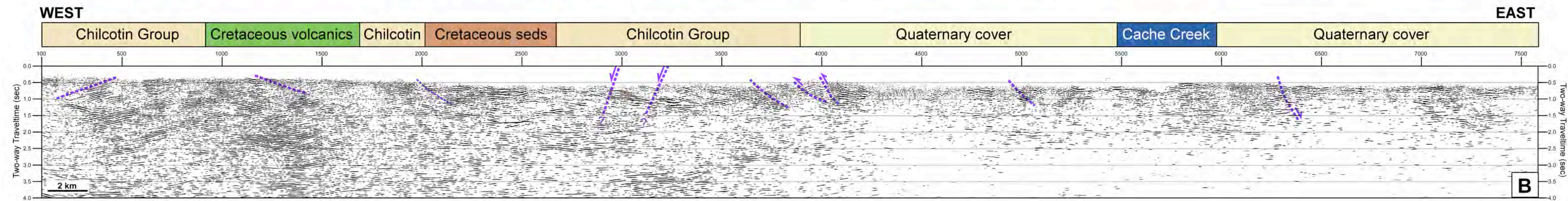
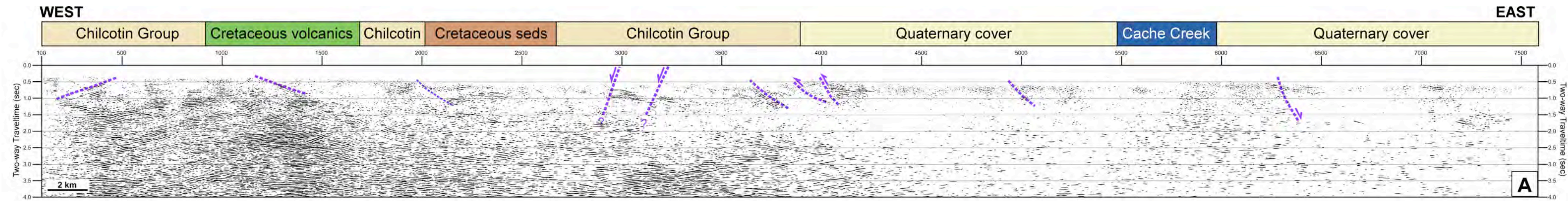
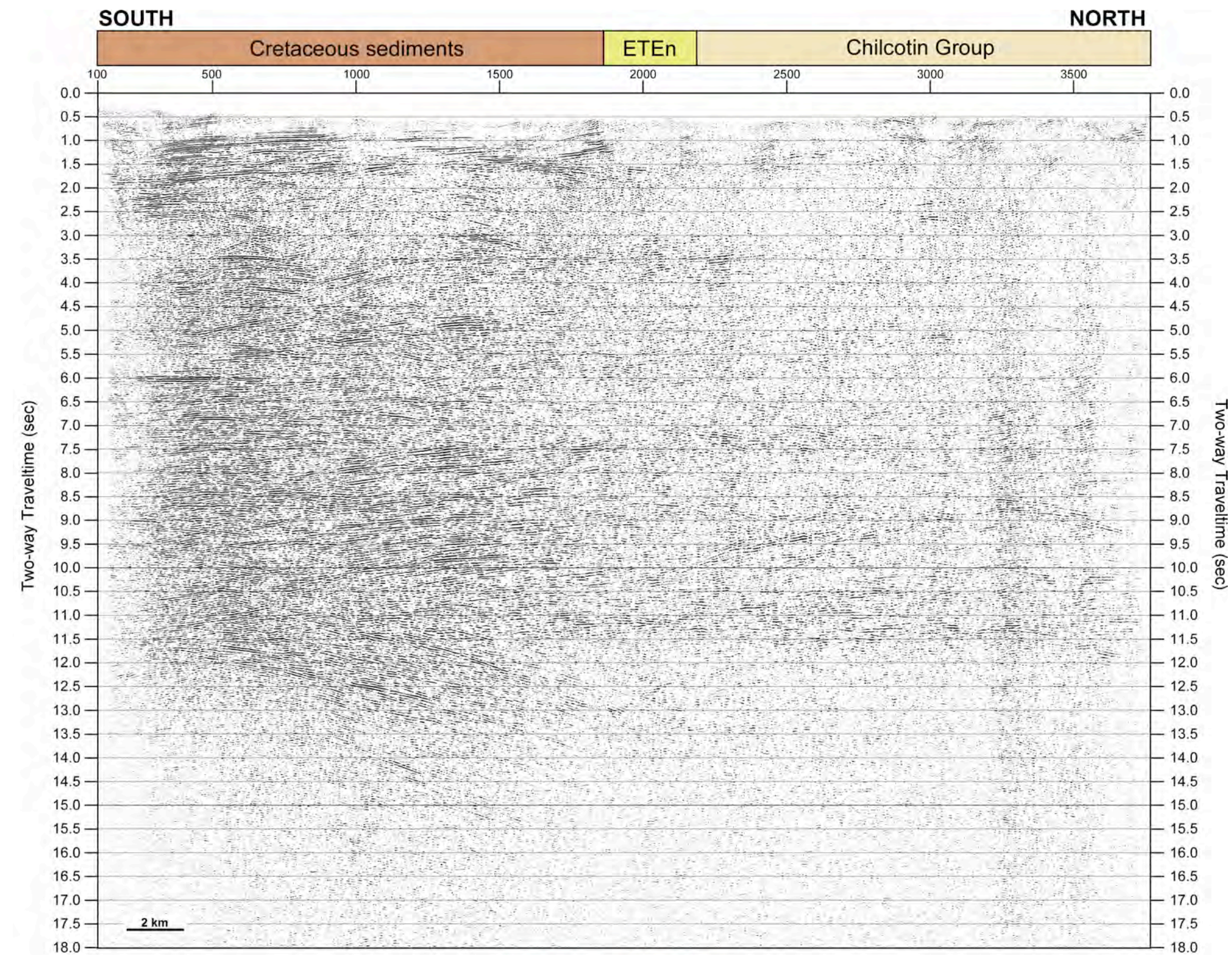


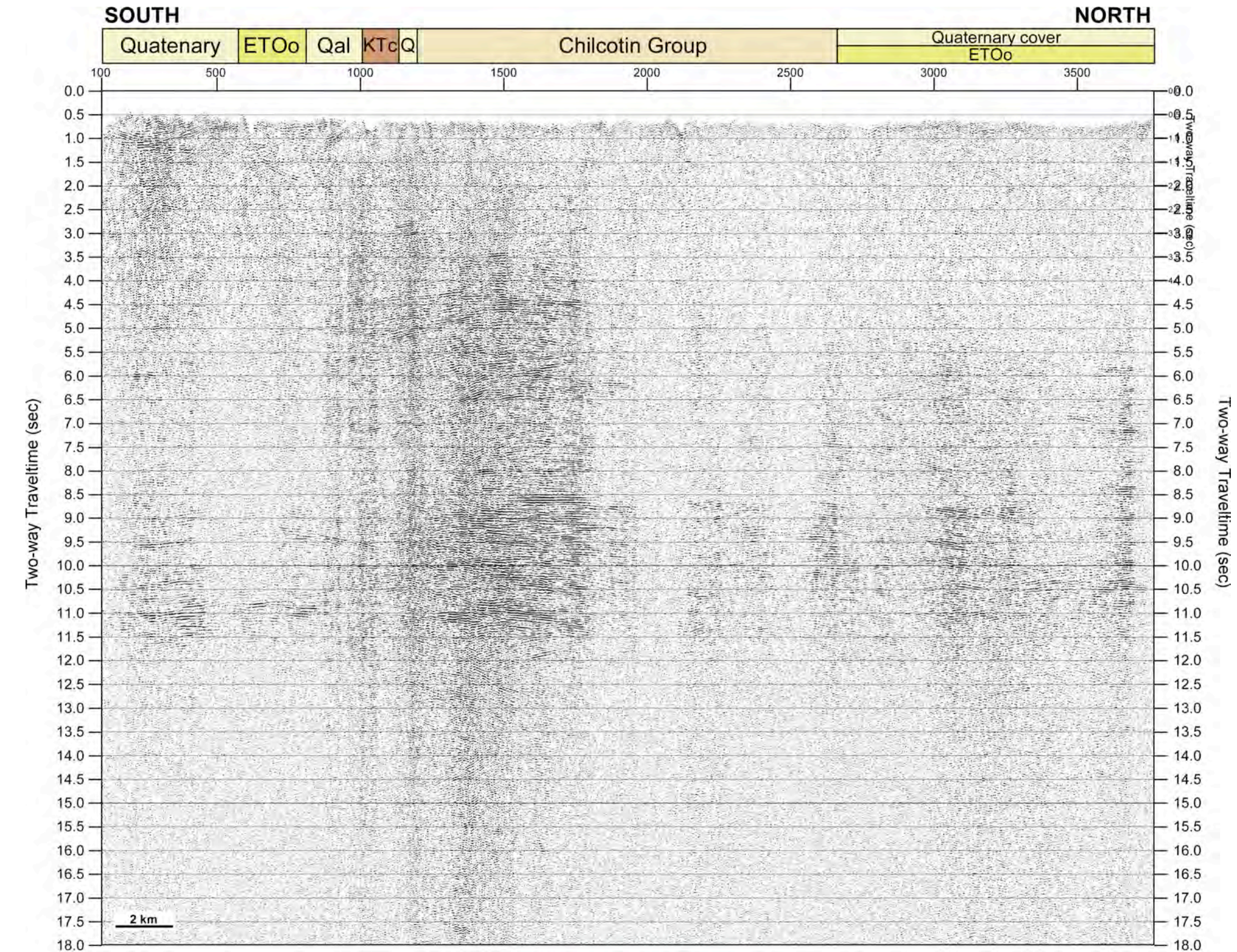
**Figure A-16:** Interpreted migrated sections for Line 2008-13; (A) finite-difference with laterally variable velocities (85% smoothed interval velocities), this study; (B) Kirchhoff with laterally variable velocities (85% smoothed stacking velocities), this study; (C) F-K phase-shift with laterally variable velocities (85% smoothed stacking velocities), CGG Veritas processing. The dashed purple lines are faults interpreted from this study and by Calvert et al. (2011). Surface geology along the line (from Fig. 24) is labelled along the top of each seismic section.

Line 2008-13



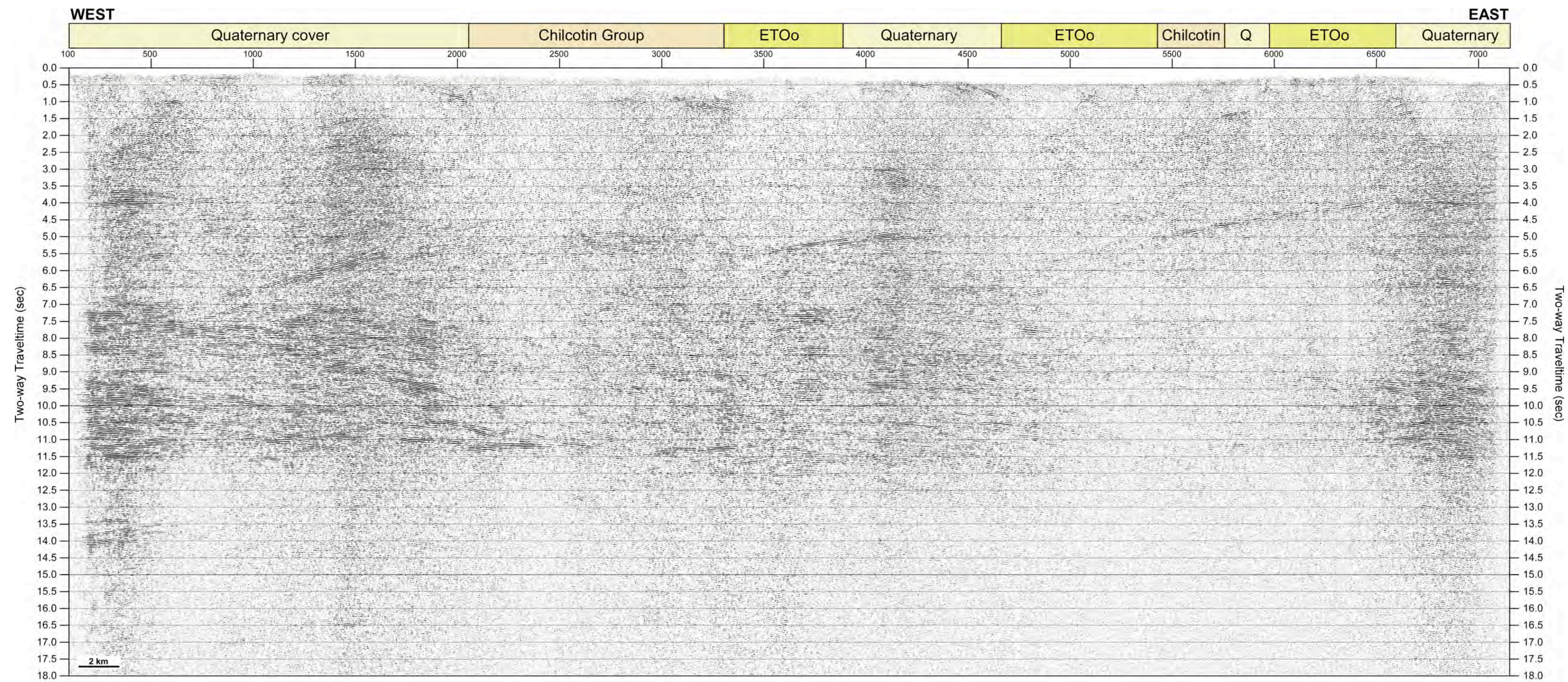
**Line 2008-5**

*Figure A-17: Coherency filtered complete stack (to 18 s TWT) for Line 2008-5. Surface geology along the line (from Fig. 24) is labelled along the top of the seismic section.*



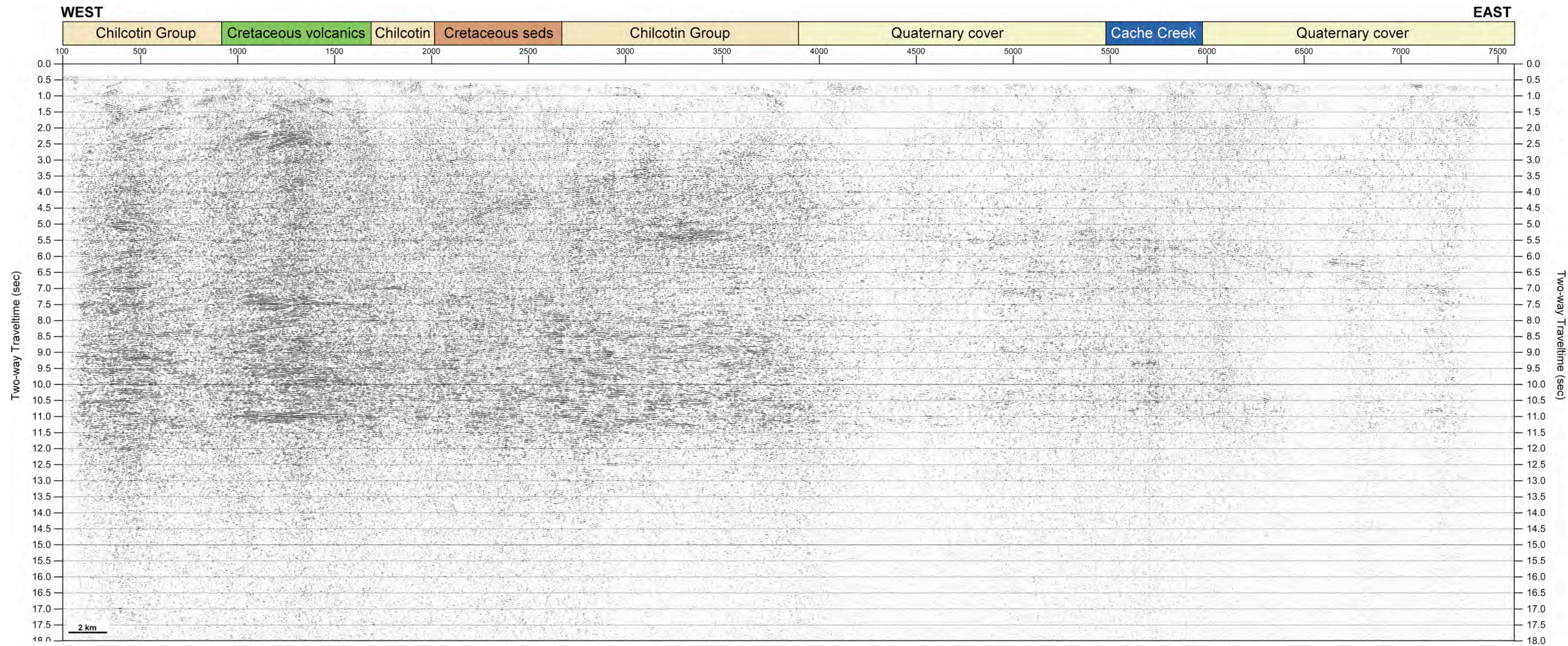
**Line 2008-12**

*Figure A-18: Coherency filtered complete stack (to 18 s TWT) for Line 2008-12. Surface geology along the line (from Fig. 24) is labelled along the top of the seismic section.*



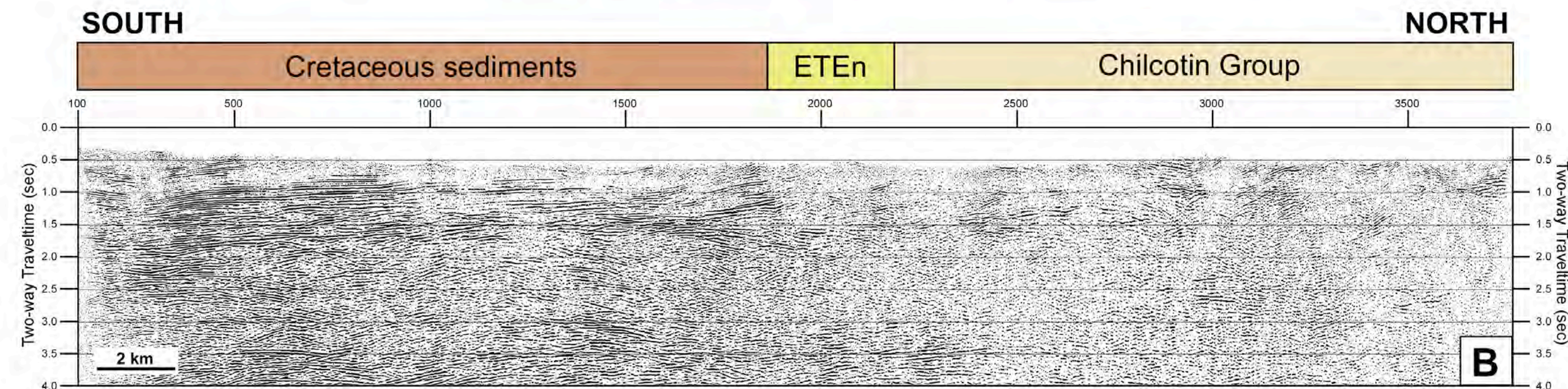
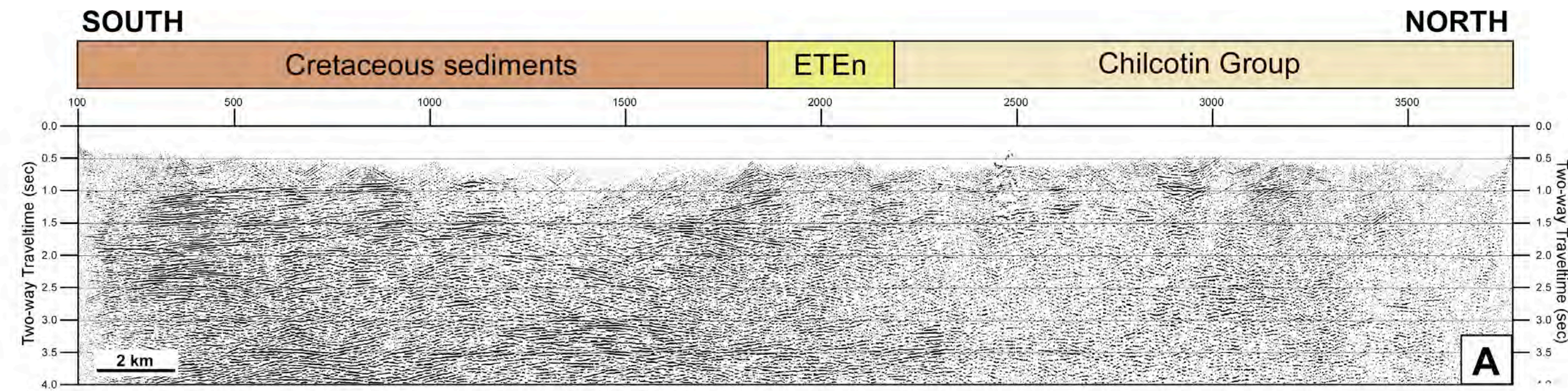
## Line 2008-10

**Figure A-19:** Coherency filtered complete stack (to 18 s TWT) for Line 2008-10. Surface geology along the line (from Fig. 24) is labelled along the top of the seismic section.



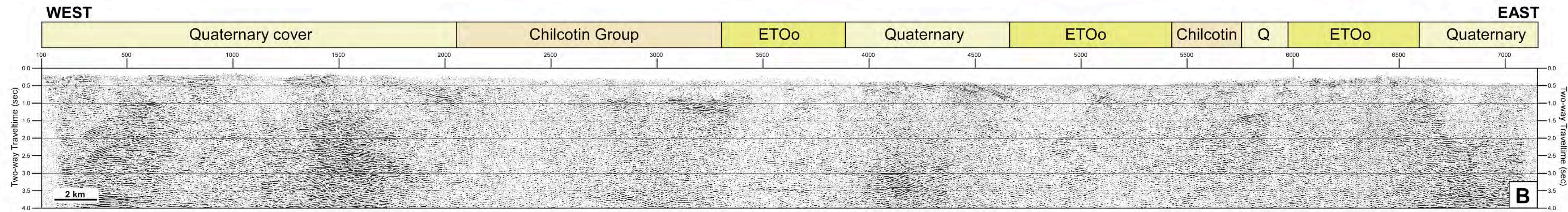
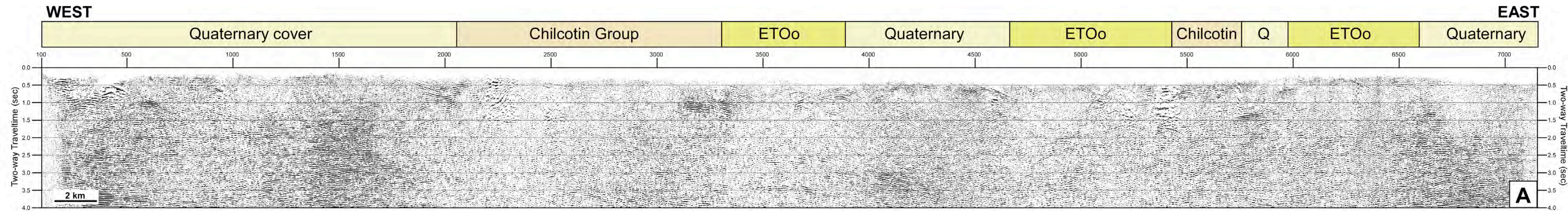
**Line 2008-13**

*Figure A-20: Coherency filtered complete stack (to 18 s TWT) for Line 2008-13. Surface geology along the line (from Fig. 24) is labelled along the top of the seismic section.*



## Line 2008-5

**Figure A-21:** Comparison between brute stack obtained using MT-derived velocities (A) and final stack (B) for Line 2008-5. Surface geology along the line (from Fig. 24) is labelled along the top of the seismic section.



# Line 2008-10

**Figure A-22:** Comparison between brute stack obtained using MT-derived velocities (A) and final stack (B) for Line 2008-10. Surface geology along the line (from Fig. 24) is labelled along the top of the seismic section.